



NAVAL  
POSTGRADUATE  
SCHOOL

MONTEREY, CALIFORNIA

**DISSERTATION**

**TURBULENCE PARAMETERIZATIONS FOR  
CONVECTIVE BOUNDARY LAYERS IN HIGH-  
RESOLUTION MESOSCALE MODELS**

by

Michelle K. Whisenant

December 2003

Dissertation Supervisor:

Qing Wang

**Approved for public release; distribution is unlimited**

THIS PAGE INTENTIONALLY LEFT BLANK

|  |   |   |   |
|--|---|---|---|
| <b>REPORT DOCUMENTATION PAGE</b>   |   |   | <i>Form Approved OMB No. 0704-0188</i>  |
| Public reporting burden for this collection of information is estimated to average 1 hour per response, including the time for reviewing instruction, searching existing data sources, gathering and maintaining the data needed, and completing and reviewing the collection of information. Send comments regarding this burden estimate or any other aspect of this collection of information, including suggestions for reducing this burden, to Washington headquarters Services, Directorate for Information Operations and Reports, 1215 Jefferson Davis Highway, Suite 1204, Arlington, VA 22202-4302, and to the Office of Management and Budget, Paperwork Reduction Project (0704-0188) Washington DC 20503.  |   |   |   |
| <b>1. AGENCY USE ONLY (Leave blank)</b>  | <b>2. REPORT DATE</b><br>December 2003                          | <b>3. REPORT TYPE AND DATES COVERED</b><br>PhD Dissertation     |   |
| <b>4. TITLE AND SUBTITLE:</b> Title (Mix case letters)<br>Turbulence Parameterizations for Convective Boundary Layers in High-Resolution Mesoscale Models  |   | <b>5. FUNDING NUMBERS</b><br>N0001403WX20542<br>N0001403WR20193 |   |
| <b>6. AUTHOR(S)</b> Michelle K. Whisenant  |   |   |   |
| <b>7. PERFORMING ORGANIZATION NAME(S) AND ADDRESS(ES)</b><br>Naval Postgraduate School<br>Monterey, CA 93943-5000  |   | <b>8. PERFORMING ORGANIZATION REPORT NUMBER</b>                 |   |
| <b>9. SPONSORING / MONITORING AGENCY NAME(S) AND ADDRESS(ES)</b><br>N/A  |   | <b>10. SPONSORING / MONITORING AGENCY REPORT NUMBER</b>         |   |
| <b>11. SUPPLEMENTARY NOTES</b> The views expressed in this thesis are those of the author and do not reflect the official policy or position of the Department of Defense or the U.S. Government.  |   |   |   |
| <b>12a. DISTRIBUTION / AVAILABILITY STATEMENT</b><br>Approved for public release; distribution is unlimited.   |   | <b>12b. DISTRIBUTION CODE</b>                                   |   |
| <b>13. ABSTRACT (maximum 200 words)</b><br>Several issues associated with grid resolution and the sub-grid scale (SGS) parameterizations in a mesoscale model are addressed in this study. Of particular concern is the issue concerning increasingly high-resolution mesoscale atmospheric numerical models in that sub-grid scale parameterization of atmospheric processes becomes unclear when the grid resolution becomes comparable to the length scale of the phenomenon. These issues are studied through the careful analysis of in situ data and mesoscale model testing. In this study, we perform observational analysis to better understand the scales of turbulence in various environmental conditions. We then explore the capability of the U.S. Navy's current Coupled Ocean-atmosphere Mesoscale Prediction System (COAMPS™), using a real case study of a cold air outbreak over the Japan/East Sea. We analyze the model's ability to perform accurately within the resolvable scales and to accurately represent the boundary layer turbulence mixing when the resolution is high. Based on results from the above analysis, we modify the existing parameterizations towards more realistic representations of the turbulent processes over a relatively wide range of grid resolution, and test this modification within COAMPS™. |   |   |   |
| <b>14. SUBJECT TERMS</b><br>Grid Resolution, Parameterizations, Boundary Layer, Mesoscale Modeling, COAMPS.  |   | <b>15. NUMBER OF PAGES</b><br>160                               |   |
|  |   | <b>16. PRICE CODE</b>   |   |
| <b>17. SECURITY CLASSIFICATION OF REPORT</b><br>Unclassified   | <b>18. SECURITY CLASSIFICATION OF THIS PAGE</b><br>Unclassified | <b>19. SECURITY CLASSIFICATION OF ABSTRACT</b><br>Unclassified  | <b>20. LIMITATION OF ABSTRACT</b><br>UL |

THIS PAGE INTENTIONALLY LEFT BLANK

Approved for public release; distribution is unlimited

**TURBULENCE PARAMETERIZATIONS FOR CONVECTIVE BOUNDARY  
LAYERS IN HIGH-RESOLUTION MESOSCALE MODELS**

Michelle K. Whisenant  
Lieutenant Commander, United States Navy  
B.S., Florida Institute of Technology, 1990  
M.S., Naval Postgraduate School, 1999

Submitted in partial fulfillment of the  
requirements for the degree of

**DOCTOR OF PHILOSOPHY IN METEOROLOGY**

from the

**NAVAL POSTGRADUATE SCHOOL  
December 2003**

Author:

\_\_\_\_\_  
Michelle K. Whisenant

Approved by:

\_\_\_\_\_  
Qing Wang  
Associate Professor of Meteorology  
Dissertation Supervisor

\_\_\_\_\_  
Carlyle H. Wash  
Professor of Meteorology

\_\_\_\_\_  
Roger T. Williams  
Professor of Meteorology

\_\_\_\_\_  
Robert L. Haney  
Professor of Meteorology

\_\_\_\_\_  
Peter C. Chu  
Professor of Oceanography

\_\_\_\_\_  
Shouping Wang  
Naval Research Lab, Monterey, CA

Approved by:

\_\_\_\_\_  
Carlyle H. Wash, Chair, Department of Meteorology

Approved by:

\_\_\_\_\_  
Carson K. Eoyang, Associate Provost for Academic Affairs

THIS PAGE INTENTIONALLY LEFT BLANK

## ABSTRACT

Several issues associated with grid resolution and the sub-grid scale (SGS) parameterizations in a mesoscale model are addressed in this study. Of particular concern is related to increasingly high-resolution mesoscale atmospheric numerical models, in that sub-grid scale parameterization of atmospheric processes becomes unclear when the grid resolution becomes comparable to the length scale of the phenomenon. These issues are studied through the careful analysis of in situ observations and mesoscale model testing. In this study, we perform observational analysis to better understand the scales of turbulence in various environmental conditions. We then explore the capability of the U.S. Navy's current Coupled Ocean-atmosphere Mesoscale Prediction System (COAMPS<sup>TM</sup>), using a case study of boundary layer roll vortices in cold air outbreak conditions over the Japan/East Sea. We analyze the model's ability to perform accurately within the resolvable scales and to accurately represent the boundary layer turbulence mixing when the resolution is high. Based on results from the above analysis, we modify the existing parameterizations towards more realistic representations of the turbulent processes over a relatively wide range of grid resolution, and test this modification within COAMPS<sup>TM</sup>.

THIS PAGE INTENTIONALLY LEFT BLANK

# TABLE OF CONTENTS

|             |  |           |
|-------------|--|-----------|
| <b>I.</b>   | <b>INTRODUCTION.....</b>   | <b>1</b>  |
|             | <b>A. MESOSCALE MODELING TODAY .....</b>   | <b>1</b>  |
|             | <b>B. THE IMPORTANCE OF HIGH RESOLUTION MESOSCALE MODELING FOR NAVY OPERATIONS .....</b>                   | <b>7</b>  |
|             | <b>C. PREVIOUS STUDIES IN HIGH RESOLUTION MESOSCALE MODELING.....</b>                                      | <b>8</b>  |
|             | <b>D. HIGH RESOLUTION AND MODEL PARAMETERIZATIONS.....</b>   | <b>10</b> |
|             | <b>E. OBJECTIVES OF RESEARCH .....</b>   | <b>12</b> |
|             | <b>F. SUMMARY OF DISSERTATION .....</b>  | <b>13</b> |
| <b>II.</b>  | <b>BACKGROUND .....</b>  | <b>15</b> |
|             | <b>A. PHYSICAL PROCESSES GENERATING BOUNDARY LAYER TURBULENT KINETIC ENERGY .....</b>                      | <b>15</b> |
|             | <b>B. SCALES OF MOTION IN THE ATMOSPHERE .....</b>   | <b>18</b> |
|             | 1. Atmospheric Energy Spectrum .....   | 18        |
|             | 2. Turbulent Energy Spectrum.....  | 19        |
|             | 3. Scales of Atmospheric Turbulence.....   | 19        |
|             | <b>C. REPRESENTATION OF TURBULENCE IN NUMERICAL MODELS .....</b>   | <b>29</b> |
|             | 1. Direct Numerical Simulations.....   | 29        |
|             | 2. Large Eddy Simulations.....   | 29        |
|             | 3. Ensemble Turbulence Closure.....  | 30        |
|             | <b>D. COAMPS™ ENSEMBLE BL PARAMETERIZATION SCHEME.....</b>   | <b>31</b> |
|             | <b>E. FORMULATIONS OF VERTICAL MIXING LENGTH SCALES WITHIN BL TURBULENCE PARAMETERIZATION SCHEMES.....</b> | <b>33</b> |
| <b>III.</b> | <b>DETERMINING THE SCALE OF TURBULENCE FROM OBSERVATIONS.....</b>  | <b>37</b> |
|             | <b>A. OBJECTIVE .....</b>  | <b>37</b> |
|             | <b>B. ANALYSIS OF TURBULENCE SPECTRA FROM OBSERVATIONS.....</b>  | <b>37</b> |
|             | 1. Aircraft Observations.....  | 37        |
|             | a. <i>Japan/East Sea (JES) Experiment.....</i>   | <i>37</i> |
|             | b. <i>Tropical Ocean Global Atmosphere Coupled Ocean-Atmosphere Response Experiment (TOGA COARE).....</i>  | <i>38</i> |
|             | c. <i>FIRE Experiment.....</i>   | <i>42</i> |
|             | 2. Statistical Calculations for Spectral Estimates .....   | 42        |
|             | 3. Spectral Analysis.....  | 43        |
|             | a. <i>Method and Objectives.....</i>   | <i>43</i> |
|             | b. <i>Surface Layer Spectra.....</i>   | <i>44</i> |
|             | c. <i>Mixed Layer Spectra.....</i>   | <i>49</i> |
|             | d. <i>Conclusions.....</i>   | <i>55</i> |

|     |   |     |
|-----|---|-----|
| C.  | TURBULENCE INTEGRAL LENGTH SCALES FROM OBSERVATIONS.....                                    | 56  |
| 1.  | Importance of Integral Length Scale Analysis.....   | 56  |
| 2.  | Integral Length Scale Calculation.....  | 56  |
| a.  | <i>Formulation</i> .....  | 56  |
| b.  | <i>Calculation of Partial Integral Length Scales</i> .....                                  | 56  |
| 3.  | Results .....   | 58  |
| 4.  | Conclusions.....  | 62  |
| IV. | CASE STUDY USING HIGH-RESOLUTION COAMPS™ .....  | 63  |
| A.  | INTRODUCTION.....   | 63  |
| B.  | COAMPS™ .....   | 63  |
| C.  | JES CASE STUDY - DESCRIPTION .....  | 65  |
| 1.  | Overview .....  | 65  |
| 2.  | Synoptic Conditions for JES0216.....  | 65  |
| 3.  | BL Roll Vortices.....   | 71  |
| a.  | <i>Satellite Imagery</i> .....  | 71  |
| b.  | <i>General Structure and Characteristics of Roll Vortices</i> .....                         | 73  |
| c.  | <i>Aircraft Observations</i> .....  | 77  |
| D.  | DESCRIPTION OF COAMPS™ SIMULATIONS OVER THE JES .....                                       | 83  |
| E.  | ANALYSIS OF COAMPS™ SIMULATIONS.....  | 85  |
| 1.  | Effects of Model Numerics .....   | 85  |
| 2.  | Analysis of COAMPS™ Results from the Control Run .....                                      | 90  |
| a.  | <i>BL Development</i> .....   | 90  |
| b.  | <i>Surface Fluxes</i> .....   | 96  |
| F.  | SUMMARY AND CONCLUSIONS .....   | 98  |
| V.  | COAMPS™ CASE STUDY SIMULATION USING A RESOLUTION-DEPENDENT TURBULENCE PARAMETERIZATION..... | 101 |
| A.  | MODIFICATION TO COAMPS™ MIXING LENGTH.....  | 101 |
| 1.  | Rationale and Motivation.....   | 101 |
| 2.  | Modified Mixing Length Formulation for COAMPS™ .....  | 102 |
| B.  | EFFECTS OF MODIFIED MIXING LENGTH ON SIMULATING THE ROLL STRUCTURE .....                    | 106 |
| 1.  | Boundary Layer Mean Structure .....   | 106 |
| 2.  | Spectral Analysis of Resolvable Scale Mean Fields .....                                     | 114 |
| 3.  | SGS TKE and Fluxes .....  | 122 |
| C.  | SUMMARY .....   | 129 |
| VI. | SUMMARY, CONCLUSIONS, AND RECOMMENDATIONS .....   | 131 |
| A.  | SUMMARY AND CONCLUSIONS .....   | 131 |
| B.  | RECOMMENDATIONS FOR FURTHER STUDY .....   | 134 |
|     | LIST OF REFERENCES .....  | 137 |
|     | INITIAL DISTRIBUTION LIST .....   | 147 |

## ACKNOWLEDGMENTS

The author would like to thank Dr. Qing Wang for her invaluable assistance during this research. Her patience, wisdom, and guidance were essential to the completion of this effort. Special thanks go to Dr. Shouping Wang at NRL Monterey for numerous helpful discussions on various related issues and to other committee members, Drs. C. H. Wash, R. T. Williams, R. L. Haney, and P. Chu for their comments and suggestions. I also want to thank Drs. Djamal Khelif and Carl Friehe, both from University of California at Irvine, and Haf Jonsson of NPS CIRPAS who kindly provided the fully calibrated data set from the JES aircraft measurements. In addition, the author thanks Mr. Bill Thompson and Mr. Robert Creasey for their assistance with computing issues, Dr. John Kalogiros for his help in calculating turbulence length scales, Mr. Kurt Nielsen for his assistance in obtaining satellite imagery, Ms. Mary Jordan for her assistance in using MATLAB and computer storage issues, Mr. Hongchao Zuo, Dr. James Doyle, Ms. Sue Chen, Dr. Douglas Miller and Dr. Kostantinos Rados for their assistance in using the COAMPS<sup>TM</sup> mesoscale model as a research tool, Ron Ruth and David Carlson of UCAR for their assistance in obtaining TOGA COARE Electra flight data and supporting literature for the data, Professor Shuyi Chen at the University of Miami for providing AVHRR SST imagery, and Dr. Zhiqiu Gao and Dr. Kostantinos Rados for their assistance in the visualization of observational data and model output. Lastly, the author would like to thank her husband, Rob, for his sacrifices, patience, and support throughout the last three years, and my family and good friends for their tremendous encouragement.

This research was supported by the Office of Naval Research under two grants: Award # N0001403WX20542 (including a sub-award to the Naval Postgraduate School) for the Coupled Marine Boundary Layer and Air-Sea Interaction Initiative (CBLAST) and Award # N0001403WR20193 for Evaluation and Improvement of Boundary Layer Parameterizations in COAMPS using aircraft measurements. This work was also supported in part by a grant of computer time from the DOD high Performance Computing Modernization Program at NAVO and ARSC.

THIS PAGE INTENTIONALLY LEFT BLANK

# I. INTRODUCTION

## A. MESOSCALE MODELING TODAY

There are three major requirements for improved numerical weather prediction (NWP): better model physics, better observational data, and better methods for data assimilation. These improvements are very computationally intensive, and thus advances in computer power, coupled with the trend toward local modeling efforts, has allowed for concentrated study of both historical and local real-time mesoscale structures and dynamics, resulting in extensive evaluation, optimization, and improvement in these three key areas of NWP that continues today (Kalnay et al. 1998).

Kalnay et al. (1998) trace the history and improvements of operational NWP at the National Center for Environmental Prediction (NCEP), a review which is representative of improvements at all major NWP operational centers. NWP has evolved from the 381 km resolution of the National Meteorology Center (NMC) 1 level barotropic model of the 1950's, running on a then state-of-the-art IBM 704 supercomputer, to NCEP's operational Eta mesoscale model, with 12 km resolution and 45 vertical levels, running on today's state-of-the-art massively parallel computer system.

While NWP efforts and advancements in mesoscale modeling continue at the national level (with NCEP's Eta mesoscale model and the U.S. Navy's Coupled Ocean-Atmosphere Mesoscale Prediction System (COAMPS<sup>TM</sup>)) a transition is occurring where mesoscale NWP has spread to the regional level (Mass and Kuo 1998). Three major advancements, namely, the advent of modestly priced single and multi-processor workstations, the availability of mesoscale models that run efficiently on workstations, and the accessibility of initial and boundary conditions and forecast fields from operational centers via the internet (Mass and Kuo 1998), have given meteorologists the ability to locally run and utilize the output of non-hydrostatic, three-dimensional atmospheric numerical models over scales of thousands of kilometers for research, teaching, and operational use. As of early 2002, over fifty state-of-the-art mesoscale and regional real-

time NWP efforts exist at universities, government laboratories, and research facilities in the United States.

Computational improvements and the vast application of mesoscale models for various meteorological phenomena have allowed for development of more detailed model physics and parameterization schemes within the research community for use in mesoscale models. One example is in precipitation predictions. Precipitation is one of the most difficult aspects of NWP, since it is often organized at the mesoscales between a few tens to a few hundred kilometers. One example of work to improve precipitation forecasts is the use of complex land-surface schemes, which have seen limited use in mesoscale modeling due to limitations in computing power. While they have been proven important in climate change studies using general circulation models (GCM), Wen et al. (2000) examine the role that land surface schemes play in short-range precipitation forecasts within mesoscale models. Two different land surface schemes are compared, providing lower boundary conditions to the Mesoscale Compressibility Community Model (MC2): the force-restore method, a simple land surface scheme used in many GCM and atmospheric models that contains a two-layer closure condition on the heat and moisture balances at the air-soil interface, and the Canadian Land Surface Scheme (CLASS), a more complex surface-vegetation-atmosphere transfer scheme, which is a one-dimensional column model designed to represent the average characteristics of a horizontal grid square. The two schemes produced different partitioning of the fluxes and different precipitation distributions, and the simulated precipitation was closer to that observed using the more complex CLASS scheme. The results of Wen et al. (2000) suggest that the impact of land surface schemes can be significant in short-range, high-resolution precipitation simulations with complicated vegetation variations.

Lynn et al. (2001) use the fifth-generation Pennsylvania State University-National Center for Atmospheric Research Mesoscale Model (MM5), at nested resolutions of 15 and 5 km to test the effects of a sophisticated land-surface model (the Parameterization for Land-Atmosphere Convective Exchange (PLACE)) coupled to a 1.5 order TKE closure model (Gayno 1994; Shafran et al. 2000) for the simulation of an observed case

of widespread summertime moist convection over the Florida Peninsula. The PLACE model represents soil and surface hydrology in considerably more detail compared to force-restore, allowing soil moisture to change with time as it interacts with evaporation, rainfall, runoff, and soil water drainage to bedrock. The simulations using the 1.5 order TKE closure and the PLACE scheme produced the best overall skill in terms of biases of the surface variables, rainfall, and percent cloud cover, and correctly simulated an early isolated convective storm which did not develop in the control run, which used the standard MM5 land-surface scheme, the force-restore method (described earlier), coupled to a simpler first-order closure BL scheme. Lynn et al. (2001) conclude that the MM5 model required the combined, synergistic effect of the more detailed land-surface and turbulence schemes to produce the most realistic simulation of the convective event.

The parameterization of surface fluxes of heat, momentum, and moisture, such as the Louis scheme (Louis 1979), has been used extensively in global models as a simple, computationally efficient method, and is also commonly used within today's mesoscale models. The approach has been improved in recent years, most notably in the incorporation of different physical processes that have previously not been included in the calculation of the exchange coefficients. For example, the COARE algorithm (Fairall et al. 1996) gives special considerations for light wind conditions, corrections for sea surface temperature, effects of precipitation, and differences in roughness lengths for momentum, sensible, and latent heat fluxes in the calculation of the exchange coefficients. The COARE Algorithm, along with the Louis scheme, is an additional option for the surface flux parameterization in the Navy's COAMPS<sup>TM</sup> model. Andreas and Emanuel (2001) review recent numerical experiments of tropical cyclones where the effect of sea spray was included within the surface flux parameterization scheme for the high wind speed regime. Most of the tests concluded that adding the effects of sea spray affect the structure of the marine BL and the rate of tropical cyclone intensification. Andreas and Emanuel (2001) further conclude that the parameterization of sea spray effects must also consider the sensible heat flux given up by re-entrant spray droplets to more correctly estimate their effect on the exchange coefficients.

New and more complex boundary layer parameterization schemes have also been developed in recent years. BL parameterizations used in mesoscale models have evolved from the simpler parameterizations of BL turbulence using first order, local closure methods such as K-theory (also called gradient transport theory). First order closure based on K-theory, and local closure schemes in general, are described and evaluated in some detail in Stull (1988) and Holstag and Boville (1993).

First-order closure gives no information on turbulence intensity or temperature variance, and has difficulty with well-mixed layers that have zero gradients of mean variables. Hence, higher-order closure techniques are more advantageous for estimating flow within the BL. In recent years, BL parameterization schemes using higher-order, as well as non-local, closure methods have been developed for use within mesoscale models. However, with the increase in computational requirements and cost associated with these more complex schemes, today's mesoscale models commonly use schemes that combine higher order (typically 1.5 order) with local closure, or first order with non-local closure. For example, the scheme employed in COAMPS<sup>TM</sup> is a 1.5 order closure model based on the Mellor-Yamada level-2.5 model (Mellor and Yamada 1982) that includes a prognostic equation for turbulent kinetic energy. The fluxes are derived from a local-K approach, but unlike the formulations for the eddy diffusivity coefficients in the earlier schemes, in which the coefficients are functions of the bulk Richardson number, the eddy diffusivity in the COAMPS<sup>TM</sup> scheme is given a complex algebraic function involving the predicted mean and turbulent variables. Another more complex BL parameterization scheme is the Medium-range Forecasting (MRF) PBL scheme (Hong and Pan 1996), which is a first-order, non-local scheme where the tendencies are dependent on the bulk characteristics of the PBL and include counter-gradient transports of temperature and moisture that account for contributions from large scale eddies. The eddy diffusivity coefficients in the MRF PBL scheme are functions of the friction velocity and the PBL height.

Some testing of the sensitivity of these different boundary layer parameterization schemes has taken place. For example in Braun and Tao (2000) in the MM5 simulation of Hurricane Bob (1991) at high resolution (4 km), the model was able to produce, to

varying degrees, the track and intensity of the hurricane, but results exhibited strong sensitivity among different parameterization schemes. Simulated mean sea-level pressures and maximum winds varied by about 16 mb and  $15 \text{ m s}^{-1}$ , respectively, with the Burk-Thompson scheme producing the strongest storms, and the MRF PBL scheme producing the weakest storm. Simulated horizontal precipitation structures varied substantially between the different schemes as well, suggesting that accurate forecasts of precipitation in hurricanes can be just as sensitive to the formulation of the PBL parameterization as they are to the cloud microphysical parameterizations. Bright and Mullen (2002) evaluate the sensitivity within MM5 of four different BL schemes for the case of monsoon convection over Arizona, and conclude that the non-local schemes tested more correctly predict the development of deep, monsoon BL and associated convection.

Cloud parameterizations have also become more complex, particularly within the framework of mesoscale modeling. A traditional approach for cumulus parameterization, such as the widely used Kain-Fritsch scheme (Kain and Fritsch 1990), is appropriate for large-scale models at convectively unstable grid points for the creation of sub-grid scale (SGS) implicit clouds (Molinari and Dudek 1992). However, the traditional approach has been proven to be less well-posed within mesoscale models, or, for that matter, any model using grid spacing near 50 km and below (Cotton and Anthes 1989). Studies addressing this issue will be discussed in a later section concerning model parameterizations in high-resolution models. In addition to improvements in cloud parameterizations based on resolution, Deng et al. (2003) have developed a shallow-convection parameterization for use in mesoscale models. The scheme, which is based on the Kain-Fritsch scheme, is closely associated with BL turbulence processes, and can transition to either a deep-convection scheme in conditionally unstable environments, or to an explicit (resolved scale) scheme in moist stable environments. Results from initial applications of the shallow-convection scheme within the MM5 model, in both marine and continental environments, are consistent with observed mesoscale thermodynamic structures and local cloud-field parameters.

The most prominent improvement in mesoscale modeling is the increased ability to observe the atmosphere, both remotely and in-situ, and the effective incorporation of observations into model forecast through improved data assimilation techniques. Geostationary visible, IR, and microwave satellite observations are now routinely taken at 1-10 km spatial resolution, while geostationary and polar orbiting satellite systems use high-resolution spectral techniques to obtain remotely sensed high vertical resolution soundings. Polar orbiter high-resolution (~10 km) microwave scatterometers measure sea surface wind speed and direction. Space-based observations are enhanced with in-situ observations from various types of instruments, including radiosonde, dropwindsonde, wind profiler, and aircraft. Improvement of observation resolution in continental regions to the sub-10 km range comes via the addition of radar observations (the National Weather Service's Next-Generation Radar system) and mesonet observing systems. Internet capability makes all of this data readily available for use in regional mesoscale modeling efforts. Increased computational ability has also led to implementation and subsequent improvements within numerical models of three-dimensional and, most recently, four-dimensional variational data assimilation systems, to replace previously used optimum interpolation (OI) schemes (Parrish and Derber 1992, Rabier et al. 2000, Lorenc et al. 2000). Studies have shown that the variational data assimilation method creates a more accurate starting point for NWP integration, and is more flexible than the OI schemes, making it easier to incorporate new data sources and utilizing existing data better (Barker et al. 2003, Rogers et al. 2001).

In addition to improvements discussed above, horizontal grid resolution in NWP has also increased to add another dimension to the potential of improved forecasting in mesoscale NWP. The Navy's COAMPS<sup>TM</sup> is being applied operationally at 9 km, and, as discussed in Mass and Kuo (1998), several groups in the research community are experimenting with high-resolution NWP, with a number of efforts applying resolutions of 15 km or less. The NCEP Eta model will go into single digit resolution in the near future, with the recent acquisition of a massively parallel computer system, and its successor, the Weather Research and Forecasting Model (WRF) is being designed for resolutions between 1 and 10 km (Mass et al 2002). NCEP is also developing a Non-

hydrostatic Mesoscale Model (NMM) (Janjic et al. 2001), formulated specifically for high-resolution simulations, to better represent processes for which the hydrostatic approximation ceases to be valid. In addition, private sector companies are experimenting with high-resolution forecast systems to provide forecasts, at resolutions below 10 km, for major urban areas of the United States (Mass et al. 2002).

## **B. THE IMPORTANCE OF HIGH RESOLUTION MESOSCALE MODELING FOR NAVY OPERATIONS**

Mesoscale NWP models are used in the study and operational forecasting of terrain-induced and synoptically-induced atmospheric mesoscale weather systems (Pielke 2002). Terrain induced systems are defined as those forced primarily by surface inhomogeneities, such as sea breeze circulations, mountain-valley winds, forced flow over and around terrain, urban circulations, and lake effect precipitation. Synoptically induced mesoscale systems are those forced primarily by instabilities within moving larger scale disturbances, and include fronts and squall lines, convective bands in stratiform clouds, mesoscale convective systems, and tropical cyclones.

The capability to predict all of these types of mesoscale atmospheric phenomena is required to maximize the effectiveness of the U.S. Navy's battle group and amphibious ready group operations abroad. Any of the above weather scenarios is a potential environment for Navy surveillance, search, and strike operations, as well as the medium in which it must function without damage to platforms and personnel. U.S. Navy meteorologists supporting fleet operations in specific localized areas of interest use the Navy COAMPS<sup>TM</sup> atmospheric model as a primary tool to support and to maximize the effectiveness of operations. Accurate, high-resolution atmospheric model output would be extremely useful to the Navy forecaster providing guidance in fleet operations. Being able to accurately resolve the detail of flow fields around complex terrain to pinpoint regions of strong or turbulent winds, or to accurately forecast the location of strong convective activity near a cold front or mesoscale convective system, for example, would play a key role in the overall success of a particular mission.

One specific example where weather played a significant role in strike operations was during the air campaigns of the desert conflicts in the Middle East. Aircraft without

target radars are especially dependent on clear weather conditions for effective operations. For example, dust storms and low cloud cover were weather events that significantly affected air operations. These phenomena are usually short-lived and confined to specific areas, which can leave one airfield or target area in the dark or under cloud cover for hours, severely hampering visibility, while at the same time conditions are clear at another airfield or target 20 miles away. The development of high-resolution mesoscale models, that could accurately resolve flow fields affected by varying local terrain structure and coastal topography, are important tools in predicting these localized weather events and providing short-term forecasts for military flight operations.

As mesoscale model resolutions increase to the sub-km scales, it will be possible to resolve features at the turbulence scale such as BL roll vortices and clear-air turbulent eddies. While sub-km resolution modeling is not presently possible operationally, researchers are discovering its potential today. For example, Burk and Haack (2000) use COAMPS<sup>TM</sup> to model coastally-trapped wave clouds off the central California coastline using a horizontal resolution of 1/3 km, and present the highest real data forecast using COAMPS<sup>TM</sup> to date. The simulation accurately predicted long, lineal variations in the wind, temperature, and moisture fields, with modeled wavelengths  $\sim 4\text{km}$ , consistent with cloud features observed in satellite imagery. The ability to predict the development of these turbulent features, which have vertical updrafts-downdrafts of up to  $4\text{ ms}^{-1}$ , would offer considerable improvement to turbulence forecasting for low-level flight operations. The effort to improve short term forecast accuracy as operational mesoscale models attain increasingly higher resolution is critical to the Navy's mission.

### **C. PREVIOUS STUDIES IN HIGH RESOLUTION MESOSCALE MODELING**

Many previous studies have examined the effects of horizontal resolution on the accuracy of mesoscale NWP forecasts (Mass et. al 2002). Some examples of these studies, modeling different mesoscale weather phenomena at high horizontal grid resolution, are reviewed below. In most cases, subjective evaluation shows that increasing the horizontal resolution below 10-15 km produces more realistic, better-

defined structure of the atmospheric features being modeled. On the other hand, few studies have demonstrated that, objectively measured over time, forecast accuracy increases as grid spacing decreases below 10-15 km (Mass et al. 2002).

Mesoscale models are approaching the resolution necessary to resolve key features in regions of complex terrain that have a direct and significant impact on precipitation. Several studies (Bruitjes et al. 1995; Colle and Mass 1996; Gaudet and Cotton 1998; and Westrick and Mass 2001) have shown that, when run at sufficiently high resolution (down to ~10 km), mesoscale models can realistically simulate observed precipitation structures over complex terrain. Simulating gap flow through the Strait of Juan de Fuca using MM5, Colle and Mass (2000a) found that the sharp transition of the Strait-exit became more realistic as horizontal grid spacing was decreased from 12 to 1.33 km, but the simulation underestimated the winds by 2-5  $\text{ms}^{-1}$  in the gap exit region due to the 30% underestimation of the sea level pressure gradient down the strait. Colle and Mass (2000b) found significant improvement in precipitation forecast skill as grid spacing decreased from 36 to 4 km. For most locations, there was little overall improvement going from 4 to 1.33 km except along the upper windward slopes and in the immediate lee of major barriers, where precipitation amounts were enhanced with higher resolution.

Non-hydrostatic models employing grid spacings of 4 km or less have shown substantial success in duplicating observed structural evolution of a range of mesoscale convective systems (e.g., Weisman et al. 1988; Skamarock et al. 1994; Droegemeier et al. 1994). For example, Bernadet et al. (2000), simulating four high plains convective events from approximately 80- to 2-km grid spacing using the Colorado State Regional Atmospheric Modeling System (RAMS) model, found that 2 km was necessary to capture convection explicitly. In the simulation of Hurricane Danny, Kuo et al. (2001) found substantial improvement in the radius of maximum wind and the eye wall and rain band structures as horizontal grid spacing was reduced from 81 to 1 km. The 3 km resolution simulation produced a radius of maximum wind at 15 km consistent with radar observations, with results further improved using 1 km resolution. The study suggested that a grid resolution of at least 3 km was necessary to capture the wind field structure of

this small, minimal hurricane, and further suggests the use of 1 km resolution or higher to properly simulate the evolution of mesoscale convective systems and their interaction with the hurricane vortex.

Mid-latitude cyclones and frontal zones have been simulated using mesoscale NWP models at high resolution in several recent studies. Simulating a Pacific cold front with MM5, Chien et al. (2001) found that decreasing the grid spacing from 45 to 15 km did not greatly change the system's synoptic structure; however, decreasing the grid spacing to 1.67 km was necessary to produce the observed narrow frontal structure, associated convective rain band, and gravity-current head-like structure near the front's leading edge. In an MM5 simulation of a polar low that developed over the Bering Sea, Bresch et al. (1997) found that although a grid spacing of 6.7 km produced sharper mesoscale features than a 20 km resolution grid, the central pressure and synoptic scale structures were nearly the same at both resolutions. Buckley and Leslie (2000) found that decreasing grid spacing from 50 to 10 km in the University of New South Wales High Resolution Limited-Area Atmospheric Prediction (HIRES) model greatly improved the wind and central pressure forecasts for the Boxing Day storm of December 1998. In general, these and other subjective studies suggest that moving to high resolution (grid spacing less than 15 km) does produce better definition of frontal zones and other mesoscale weather features, but does not significantly improve the synoptic evolution of fronts and cyclones (Mass et al. 2002).

#### **D. HIGH RESOLUTION AND MODEL PARAMETERIZATIONS**

As stated earlier, Cotton and Anthes (1989) suggest that the conceptual basis for cumulus parameterization becomes unclear when model grid spacing falls below about 50 km. Along these lines, some researchers have eliminated cumulus convection in high-resolution models, and explicitly simulate cumulus convection at the grid scale (e.g., Yamasaki 1977; Rosenthal 1978). Other researchers have designed cumulus parameterizations with closure assumptions more appropriate for grid resolutions below 50 km (Fritsch and Chappell 1980; Frank and Cohen 1987). At resolutions typical of today's mesoscale models, on the order of tens of kilometers, the two schemes must be

used concurrently: an implicit parameterization scheme for the SGS convection, and an explicit scheme for modeling for larger-scale clouds resolved on the grid scale. Belair and Mailhot (2001) examine the relative roles of implicit and explicit convection schemes in the numerical simulation of a MCS and squall line using the MC2 mesoscale model at 2, 6, 18, and 50 km resolutions. At 2 km resolution, the explicit scheme is used alone, and the model realistically reproduces both the mesoscale and small-scale features of the system without the use of any parameterization. In the 6 km simulation, where the implicit scheme is employed for the SGS convection, both the convective and anvil regions of the MCS are still resolved by the model, but the leading convective band is less realistic (wider, shallower, and less intense) than in the explicit 2 km simulation. Belair and Mailhot (2001) explain that at 6 km resolution, the grid spacing is so close to the convective scale that the leading convective band of the squall system is barely resolved by the model, and is thus the implicit and explicit schemes coincidentally parameterize part of the convection. As previously emphasized in Frank (1983) and Molinari and Dudek (1992), the use of implicit schemes at resolutions between 3 and 10 km is in violation of the parameterization's fundamental assumptions and closure hypothesis. Belair and Mailhot (2001) state that because of the lack of separation between the convective and grid scales, results obtained from models at these intermediate resolutions must be examined cautiously. Belair and Mailhot (2001) conclude that the necessity to parameterize convection, even at this high resolution, should encourage researchers to find ways to represent the effects of unresolved convection in the gap between the scales of direct simulation of clouds ( $\sim 100$  m) (Arakawa and Chen 1987) and  $\sim 10$  km, where explicit modeling of clouds is insufficient to represent the convection realistically.

The treatment of SGS turbulence, similar to that of convection, becomes less well posed as the horizontal resolution increases. As resolution increases into the turbulent scale, the appropriateness of the turbulence parameterization scheme itself now becomes questionable, and the need to re-evaluate the appropriateness of turbulence parameterizations arises. Belair et al. (1998) addressed the issue of approaching the turbulence scale in high-resolution numerical modeling. They assessed the impact of

increasing the horizontal resolution from 10 km to 1 km on the simulation (using the French MESO-NH limited area model) of surface and turbulent fluxes in a field experiment over cultivated land and forest regions in southwestern France. Comparing the model output with aircraft measurements, they found that the increased resolution to 1 km showed much smaller scale detail in the parameterized fluxes and turbulent kinetic energy, but there were oscillations in the parameterized quantities that did not appear reasonable. They conclude that since a non-negligible portion of the turbulent fluxes are technically resolvable by the 1 km model, this portion of the energy should not be parameterized by the turbulent scheme, which is designed to parameterize the vertical mixing based on the *total ensemble* of turbulent energy. Their study thus indicates that at intermediate resolutions (between 200 m and a few kilometers) the interpretation of model output relating to turbulent quantities is complicated, and that the higher resolution does not necessarily improve the simulation of the turbulence. This raises the questions: at what resolution should the validity of SGS parameterization be questioned, and how can we properly parameterize the SGS processes when the model resolution is close to the scale of turbulent eddies? These questions have no known published answers, and are key issues of this study.

## **E. OBJECTIVES OF RESEARCH**

While the Navy operational COAMPS<sup>TM</sup> is currently using an 81-27-9 km nest, the inevitable increase in available computing power, both at Navy METOC centers and afloat, will allow even higher resolution model runs to become operational. With this eventuality and the discussion in the previous section in mind, the main goal of this study is to answer the basic questions and better understand the issues relating to the grid resolution dependence of turbulence parameterizations in mesoscale models where the resolution approaches the scale of turbulent eddies. Understanding the scale of turbulence, and the factors affecting it, is also an important objective in determining in the appropriateness of ensemble turbulence parameterization in a high-resolution numerical simulation when the grid resolution approaches the scale of turbulent eddies. Through analyses of a numerical simulation using a case study of cold air outbreak

conditions over the Japan/East Sea (JES), we explore the capability of the current COAMPS<sup>TM</sup> turbulence parameterization scheme, at high resolution, in simulating the boundary layer turbulence mixing. Results from these simulations are compared with those from direct measurements. Based on results from the above analysis, we attempt to modify the existing COAMPS<sup>TM</sup> turbulence parameterization towards more realistic representations of the turbulent processes. The modification will be applied within COAMPS<sup>TM</sup> for the same case study, and results of the control and modified simulations will be compared and verified against observations to determine if improvement was indeed made.

## **F. SUMMARY OF DISSERTATION**

Chapter II contains background information on turbulent scales, the ensemble turbulence parameterization scheme used within COAMPS<sup>TM</sup>, and mixing length formulations used within different BL turbulence parameterization schemes. Chapter III contains an observational analysis of the scale of turbulence and the integral length scale. The analysis, which utilizes aircraft observations from three different convective BL field experiments, provides the conceptual basis for modifications made to the COAMPS<sup>TM</sup> mixing length used in the turbulence parameterization scheme. In chapter IV, an in-depth analysis of the JES cold air outbreak case study is performed, where the BL structure from aircraft observations is compared with that simulated in the COAMPS<sup>TM</sup> control run. It is determined that the model poorly simulates the observed BL turbulent structure, in terms of the spatial variability near the minimum resolvable scale. Chapter IV also includes a background discussion of horizontal roll vortices, which are observed in the BL for this case study. Chapter V explains modifications made to the COAMPS<sup>TM</sup> mixing length, which is applied within the model for the JES cold air outbreak case study in an effort to improve the simulated spatial variability. The results from the simulation with modified mixing length are compared to that of the control run to determine if improvement in the simulated BL structure is achieved. Chapter VI provides a project summary and conclusions, and recommendations for further study of this issue.

THIS PAGE INTENTIONALLY LEFT BLANK

## II. BACKGROUND

### A. PHYSICAL PROCESSES GENERATING BOUNDARY LAYER TURBULENT KINETIC ENERGY

Modeling of BL turbulence in COAMPS<sup>TM</sup> is the main focus of this research, thus it is important to understand the various physical processes that act to generate and maintain turbulence there. The BL is that layer of the atmosphere directly influenced by the earth's surface, responding to surface forcings on a time scale of 1 hour or less, and contains a significant amount of turbulent energy (Stull 1988). The height of the BL top is dependent on the balance between the strength of the subsidence in the free atmosphere and the strength of turbulence within the BL. The vertical motions generated by turbulence act to mix heat, moisture, and momentum fluxes generated at the surface upward.

Turbulent kinetic energy (TKE) is a measure of the intensity of turbulence in the BL, and is directly related to the momentum, heat, and moisture transport through the BL. The individual terms of the TKE budget equation (time tendency of TKE) describe the physical processes that generate turbulence. Here we present a simplified version of the TKE budget equation for the purposes of describing the important processes which generate TKE in the BL. The simplified TKE budget equation for a field with horizontal homogeneity (Stull 1988),

$$\frac{\partial \bar{e}}{\partial t} = \underbrace{\frac{g}{\theta_v} \overline{w'\theta_v'}}_{\text{I}} - \underbrace{\overline{u'w'}}_{\text{II}} \frac{\partial \bar{U}}{\partial z} - \underbrace{\frac{\partial \overline{(w'e)}}{\partial z}}_{\text{III}} - \underbrace{\frac{1}{\rho} \frac{\partial \overline{w'p'}}{\partial z}}_{\text{V}} - \underbrace{\varepsilon}_{\text{VI}}, \quad (2.1)$$

assumes a coordinate system aligned with the mean wind, no horizontal advection of TKE, and neglects subsidence. Term I represents the local storage or tendency of TKE. Turbulent kinetic energy (TKE) is generated through buoyancy production (term II) and shear production (term III), mainly occurring in the lower half boundary layer. A positive buoyancy flux generates TKE and represents the effects of thermals in the convective BL; for example, a warm, sunny day over land or the advection of cold air

over a relatively warmer surface. Static stability tends to suppress or consume TKE as it generates negative buoyancy flux. Such conditions are present in the stable BL at night over land, or when the surface is colder than the overlying air. Shear production occurs in the presence of a mean wind shear. The interaction tends to generate more turbulence, since the two terms are usually of opposite sign, and thus shear production is a positive term in the TKE budget equation. Term IV is the vertical flux of TKE, and represents the vertical transport of TKE by turbulent eddies. This term is not a production or loss term (its value is zero when integrated over the depth of the BL), but acts to redistribute TKE within the BL. Term IV is generally negative in the lower half of the BL, as turbulence generated there by shear and buoyancy production is transported to the upper half of the BL, where term IV is generally positive. Term V is a pressure correlation term, which describes how TKE is redistributed in different directions. Little is known about this term from observations, and it is often calculated as the residual required to balance the other terms in the TKE budget. Term VI is the dissipation of TKE, representing the molecular destruction of turbulent motions. Turbulent energy is dissipated within the BL through the energy cascade process, discussed in the next section, and the magnitude of this dissipation rate is proportional to the rate of TKE production. Dissipation occurs primarily within the smallest turbulent eddies, at the smallest scales, while production of TKE occurs in the largest turbulent eddies. Thus, the production and loss mechanisms defined in the TKE budget occur on completely different scales. Figure 2.1 is a figure from Stull (1988) that shows the variation of the terms with height within a fair weather convective BL. The relative magnitudes of the terms shown in the figure are derived from several data and models from several different experiments.

While not the focus of this study, entrainment is an important BL process that responds to and feeds back to turbulence in the BL, and is a mechanism for exchange between the BL and the free atmosphere. Entrainment of above BL air from the free atmosphere into the BL is the mechanism for BL vertical growth, and allows the free atmosphere to interact with the BL and respond to changes in surface forcing. In the clear BL, turbulent eddies rising through the BL become negatively buoyant as they reach

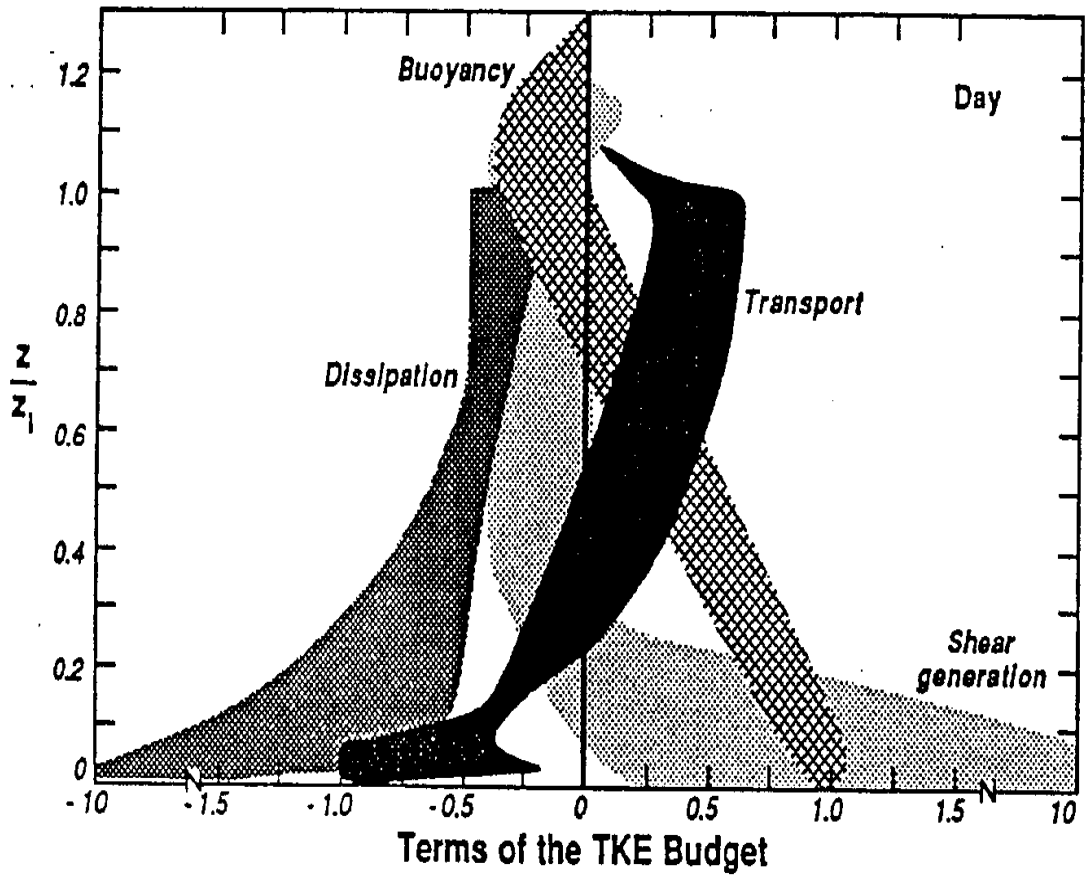


**Figure 2.1.** Terms in the TKE budget equation, normalized by BL height. Shaded areas indicate ranges of values. From Stull (1988).

the inversion, but overshoot into the free atmosphere before sinking back into the BL. During the overshoot into the inversion, some free atmospheric air is pushed into the BL and is rapidly mixed into the BL because of the strong turbulence there, and results in a one-way entrainment process allowing the BL to grow in thickness. If clouds are present in the BL, warm air from above the BL entrained into the top of a cloud can cool and sink through evaporation of cloud droplets. This, along with IR cooling at the cloud top, form negatively buoyant downdrafts generating more turbulence that enhance BL mixing and entrainment. Because the strength of the entrainment is directly proportional to the strength of BL turbulence, changes to the free atmosphere are dependent upon the extent of turbulent flow within the BL.

## **B. SCALES OF MOTION IN THE ATMOSPHERE**

### **1. Atmospheric Energy Spectrum**

Atmospheric flow as a whole can be described as eddies of different sizes, each carrying a certain amount of kinetic energy. This is best shown in the sketch of the energy density spectrum of wind speed (Figure 2.2). Here, the leftmost peak corresponds to kinetic energy associated with synoptic scale phenomena. The spectral minimum at about 1 hour allows for a separation of scales between the synoptic and mesoscale features, or mean flow, with microscale features, or turbulence, in the BL. In this gap region is where several special mesoscale types of flow are known to exist, such as deep convection, large roll vortices, and local circulations such as land/sea breezes (Smedman and Höögström 1975). Because of these phenomena, the “gap” is sometimes not well-defined, and is likely to contain different types of motion, which fortunately are distinctly varied in terms of spectral signature. The remainder of the spectral energy to the right of the gap is associated with turbulent energy within the atmospheric BL. Note that the relative magnitudes of the synoptic scale and turbulent scale spectral peaks in Figure 2.2 are for illustrative purposes only and are not to scale; synoptic scale energy is in reality 2 or more orders of magnitude larger than turbulence scale energy. The magnitude of TKE will be illustrated clearly in Chapter III.

## 2. Turbulent Energy Spectrum

Turbulence is the gustiness superimposed on the mean wind (Stull 1988) and can be visualized as irregular swirls of motion, known as turbulent eddies. The rightmost peak in the atmospheric energy spectrum of Figure 2.2 is associated with the energy-containing turbulence eddies within the atmospheric BL. These eddies are on the scale of the BL depth, roughly 100 m to 3 km in diameter and are produced directly by the dynamic instability of the mean flow via shear or buoyancy effects. The smallest eddies (on the order of a few millimeters in size) are called the dissipation eddies because of the dissipating effects of molecular viscosity. Eddies that scale on the order of centimeters to 100 m, exist on a scale known as the inertial sub-range, and are produced by the energy cascade process from the large eddies. There is a net transfer of energy from the largest to the smallest eddies, where large eddies create eddy-size wind shear regions that generate smaller eddies, a cycle which continues until the smallest eddies dissipate into heat via molecular viscosity. After many cascade processes, the eddies become so small and contain so little energy that they are no longer considered a mechanism in the transfer of momentum and heat, and are much less dependent on the flow than large eddies. The issue of understanding the scales of turbulence is important to improved high resolution simulations of BL turbulent motions, and will be addressed in great detail in Chapter III, through the analysis of turbulence spectra from high rate aircraft observations.

## 3. Scales of Atmospheric Turbulence

Several length scales have been used to denote the size of turbulent eddies. Some of the more commonly used length scales are presented in Kaimal (1973). The integral length scale ( $\Lambda$ ) is the classical length scale of fluid mechanics, and is obtained from the integral time scale ( $\tau$ ) using Taylor's "frozen field" hypothesis (Taylor 1938) using

$$\Lambda = U\tau = U \int_0^{\infty} \rho(t) dt \quad , \quad (2.2)$$

where  $\rho(t)$  is the autocorrelation coefficient. The wavelength corresponding to the peak of the logarithmic power spectrum ( $\lambda_m$ ), also derived using Taylor's hypothesis, is

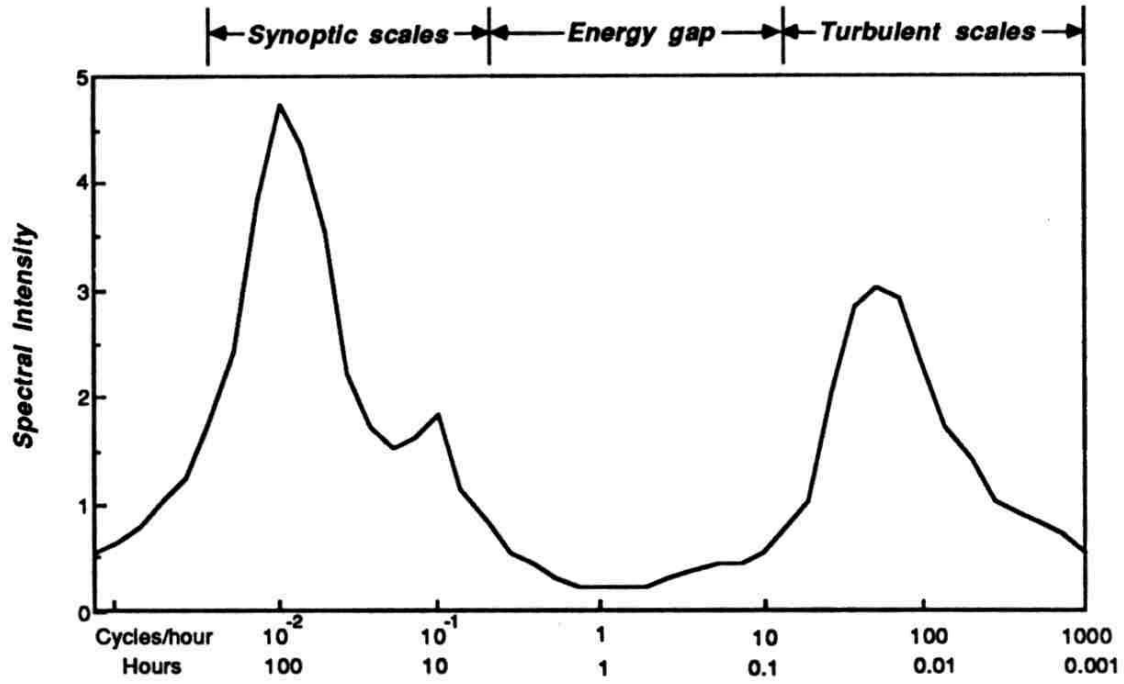


**Figure 2.2.** Spectra of wind speed near the surface, illustrating the scales of motion within the atmosphere. From Stull (1988).

$$\lambda_m = U / f_m, \quad (2.3)$$

where  $f_m$  is the peak frequency. This length scale is widely used in the interpretation of atmospheric spectra, since it can be derived directly from the logarithmic power spectrum, and will be used in the work presented here in our discussion of turbulent length scales.  $\Lambda$  and  $\lambda_m$  are related empirically in Kaimal (1973) by

$$\lambda_m = 2\pi\Lambda. \quad (2.4)$$

Several studies have addressed the scales of turbulence by analyzing the spectra of velocity components and temperature using observations taken within the surface layer and outer layer of the BL. Studies of this nature also provide insight into the physical mechanisms that are active in the turbulent transfer processes in the BL. Some of these studies, pertinent to the work presented here, are reviewed below. The discussion will focus mainly on the vertical velocity spectra and length scales, and will be referenced later in the analysis of vertical velocity spectra from different experiments over the ocean.

Much of the pioneering work in the study of turbulent energy spectra utilized similarity theory (Kolmogorov 1941; Obukov 1941) to normalize spectral intensities according to scaling variables appropriate to the flow. This approach allowed researchers to organize results and generalize the behavior of turbulence. For example, turbulent eddies in the inertial sub-range obtain their energy inertially from larger eddies and lose their energy in the same way to smaller eddies. For a steady state turbulent flow, the cascade rate of energy down the spectrum must balance the dissipation rate at the smallest eddy sizes. Thus, three variables govern this process: spectral intensity ( $S$ ), the wavenumber ( $\kappa$ ) and the dissipation rate ( $\epsilon$ ). Dimensional analysis leads to an equation for the spectral intensity in the inertial sub-range,

$$S_\kappa = \alpha \epsilon^{2/3} \kappa^{-5/3}, \quad (2.5)$$

where  $\alpha$  is the Kolmogorov constant, with a typical value around 1.5 (Gossard et. al 1982). This relationship has allowed for the determination of the inertial sub-range within any measured spectrum, since the plot of  $S$  vs.  $\kappa$  on a log-log scale would present a straight line portion of slope  $-5/3$ , indicating the location of the inertial sub-range.

Kaimal et. al (1972) studied the behavior of turbulence spectra in the surface layer, defined as the lowest  $\sim 10\%$  of the BL (Stull 1988), within the framework of similarity theory. The study utilized data obtained within a surface layer over flat grasslands. The goal of their study was to define the general behavior of velocity and temperature spectra for different heights within the surface layer and under different conditions of stability. In their approach to this goal, the spectra were collapsed into coincidence in the inertial sub-range, by normalizing the velocity and temperature spectra to remove the dependence on stability there. The ability to collapse the curves by removing the stability dependence implies that the smaller eddies in the inertial sub-range receive all of their energy via the cascade process from larger eddies, with no direct interaction with the mean flow or mean stratification. The result allows the observation of the variation in the spectra as a function of stability above the inertial sub-range, at the scale of energy-containing eddies. The resulting generalized spectral curves, derived from the normalized  $w$  spectra, are plotted for a range  $z/L$  values from stable (2.0) to unstable (-2.0) for vertical velocity ( $w$ ) in Figure 2.3. The curves provide some important implications for the characteristics and the scales of turbulent flow in the surface layer.

One notable feature of the spectrum of the stable surface layer is its shape, which is insensitive to changes in height and stability. Also, we see that the peak spectral intensity is reduced as the stability increases. This is a reasonable result, since stability opposes turbulent motions. We also observe a shift toward higher frequencies, or smaller scales, of the peak spectral intensity as stability increases, possibly due to stronger damping by buoyancy forces at the lower frequencies (Stull 1988). The stippled region for the range  $-0.3 > z/L > -2.0$  indicates the absence of any well-defined trend or conformance to a single shape in the spectra for the unstable region, where the systematic progression seen on the stable side breaks down as  $z/L$  changes sign. The generalized results from Kaimal et al. (1972) were consistent with surface layer spectra reported by other investigators. Kaimal (1973) further extended the use of similarity theory to bring the spectra in the stable surface layer into one universal curve, by developing a modified frequency scale. In establishing a relationship between this new frequency scale and stability, Kaimal determined that the integral length scale of eddies in the stable surface

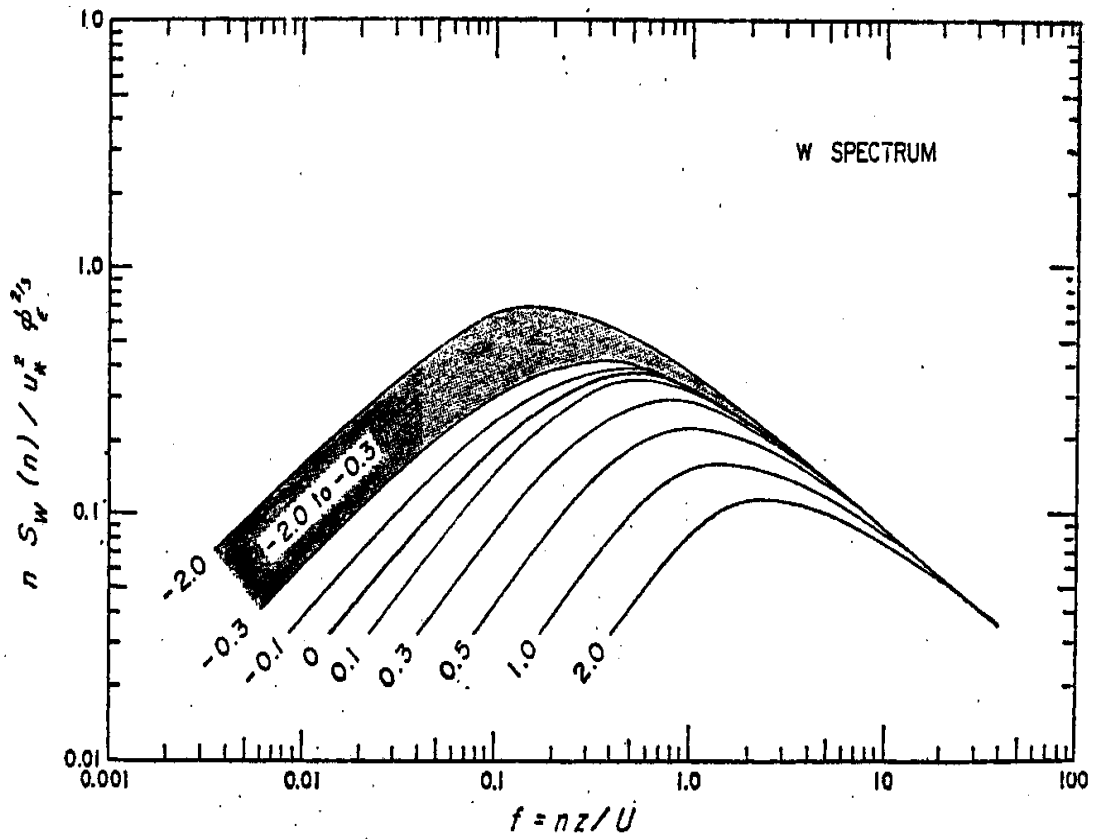


**Figure 2.3.** Generalized surface layer vertical velocity spectrum for  $z/L$  values ranging from +2.0 to -2.0. From Kaimal et. al (1972).

layer was inversely proportional to the Richardson number ( $R_i$ ). Kaimal also generalized that the scale of eddies in the stable surface layer becomes more proportional to height as stability decreases. These studies provided a comprehensive picture of surface layer turbulent structure and the size of surface layer turbulence, but also indicated a need for similar work at higher levels in the BL, since it appeared that surface layer turbulence was strongly influenced by scales of motion large enough to encompass the whole BL.

Kaimal et al. (1976) were able to similarly generalize the spectra in the convective mixed layer (ML) using similarity theory. This experiment utilized observations from various levels in the surface layer and ML within a well-mixed, daytime convective BL over flat land. They found that, within the ML, the energy in the inertial sub-range remained essentially constant with height, and the spectral peaks were invariant in intensity and location on the frequency scale. This near uniform spectral behavior over much of the BL allowed for the generalization of the normalized ML spectra expressed in mixed layer similarity coordinates. Figure 2.4 shows the generalized mixed layer spectra for the velocity components. At lower frequencies the velocity spectra separate as a function of  $z/z_i$ , (where  $z_i$  is the height BL top). The large spread with height between vertical velocity spectra implies that the scales of vertical velocity are strongly dependent on the  $z/z_i$  compared to the horizontal velocity components, which only have two closely separated general ranges of  $z/z_i$ . As  $z/z_i$  increases from .01 to 1.0, the position of the spectral peak for  $w$  shifts to lower frequencies (larger scales). For  $u$  and  $v$ , there is virtually no shift in the peak for different  $z/z_i$ . Kaimal et. al. (1976) also investigate  $\lambda_m$  as a function of  $z/z_i$  (Figure 2.5). We see from the figure that for  $w$ , a near-linear relationship exists between the dimensionless peak wavelength and  $z/z_i$ , in the surface layer (up to  $0.1z_i$ ) where

$$\lambda_m / z_i = 5.9z / z_i. \quad (2.6)$$

Above the surface layer,  $\lambda_m$  is seen to increase more gradually up to about  $0.5z_i$ , and approaches a constant value of  $\sim 1.5z_i$  in the range  $0.5z_i < z < z_i$ . The horizontal wind components  $u$  and  $v$  show virtually no variation in  $\lambda_m$  with height. For temperature, the  $\lambda_m$  increases linearly with height in the surface layer, while for  $z > 0.1z_i$ ,  $\lambda_m$  increases

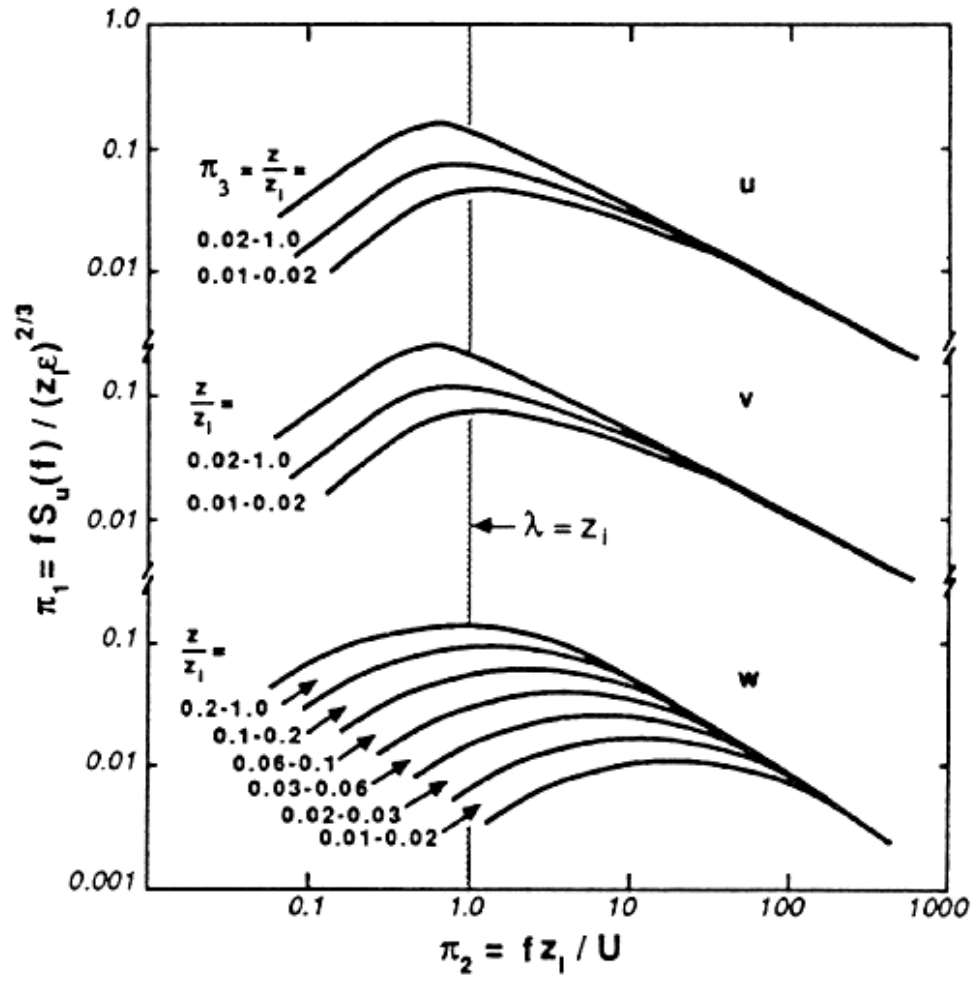


**Figure 2.4.** Generalized mixed layer spectrum of  $u$ ,  $v$ , and  $w$  for various  $z/z_i$  values. From Kaimal et. al (1976).

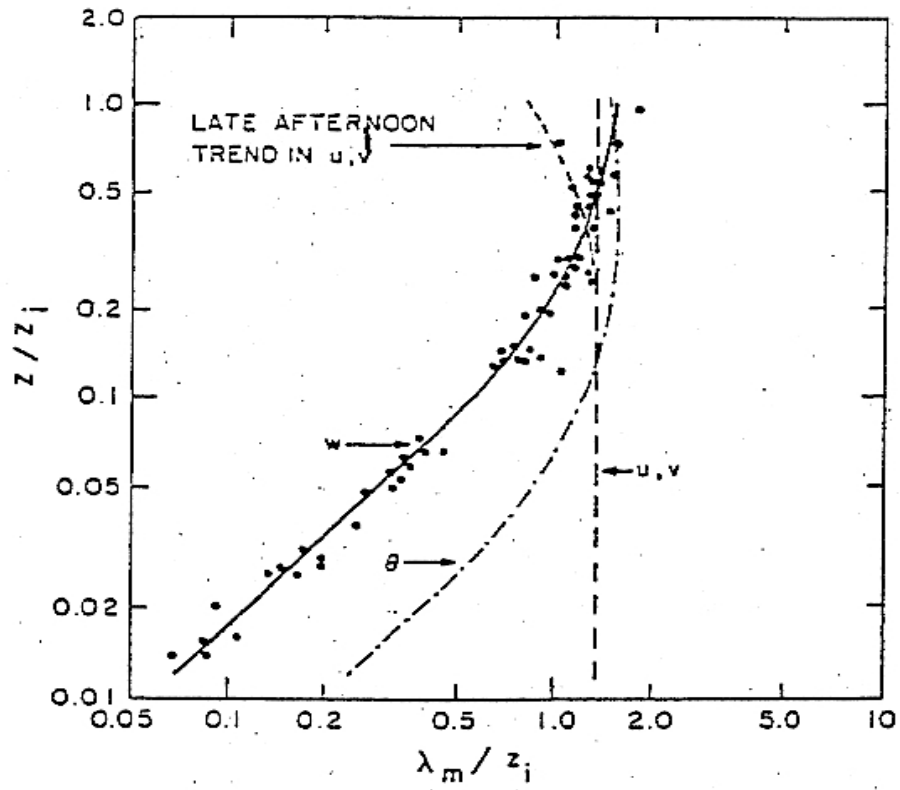


**Figure 2.5.** Dimensionless peak wavelength ( $\lambda_m$ ) for the velocity components and temperature plotted as a function of  $z/z_i$ . From Kaimal et. al (1976).

slightly with height up to  $0.5z_i$ , then decreases slightly above  $0.7z_i$ . In general, the results show that in the mixed layer, the maximum wavelength for all components is roughly equal to  $1.5z_i$ , which corresponds to the length scale of large thermals that dominate the convective BL circulation over land.

While the previously mentioned studies involved the analysis of spectra using observations over land, Grossman (1982) performed spectral analysis using aircraft observations of vertical velocity over the ocean, within the trade wind region near Barbados. His goal was to test the hypothesis that a hierarchy of physical mechanisms (the major division of this hierarchy being roll vortex motion and cellular convection), responding to wind shear and buoyancy forcing, is active in the generation of turbulent eddies within the oceanic sub-cloud layer. Using cases from near-neutral and near free-convective conditions for both along and cross wind runs, at levels of 18, 46, and 152 m within fair weather BLs that averaged around 600-900 m in depth, Grossman (1982) compares the characteristics of the vertical velocity spectra, which, regardless of stability or wind direction orientation, showed a shift toward larger values of  $\lambda_m$  with increasing height. The over-ocean spectra at all levels also reveal a double peak in the vertical velocity spectra, at the 1-2 km scale and at the 100's of m scale. The remaining discussion here will focus on the cross-wind vertical velocity spectra at different levels for the case in near free-convective conditions (shown in Figure 2.6), which is most applicable to this study. The  $\lambda_m$  for the 1-2 km peak is invariant with height, while the 100's of m peak shifts to a longer  $\lambda_m$  with height. The variance for both the 1-2 km peak and the 100's of m peak at the  $\lambda_m$  increases with height. Based on the relatively constant  $\lambda_m$  of the spectra peak at 1-2 km, he concludes that the limiting size of eddies over the ocean is roughly  $2z_i$  (1.2 to 1.8 km for the cases studied), which appears to apply regardless of stability or orientation to the horizontal wind direction. These findings are in close agreement with over-land studies of vertical velocity spectra in the surface layer and ML discussed previously. Grossman (1982) states that the spectral results presented in his study give insight to the nature of physical mechanisms occurring within these BLs. For instance, the spectral signature at 18 m shows eddies on the scales of 100's of m, likely generated by convective cells of similar scales, are co-existing with

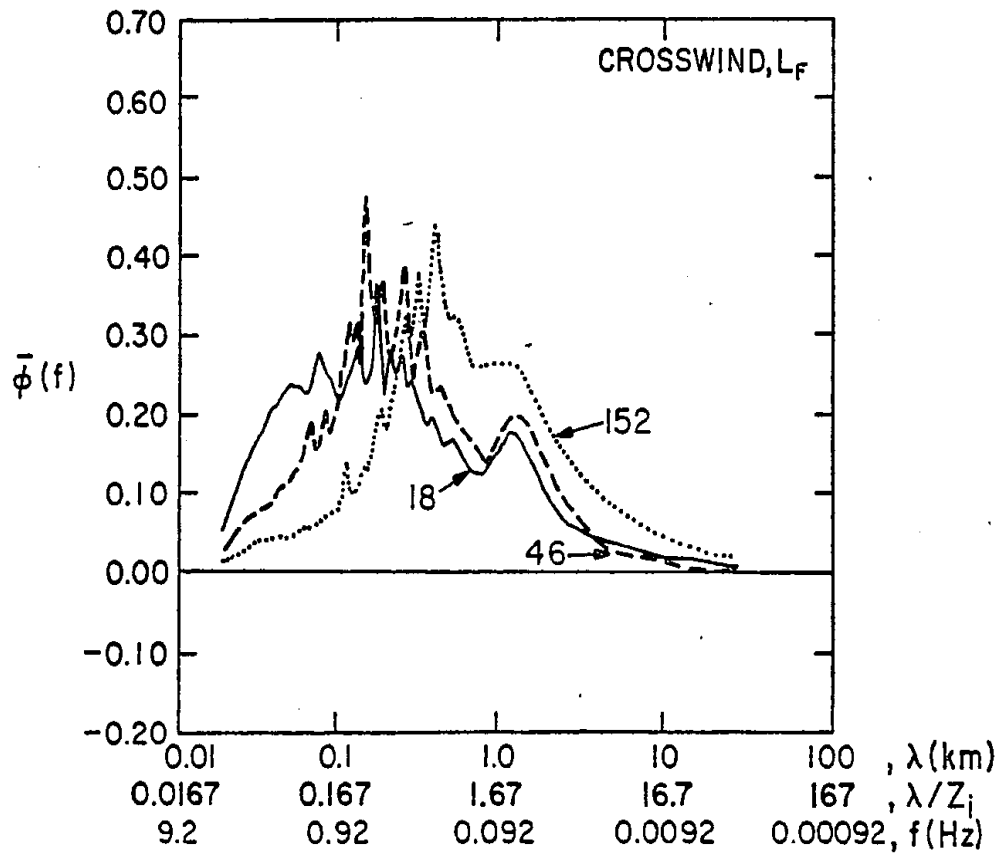


**Figure 2.6.** Vertical velocity spectra over the ocean for a convective BL. Each line represents the spectra from a different vertical level within the BL, as indicated (height in m). From Grossman (1982).

eddies in the km scales, likely generated by larger scale linear structures such as roll vortices.

## **C. REPRESENTATION OF TURBULENCE IN NUMERICAL MODELS**

### **1. Direct Numerical Simulations**

In an idealized sense, a direct simulation of BL turbulence would mean that the turbulence is fully resolved. No turbulence closure would be used, and the goal is to solve the full equations of motions with explicit molecular diffusion terms. For this type of model to succeed, the grid resolution of the model must be finer than the smallest scale of turbulent eddies in the solution. The direct application of the model equations is limited to spatial scales on the order of about 1 cm and time scales of less than 1 second (Pielke 2002), and to represent the atmosphere accurately, the equations must be evaluated over those space and time intervals. Thus, a direct simulation, resolving down the finest scales of turbulent dissipation, of mesoscale circulations (which scale on the order of 10 to 100 km in the horizontal, and up to 10 km in the vertical) would require solutions at  $10^{18}$  to  $10^{20}$  grid locations. This far exceeds the capacity of any existing or foreseeable computer system. Thus, there will likely always be a requirement to account for unresolved motions to some degree in mesoscale NWP.

### **2. Large Eddy Simulations**

The Large Eddy Simulation (LES) is in a middle ground between direct and ensemble-average simulations. The horizontal grid resolution is high, typically less than 100 m (within the inertial sub-range of turbulence), with simulation time steps of less than 10 seconds. The numerical simulation explicitly describes the large-scale turbulence and associated fluxes of heat and momentum, and a turbulence closure scheme represents the unresolved small scale motions, mainly accounting for the dissipation of the resolved turbulence energy, at scales below the inertial sub-range. In general, LES models perform well by explicitly resolving the large eddy energy well. The SGS energy, due to the dissipation eddies, is dependent on the parameterization scheme, but most studies conclude that LES model results are insensitive to the small scale turbulence closure, except near boundaries and regions of static stability (Mason 1994). This insensitivity stems from the fact that small eddies contribute much less heat and momentum transport

than the large eddies. Because these types of simulations explicitly resolve large-scale turbulent eddies, LES modeling has been very successful in research as a means of both predicting the flow properties of specific turbulent flows and providing flow details which are often used by researchers as a substitute for real observations for testing and refining turbulence closure models. However, the high vertical and horizontal resolution required for LES modeling is computationally restrictive, limiting its use operationally.

### **3. Ensemble Turbulence Closure**

In contrast to direct simulations, models with ensemble turbulence closure only numerically describe the mean flow, where the equations of motion for resolved flow are averaged continuously in space over a volume  $\Delta x \Delta y \Delta z$ . Therefore, a calculated variable centered at some grid point represents the average over the surrounding grid volume. The ensemble properties of all fluctuations in the flow (i.e. turbulent eddies) are assumed to take place on scales smaller than the resolvable scale of the model grid resolution, called the sub-grid scale (SGS). These turbulent eddies are not modeled directly, but instead must be represented through parameterizations based on the resolvable mean quantities. The accurate parameterization of surface and BL turbulent fluxes in numerical models has been a particularly challenging task, and the schemes used are far from perfect, but ensemble-average simulations are less limited by computer resources than direct or LES simulations and are often the only option in modeling some weather systems.

When operating at high resolution, most mesoscale models, including COAMPS<sup>TM</sup>, use grid resolutions that fall within the scale of turbulence. In this case, some of the larger-scale turbulent eddies are explicitly resolved, although the BL turbulent mixing processes are generally represented through ensemble parameterization schemes. Some of the different BL turbulence parameterization schemes used in mesoscale NWP models were briefly discussed in chapter I. The BL turbulence parameterization scheme specifically used in COAMPS<sup>TM</sup>, which will be used in our study, will be described in the next section.

#### D. COAMPS<sup>TM</sup> ENSEMBLE BL PARAMETERIZATION SCHEME

In this section we discuss the parameterizations used to represent the planetary boundary layer in the COAMPS<sup>TM</sup> mesoscale model. The grid-volume averaging of simplified prognostic equations for the mean variables within mesoscale models results in averaged vertical sub-grid scale fluxes that must be parameterized since they cannot be resolved by the model. Vertical sub-grid scale fluxes are reasonably well-understood and can be parameterized accurately in terms of dependent variables, i.e., the fluxes are specified using experimental data and fundamental concepts. In developing sub-grid scale averaged quantities, the preferred representation is an ensemble average over the grid volume, rather than a simple grid-volume average (Pielke 2002). The ensemble average represents the most likely value of the sub-grid scale quantity, whereas the grid-volume average represents just one realization. Wyngaard (1982, 1983) and Cotton and Anthes (1989) discuss ensemble averaging in more depth.

As mentioned in chapter I, COAMPS<sup>TM</sup> uses a one-and-a-half (1.5) order closure ensemble parameterization scheme based on the Mellor-Yamada level 2.5 model (Mellor and Yamada 1982, hereafter MY82) for BL turbulence parameterization. The 1.5 order closure retains the equations for the vertical variances in the mean equations, with a prognostic equation for TKE used in place of the velocity variance equations. In addition, eddy coefficients are based on K-theory for the vertical flux terms, which results in the algebraic simplification of the variance equations in terms of empirical constants and the parameterized fluxes. The resulting COAMPS<sup>TM</sup> prognostic TKE equation is

$$\frac{D}{Dt} \left( \frac{e^2}{2} \right) - \frac{\partial}{\partial z} \left[ l e S_e \frac{\partial}{\partial z} \left( \frac{e^2}{2} \right) \right] = +P_s + P_b - \varepsilon \quad (2.7)$$

where  $e^2$  is the TKE and  $l$  is the vertical mixing length scale (discussed in the next section). The second term on the left side represents the turbulent diffusion of TKE (Mellor 1973).

$$P_s = -\overline{w'u'} \frac{\partial U}{\partial z} - \overline{w'v'} \frac{\partial V}{\partial z} \quad (2.8)$$

is the shear production term,

$$P_b = \beta g \overline{w' \theta'_v} \quad (2.9)$$

is the buoyancy production term, with  $g$  the acceleration due to gravity and  $\beta$  a constant, and  $\theta_v$  the virtual potential temperature. The dissipation rate,  $\varepsilon$ , can be parameterized as

$$\varepsilon = \frac{e^3}{\Lambda_1}, \quad (2.10)$$

where  $\Lambda_1$  is the dissipation length scale. The vertical fluxes are parameterized in the prognostic TKE (and in the mean equations) using K-theory as

$$-\overline{w'u'} = K_m \frac{\partial U}{\partial z} \quad (2.11)$$

$$-\overline{w'v'} = K_m \frac{\partial V}{\partial z} \quad (2.12)$$

$$-\overline{w'\theta'_v} = K_h \frac{\partial \theta_v}{\partial z}, \quad (2.13)$$

where

$$K_{m,h,e} = leS_{m,h,e} \quad (2.14)$$

and  $S_m$ ,  $S_h$ , and  $S_e$  are functions of the gradient Richardson number,  $R_i$ , where

$$R_i = \frac{g}{\theta_v} \frac{\frac{\partial \theta_v}{\partial z}}{\left(\frac{\partial U}{\partial z}\right)^2 + \left(\frac{\partial V}{\partial z}\right)^2}. \quad (2.15).$$

Inserting all of the parameterizations into the TKE equation gives the parameterized TKE equation used in COAMPS<sup>TM</sup>:

$$\frac{D}{Dt} \left( \frac{e^2}{2} \right) - \frac{\partial}{\partial z} \left[ leS_e \frac{\partial}{\partial z} \left( \frac{e^2}{2} \right) \right] = +K_m \left( \left( \frac{\partial U}{\partial z} \right)^2 + \left( \frac{\partial V}{\partial z} \right)^2 \right) + \beta g K_h \frac{\partial \theta_v}{\partial z} - \frac{e^3}{\Lambda_1}. \quad (2.16)$$

## E. FORMULATIONS OF VERTICAL MIXING LENGTH SCALES WITHIN BL TURBULENCE PARAMETERIZATION SCHEMES

Most turbulence parameterization schemes use, as a closure assumption, a vertical mixing length scale (hereafter referred to as mixing length), which represents some measure of the intensity of turbulence mixing. Stull (1988) details the development and use of mixing length theory, from which the mixing length formulation is based on. Mixing length formulations are often developed by trial and error, in an attempt to make the simulated flow field match observed field or laboratory cases. Turbulence models have been shown to be sensitive to the choice of mixing length formulation (Therry and Lacarrere 1983), and thus several formulations for mixing length exist in the literature, with some being very specific to different BL structures and characteristics. To illustrate this, some brief examples of different formulations are provided below. The vertical profile of mixing length within the BL, as modeled in COAMPS<sup>TM</sup>, will be graphically presented and its formulation discussed in further detail in chapter IV.

One of the simplest formulations of mixing length, normally only appropriate for use in LES modeling, is the approach first proposed by Smagorinsky (1963). The Smagorinsky model (followed by Lilly 1967, Deardorff 1972, Klemp and Wilhelmson 1978) calculates a basic mixing length,

$$l = (\Delta x \Delta y \Delta z)^{1/3}, \quad (2.17)$$

where the mixing length is dependent only on the model horizontal and vertical grid resolution and which represents the distance over which ensemble averaging occurs. Some formulations have been developed for very specific BL conditions. Deardorff (1980) suggested a mixing length formulation to account for small mixing length in stably stratified regions of the form

$$l = 0.76e^{1/2} \left( \frac{g}{\theta_0} \frac{\partial \theta}{\partial z} \right)^{-1/2}, \quad (2.18)$$

where  $e$  is the TKE. This formulation is also used within COAMPS<sup>TM</sup> for the same purpose. A variety of mixing length formulations have been used successfully to model the stable nocturnal boundary layer, because of the absence of large eddies (Estournel and

Guedalia 1987; Lacser and Arya 1986; Yu 1976; and Delage 1974). For example, the formulation from Delage (1974),

$$\frac{1}{l} = \frac{1}{\kappa z} + \frac{f}{0.0004G} + \frac{\beta}{\kappa L}, \quad (2.19)$$

where  $G$  is the geostrophic wind speed,  $f$  the Coriolis parameter,  $\beta$  a constant, and  $L$  the Obukov length scale, is an asymptotic formulation that allows for different atmospheric dependencies to be factored into the calculation (i.e., height, stability, wind, turbulence). Equation 2.19 is based on the formula developed by Blackadar (1962),

$$\frac{1}{l} = \frac{1}{\kappa z} + \frac{1}{l_0}, \quad (2.20)$$

where  $k$  is the Von Karman constant and  $z$  the height, and  $l_0$  is some maximum value of length scale prescribed for a mixed layer. Equation 2.20 is used for the mixing length formulation in many mesoscale and LES model parameterization schemes. The formulation asymptotically approaches two limits, where  $l \sim \kappa z$  as  $z$  approaches zero, and  $l \sim l_0$  as  $z$  approaches infinity. Equation 2.20 is widely used with  $l_0$  constant or derived using formulations of varying complexity. The MY82 formulation of vertical mixing length, used within the MY82 turbulence parameterization scheme used in COAMPS<sup>TM</sup>, follows Blackadar (1962), with

$$l_0 = \frac{\left( \int z e dz \right)}{\int e dz}, \quad (2.21)$$

which represents the ratio of first to zero order moments of vertical distribution of TKE. Physically, this means that the length scale in the upper portion of the boundary layer, which is related to the scale of turbulent eddies, is sensitive to the vertically integrated TKE. The added dependence on TKE creates a prognostic equation for mixing length in connection with the TKE equation, resulting in eddy coefficients that vary in time and space as the BL structure changes.

Using higher-order closure techniques allows the use of even more complex formulations for mixing length. Therry and Lacarrere (1983) attempt to improve the

mixing length formulation for turbulence modeling of the convective BL, based on results from a third-order closure scheme and experimental studies. They derive a rather detailed formulation of both a dissipation and turbulent mixing length scale, dependent on TKE flux and which also account for various thermal conditions and for the larger differences between vertical and horizontal eddy motions as the effects of buoyancy become larger. Bougeault and Andre (1986) develop a mixing length formulation for use in a third-order closure turbulence model, specific for the case of a stratocumulus-topped BL where a statically unstable region exists at the cloud top. Their formulation is based on a parcel displacement scheme, where the upward and downward paths of an imaginary parcel are calculated, based on the TKE at a given height in the BL and the buoyancy force the parcel experiences at that height. The mixing length is calculated as an average between the upward and downward paths, weighted towards the smaller path length.

In summary, it is evident by the large number of mixing length formulations proposed in the literature, that the choice of appropriate mixing length for turbulence closure based on gradient transfer or K-theory is not always obvious. The use of higher-order closure techniques come with the expense of added computational complexity, and so schemes such as the MY82 scheme (used within many of today's mesoscale models), which retains the simplicity of K-theory parameterization, but improves the model by making the mixing length a prognostic variable (based on TKE), are more desirable. The remaining chapters of this study focus on the adequacy of the MY82 mixing length formulation used within the COAMPS<sup>TM</sup> BL parameterization scheme in representing the turbulent structure of the convective BL.

THIS PAGE INTENTIONALLY LEFT BLANK

### **III. DETERMINING THE SCALE OF TURBULENCE FROM OBSERVATIONS**

#### **A. OBJECTIVE**

To better understand how the resolution of mesoscale models relates to the scales of turbulence within the BL, we performed spectral analysis of turbulence measurements from near the surface and within the convective mixed layer (ML) using high-rate aircraft measurements from three different experiments over the ocean. The objective is to generalize the different scales of turbulence and to directly evaluate the SGS representation of the turbulent fluxes and variances. The spectral analysis performed here will result in turbulent variances as a function of the length scale of spectral integration for different cases of convective BL's over the ocean.

Chapter II summarized previous studies on scales of BL turbulence, the results of which will be utilized here as a basis for generalizing the observed turbulent scales. Our focus here will be on cases with strong convective BL's, since it was shown in Chapter II that the convective BL contains the largest eddies which would most likely approach the scale of a high resolution model.

In this chapter, we analyze turbulent energy spectra and calculate length scales, using aircraft observations from the three field experiments described below, in an attempt to better understand the contribution to turbulent statistics from different scales of turbulence. This analysis will provide the justification for modifications to the COAMPS model to more correctly parameterize SGS turbulence in high resolution simulations where turbulence is partly resolved.

#### **B. ANALYSIS OF TURBULENCE SPECTRA FROM OBSERVATIONS**

##### **1. Aircraft Observations**

###### *a. Japan/East Sea (JES) Experiment*

The JES experiment took place in January and February 2000. The main objectives of the atmospheric portion of the JES experiment were to characterize the

lower atmosphere over the JES and examine the role played by the marine boundary layer in determining air-sea heat fluxes in the JES. This study utilizes the atmospheric measurements collected by the Twin Otter research aircraft operated by the Center for Interdisciplinary Remotely Piloted Aircraft Studies (CIRPAS). Measurements utilized, in this chapter and in later chapters, include SST, flight level wind ( $u$ ,  $v$ , and  $w$ ), temperature, and water vapor, as well as derived flight level potential temperature and moisture fluxes and wind stress. The Twin Otter aircraft speed was  $70 \text{ ms}^{-1}$  and measurement flight patterns were made up of low-level transects and soundings to map the surface flux and mean horizontal and vertical structure of the boundary layer. Data was collected at a sampling rate of 10 Hz. A more detailed description of the JES experiment measurements is given in Kheif et al. (2003). While the JES experiment covered a wide range of wintertime synoptic conditions, this study will focus on the high wind cases of frontal and post-frontal large scale forcing in cold air outbreak conditions.

The JES experiment Twin Otter measurements from level flight legs flown near the surface are used in this chapter for the spectral analysis of BL turbulent structure. In later chapters, the level leg observations as well as slant ascent/decent soundings from JES are used for inter-comparison with high-resolution COAMPS output fields. A brief summary of the Twin Otter flight legs used in this study is provided in Table 3.1.

***b. Tropical Ocean Global Atmosphere Coupled Ocean-Atmosphere Response Experiment (TOGA COARE)***

The TOGA COARE intensive operating period (IOP) took place between 1 November 1992 and 28 February 1993. TOGA COARE was a large international field experiment conducted to study the atmospheric and oceanic exchange processes over the region of the western Pacific known as the "warm pool". This region, which is near the equator between about  $140^\circ \text{ E}$  and  $170^\circ \text{ E}$ , is a region of very warm ocean temperatures ( $\sim 28^\circ \text{ C}$ ) with active convection and significant precipitation linked to the El Nino climate variation. TOGA COARE's primary objective was to achieve significantly more accurate and complete descriptions of the surface meteorology and air-sea fluxes, with the ultimate goal of producing a dataset that will be used to improve air-sea interaction and BL parameterizations in numerical models and to validate coupled models. Weller

| <b>Date</b> | <b>Flight Leg</b> | <b>Measurement Start/ End Time (UTC)</b> | <b>Leg Position (lat (degrees N) lon (degrees E)) / Length (km)</b> | <b>Mean Altitude (m)</b> |
|-------------|-------------------|--|---|--------------------------|
| 02/01/00    | R01               | 0039-0110                                | 41.0 133.2 – 132.0 / 90   | 41                       |
| 02/01/00    | R03               | 0124-0144                                | 41.3 132.0 – 133.0 / 70   | 40                       |
| 02/01/00    | R04               | 0200-0217                                | 41.7 132.7 – 132.1 / 45   | 43                       |
| 02/01/00    | R08               | 0326-0351                                | 41.0 132.1– 133.2 / 94  | 39                       |
| 02/17/00    | R02               | 0052-0116                                | 41.0 133.0– 132.1 / 71  | 46                       |
| 02/17/00    | R04               | 0129-0146                                | 41.3 132.1– 132.9 / 61  | 42                       |
| 02/17/00    | R06               | 0200-0222                                | 41.7 132.9– 132.1 / 61  | 44                       |

| <b>Date</b> | <b>Sounding</b> | <b>Start/ End Time (UTC)</b> | <b>Mean Position (lat (degrees N) lon (degrees E))</b> | <b>Sounding Depth Coverage (m)</b> |
|-------------|-----------------|------------------------------|--|------------------------------------|
| 02/01/00    | S2              | 0144-0150                    | 41.4 133.0   | 36 – 803                           |
| 02/01/00    | S3              | 0150-0157                    | 41.5 132.8   | 803 – 27                           |
| 02/17/00    | S1              | 0147-0153                    | 41.4 132.9   | 40 – 813                           |
| 02/17/00    | S2              | 0155-0159                    | 41.6 132.9   | 808 – 40                           |
| 02/17/00    | S7              | 0409-0414                    | 41.1 132.9   | 41 – 878                           |
| 02/17/00    | S8              | 0414-0420                    | 41.2 132.8   | 917 – 60                           |
| 02/17/00    | S9              | 0420-0426                    | 41.3 132.7   | 58 – 782                           |
| 02/17/00    | S10             | 0426-0432                    | 41.4 132.6   | 784 – 64                           |
| 02/17/00    | S11             | 0432-0436                    | 41.5 132.5   | 63 – 806                           |
| 02/17/00    | S12             | 0436-0441                    | 41.6 132.4   | 805 – 90                           |
| 02/17/00    | S13             | 0441-0447                    | 41.7 132.3   | 88 – 775                           |
| 02/17/00    | S14             | 0447-0453                    | 41.8 132.2   | 779 – 35                           |

**Table 3.1.** JES low level flight legs and sounding legs analyzed in this study.

and Anderson (1996), describe the wind conditions during the IOP as dominated by periods of low wind (mean wind speed  $\sim 2 \text{ ms}^{-1}$ ), with some short-lived events and westerly wind burst events where the wind speed reached  $\sim 9\text{-}12 \text{ ms}^{-1}$  for a short duration. These wind bursts excite the local air-sea heat and moisture fluxes, enhancing the convection and BL turbulence even more.

Measurements from TOGA COARE utilized in this study include horizontal and vertical wind velocity, temperature, and moisture fields collected by the National Center for Atmospheric Research (NCAR) Electra aircraft, which flew 32 flights to study boundary layer fluxes and convective systems. The Electra aircraft made turbulence, radiation, and cloud microphysics measurements in the BL. The measurements used in this study consisted of horizontal legs at different altitudes in and above the marine BL, and vertical soundings throughout the BL. The aircraft recorded measurements at a constant speed of  $100 \text{ m s}^{-1}$ . Horizontal flight legs consisted of 20-minute L-shaped legs at various vertical levels within and above the BL. Observations captured cloud structure and measured the turbulent flux profiles at various levels in the BL. Weller and Anderson (1996) describes the Electra atmospheric data collection instrumentation used in TOGA COARE. The data was sampled at a 50 Hz sampling rate and recorded at 20 Hz for data processing. These measurements were obtained from the data archives at the National Center for Atmospheric Research (NCAR). Descriptions of the synoptic and BL meteorological conditions of the TOGA COARE flights analyzed are based on information from the TOGA COARE IOP Operations Summary (1993). These descriptions will be used to explain the characteristics of the BL turbulence structure along these flight tracks. Table 3.2 lists the flight date, time, average BL depth (as determined from sounding measurements), and average level leg length and wind speed for the boundary layer flight measurement legs that were used in this study. In cases where convective clouds were present, the lifting condensation level (LCL) was calculated from sounding measurements and taken as the BL height (Stull 1988).

| <b>Flt #</b> | <b>Date</b> | <b>Measurement Start/ End Time (UTC)</b> | <b>Avg BL Depth or LCL (m)</b> | <b>Average BL level leg length (km)</b> | <b>Avg. BL wind speed (m/s)</b> |
|--------------|-------------|--|--------------------------------|---|---------------------------------|
| 10           | 12/9/92     | 2230-0300                                | 300                            | 119                                     | 2.5                             |
| 12           | 12/10/92    | 1830-2200                                | 450                            | 52                                      | 3.0                             |
| 19           | 1/13-14/93  | 2230-0200                                | 450                            | 59                                      | 2.0                             |
| 20           | 1/14-15/93  | 2230-0200                                | 500                            | 60                                      | 1.9                             |
| 22           | 1/17-18/93  | 0030-0330                                | 400                            | 119                                     | 4.9                             |
| 23           | 1/19/93     | 0045-0330                                | 910                            | 122                                     | 7.4                             |
| 24           | 1/26-27/93  | 2230-0050                                | 250                            | 49                                      | 4.8                             |
| 26           | 1/28-29/93  | 2245-0200                                | 570                            | 61                                      | 6.5                             |

**Table 3.2.** TOGA COARE level flight legs analyzed in this study.

### *c. FIRE Experiment*

During June and July 1987, the First International Satellite Cloud and Climate Project (ISCCP) Regional Experiment (FIRE) Marine Stratocumulus Intensive Field Observations (IFO) was conducted off the coast of southern California. FIRE obtained a comprehensive set of boundary layer and above boundary layer measurements in 12 coordinated multi-missions. Albrecht et al. (1988) and Cox et al. (1987) give a detailed description of project objectives. In addition, Kloesel et al. (1988) gives a summary of experiment operations and general meteorological conditions during the period. In this chapter, we utilize horizontal turbulence leg data obtained by the NCAR Electra aircraft (as described above for the TOGA COARE experiment) during FIRE on July 3, 1987 (flight 3), at various levels in the boundary layer.

#### **2. Statistical Calculations for Spectral Estimates**

In this study, we used MATLAB, the data acquisition, analysis, and visualization software application commonly used in the scientific community, as an integral tool for the detailed analysis of both model output and the real data. For the graphical representation of the spectra analysis, the MATLAB function PSD was used to estimate the power spectral density of a discrete time series using Welch's averaging method. The time series is linearly detrended, which reduces the contamination of the spectra by wavelengths longer than the data series. The power spectral density as a function of wave number is then estimated to a 95% confidence interval. The spectra are calculated between the smallest resolvable scale (or largest resolvable (Nyquist) frequency), defined by the data frequency (for observations), and the largest resolvable scale, defined by the length of the observation leg.

Using the energy density spectrum, we also calculate the Ogives, defined as the cumulative integral of the spectrum from the smallest wavelength, (where the contribution to the energy is generally small) to some specified wavelength of spectral integration ( $\lambda_0$ ) (Rogers et al. 1995). Theoretically, Ogives can be expressed as

$$O(\lambda_0) = \frac{\int_0^{\lambda_0} S(\lambda) d\lambda}{\int_0^{\infty} S(\lambda) d\lambda}, \quad (3.1)$$

where the denominator is the total integrated energy over all wavelengths, or variance, which normalizes the calculation. In discrete form, we set the lower limit in integrations to the wavelength corresponding to the Nyquist frequency (smallest resolvable wavelength) for both integrals in Equation 3.1, and the upper limit to 3 km (generalized estimate of the largest turbulent eddy size for the cases analyzed here), in the variance calculation in order to only consider spectral energy associated with turbulence. The resulting plot of the Ogives versus  $\lambda_0$  allows us to analyze the fraction of total turbulent energy from scales smaller than a given scale limit.

### 3. Spectral Analysis

#### a. *Method and Objectives*

Here we present examples of the energy density spectrum of vertical velocity as a function of wave number, and the Ogives vs. wavelength of spectral integration. In these examples, wavelength ( $\lambda$ ) and wave number ( $k$ ) are related by

$$\lambda = 2\pi/k, \quad (3.2)$$

where  $k$  is calculated from the sampling frequency and the aircraft speed. For reference, a wave number of  $1 \text{ km}^{-1}$  corresponds to a wavelength of about 6 km.

The spectra are presented in log-linear fashion, so that the area under the energy curve is proportional to the variance, and a peak in the spectrum can be interpreted as the wavelength that contributes most to the variance. As the scale increases, the statistical significance and thus the smoothness of the spectral estimate decreases. However, the length of all observation legs in these examples, which varies from 70 to 130 km, is considered adequate for the spectral representation of the entire turbulence scale, which is considered here to be at wave numbers  $2 \text{ km}^{-1}$  and higher (turbulent eddies 3 km and smaller). For better presentation of the turbulent energy

spectra, the signal from scales larger than 6 km was filtered out of the observed vertical velocity, to remove signals from the less statistically significant waves.

The spectra analysis will focus primarily on two aspects: 1) determination of the peak wavelength, which will indicate the size of turbulent eddies dominating the fluctuations of turbulent variables within the BL, and 2) the Ogives, or fraction of total turbulent energy from scales smaller than a given scale limit. Ogives allows us to determine the fraction of total turbulent energy that could potentially be resolved by a high-resolution mesoscale model, and thus the appropriateness of an ensemble turbulence parameterization.

While TKE depends on the variance of both horizontal and vertical wind, we choose to present only the spectra of vertical velocity. The horizontal wind spectra were analyzed as well, and the shape and turbulent scales are quite similar to that of the vertical velocity spectra. The main difference is the significant mesoscale contribution to the spectral energies in the horizontal wind spectra, which are not present in the vertical velocity spectra. While vertical motion is limited by the depth of the BL, there are no boundaries on the horizontal flow to restrict the scales of motion. These mesoscale contributions to the horizontal wind spectra are also noted in Nucciarone and Young (1991) for the FIRE experiment.

#### ***b. Surface Layer Spectra***

Figures 3.1 through 3.3 show three examples of turbulent characteristics of the surface layer of the convective BL using near-surface high-rate vertical velocity measured by aircraft. The surface layer is defined as a height ( $z$ ) within the BL that is less than or equal to 1/10 of the BL height ( $z_i$ ). Using a normalized height scale  $z^*$  equal to  $z/z_i$ , the surface layer is then defined for a  $z^*$  of 0.1 or less. Figure 3.1 is

### JES Aircraft Observations – Mean Spectra

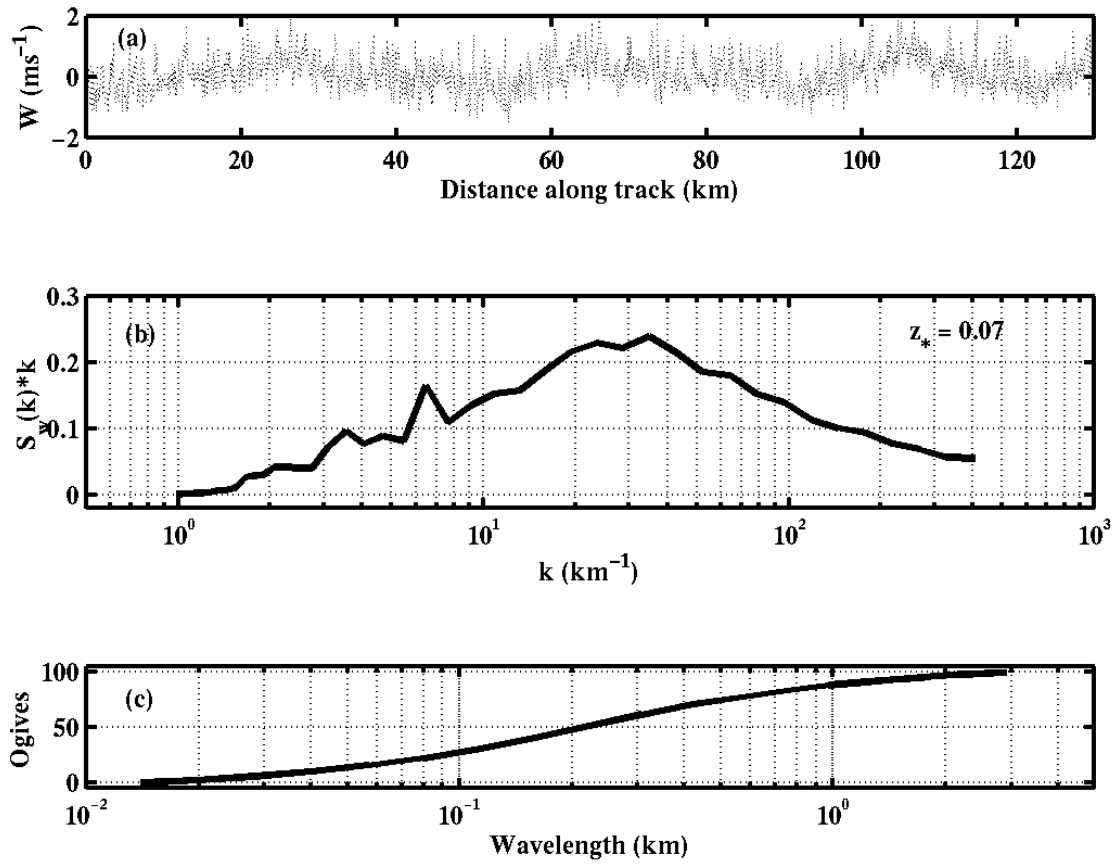


**Figure 3.1.** Vertical Velocity ( $w$ ) along the flight leg (a), energy density spectrum of  $w$  vs. wave number (b) and Ogives of  $w$  (c) vs. wavelength, using near-surface observations from the JES experiment.

TOGA COARE Aircraft Observations – Leg F1 23b

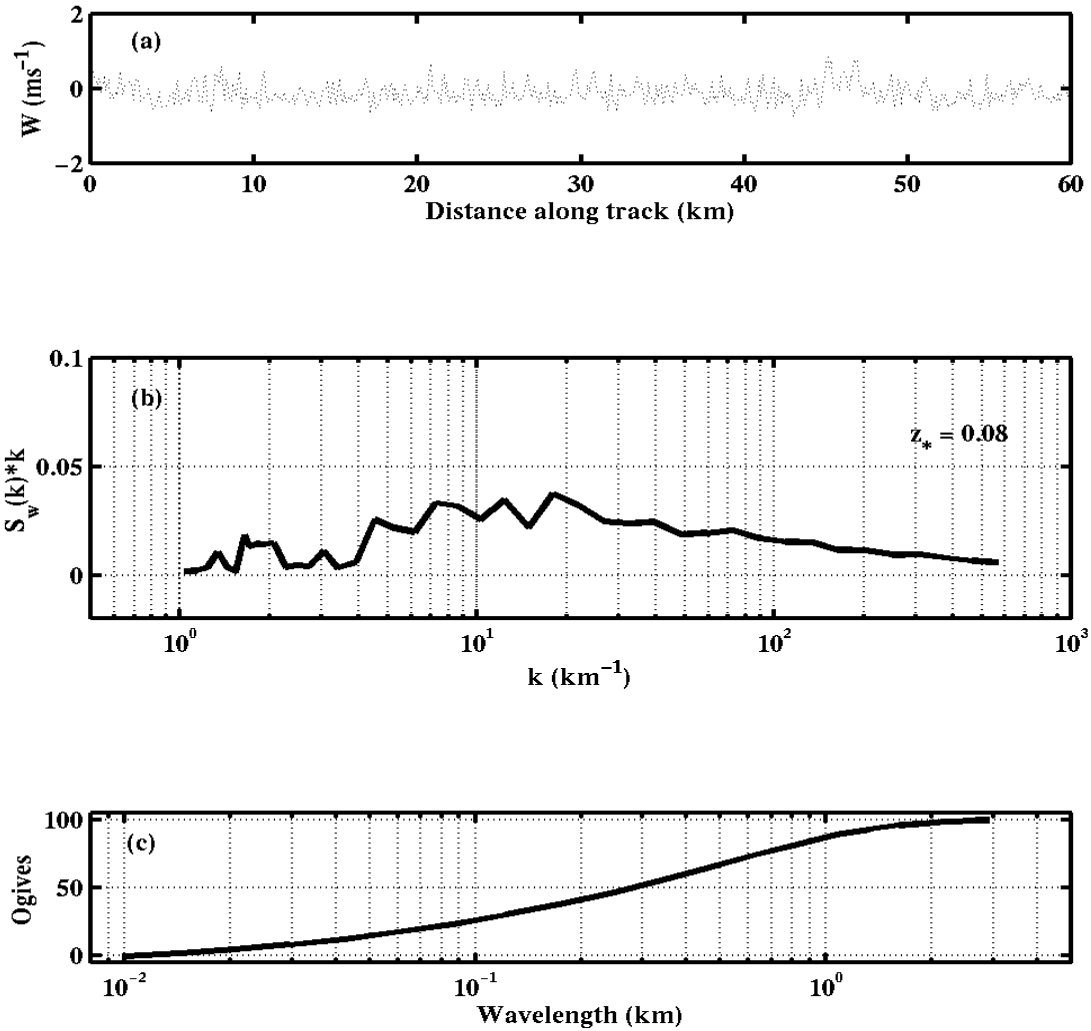


**Figure 3.2.** Same as Figure 3.1, except using observations from a near-surface flight leg during flight 23 of the TOGA COARE experiment.

FIRE Aircraft Observations – Leg H1 3a

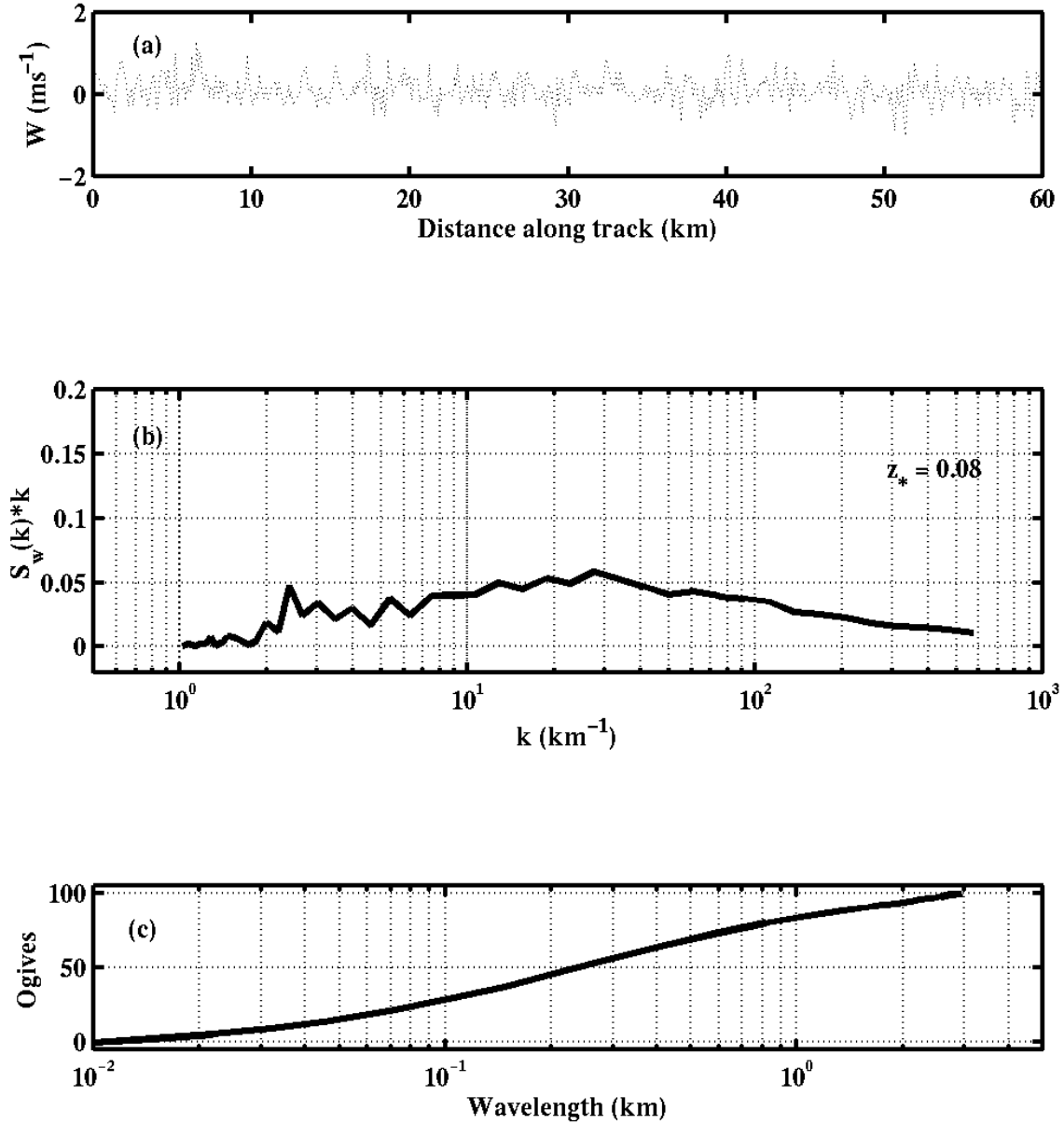


**Figure 3.3.** Same as Figure 3.1, except using aircraft observations from a near-surface flight leg during flight 3 of the FIRE experiment.

an example from the JES experiment, on January 31, 2000. The surface layer was unstable ( $z/L = -0.35$ ), with an air-sea temperature difference of nearly 10 degrees. The horizontal wind speed was, on average, greater than  $12 \text{ ms}^{-1}$ . For this flight, the BL depth averaged around 700 m as determined from sounding profiles. The spectrum and Ogives in Figure 3.1 are averages of four different low-level legs from this flight, flown at 40 m above the sea surface ( $z^* = 0.07$ ). Figure 3.2 shows an example from flight 23 of the TOGA COARE experiment. For this flight, the surface layer was also unstable ( $z/L = -0.86$ ), with an air-sea temperature difference of 3 degrees and a mean BL horizontal wind speed of about  $8 \text{ ms}^{-1}$ . The BL height (taken as the lifting condensation level) averaged around 400 m. The observations used are from a 110 km long flight leg flown at 31 m ( $z^* = 0.08$ ) above the sea surface. Figure 3.3 shows a typical vertical velocity spectra and Ogives from flight 3 of the FIRE experiment. During this night mission, the surface layer was unstable ( $z/L = -0.38$ ) with an air-sea temperature difference of 0.8 degrees, and an average BL horizontal wind that exceeded  $10 \text{ ms}^{-1}$ . The BL was very well mixed and turbulent, with an average depth of about 750 m. The observations used are from a 120 km long flight leg flown at 56 m above the sea surface ( $z^* = 0.08$ ).

We can see distinct features of the near-surface turbulence for the observations in these three cases of unstable surface layers. Comparing the top panels in each of the Figures 3.1 through 3.3, the JES example clearly has the largest vertical velocity variation. This fact is also evident in the larger magnitude of the spectra compared to the TOGA COARE and FIRE examples. For all three examples, the spectral signature of turbulent energy appears clearly at wave numbers (wavelengths) to the right of about  $2 \text{ km}^{-1}$  (3 km) on the x-axis, and the peak scale of turbulence eddies ( $\lambda_m$ ) generally exists within the wavelength range of 200 to 300 m, representing the dominant eddy size contributing to the total TKE at the measurement level near the surface. The inconsistency in the shape of the spectra at larger scales between the three cases with varying values of  $z/L$  is consistent with the findings of Kaimal et al. (1972) for vertical velocity spectra in the unstable surface layer. When plotted on a log-log scale (not shown here), the inertial sub-range in the near-surface energy spectra (as well as the spectra

from higher levels in the ML, shown later) follow the  $-5/3$  law of the inertial sub-range, and the scale of the inertial sub-range (which appears to begin around  $60 \text{ km}^{-1}$  (100 m wavelength) in all three cases), does not vary among the different cases (Kaimal et al. 1972). In the JES case, we observe the existence of a double-peak in spectral intensities, as was observed in Grossman (1982) (see chapter II). The peak near 1 km, while not dominant near the surface, signifies the existence of observed horizontal roll vortices (discussed chapter IV) produced in a post-frontal cold air outbreak over the relatively warmer ocean. The much larger magnitude spectra in the JES ML case, compared to the examples from TOGA COARE and FIRE, is due to the relatively more intense turbulence forced by large surface fluxes associated with the unstable surface layer.

The Ogives plots in Figures 3.1 through 3.3 indicate that, near the surface, 50% of the total turbulent variance is contained in eddies smaller than about 200 m in scale. The largest eddies, greater than 1 km in scale, make up about 10% of the turbulence variance near the surface. This implies that a mesoscale model operating at a horizontal resolution of 500 m could theoretically resolve a 1 km ( $2\Delta x$ ) wave, and thus 10% of the turbulent energy near the surface.

### *c. Mixed Layer Spectra*

Vertical velocity measurements from the TOGA COARE and FIRE experiments taken from within the ML of the convective BL are also analyzed to determine the scale of turbulence at these levels. The vertical velocity along the leg, spectra, and Ogives plots in Figure 3.4 are from flight 23 of the TOGA COARE experiment. The observations used are from a flight leg flown at 221 m above the sea surface, in the middle of the ML ( $z^* = 0.55$ ). Figure 3.5 illustrates these same parameters for flight 3 of the FIRE experiment, from a leg flown at 481 m above the sea surface, also near the middle of the ML ( $z^* = 0.64$ ).

Compared to the near the surface, we observe distinct and consistent differences in the ML turbulence scales, fairly consistent with the findings of Grossman (1982) for over the ocean MLs. For comparison purposes, the near-surface and ML spectra are plotted on the same axis in Figures 3.6 (for FIRE) and 3.7 (for TOGA

TOGA COARE Aircraft Observations – Leg H3 3a

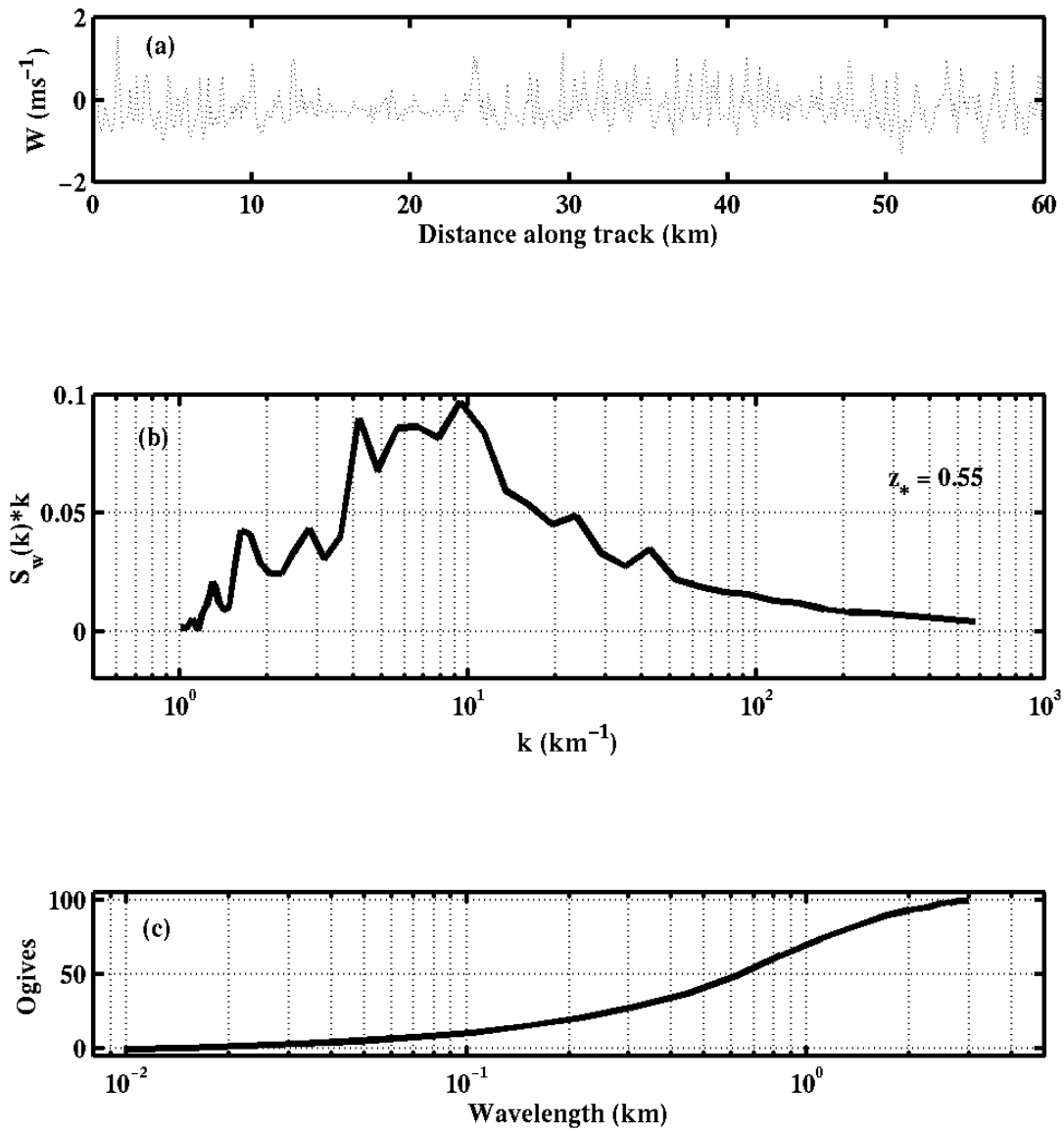


**Figure 3.4.** Same as Figure 3.2 except using aircraft measurements from a flight leg flown at 221 m above the sea surface.

FIRE Aircraft Observations – Leg H2 3b

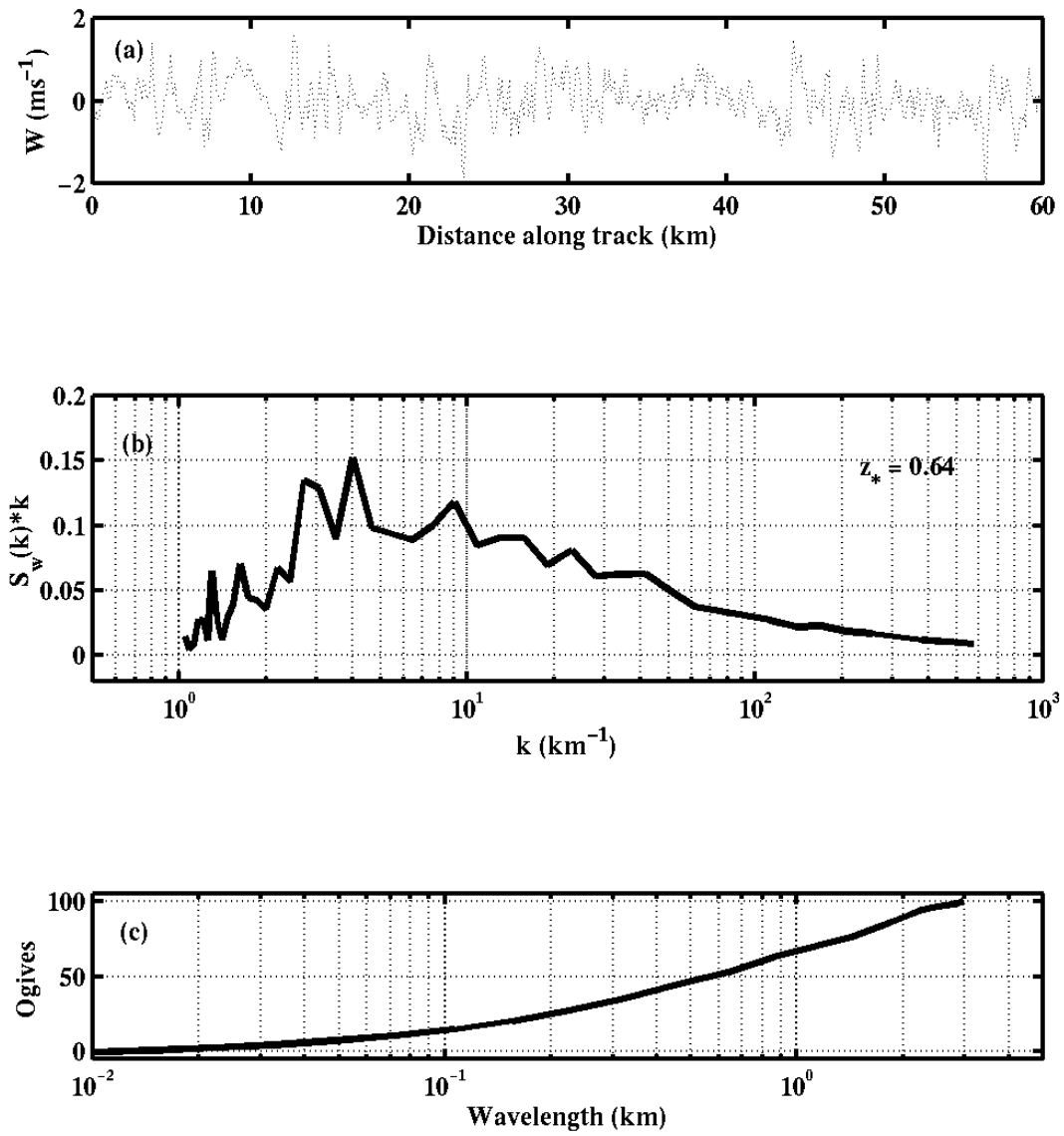


**Figure 3.5.** Same as Figure 3.3, except using aircraft measurements from a flight leg flown at 481 m above the sea surface.

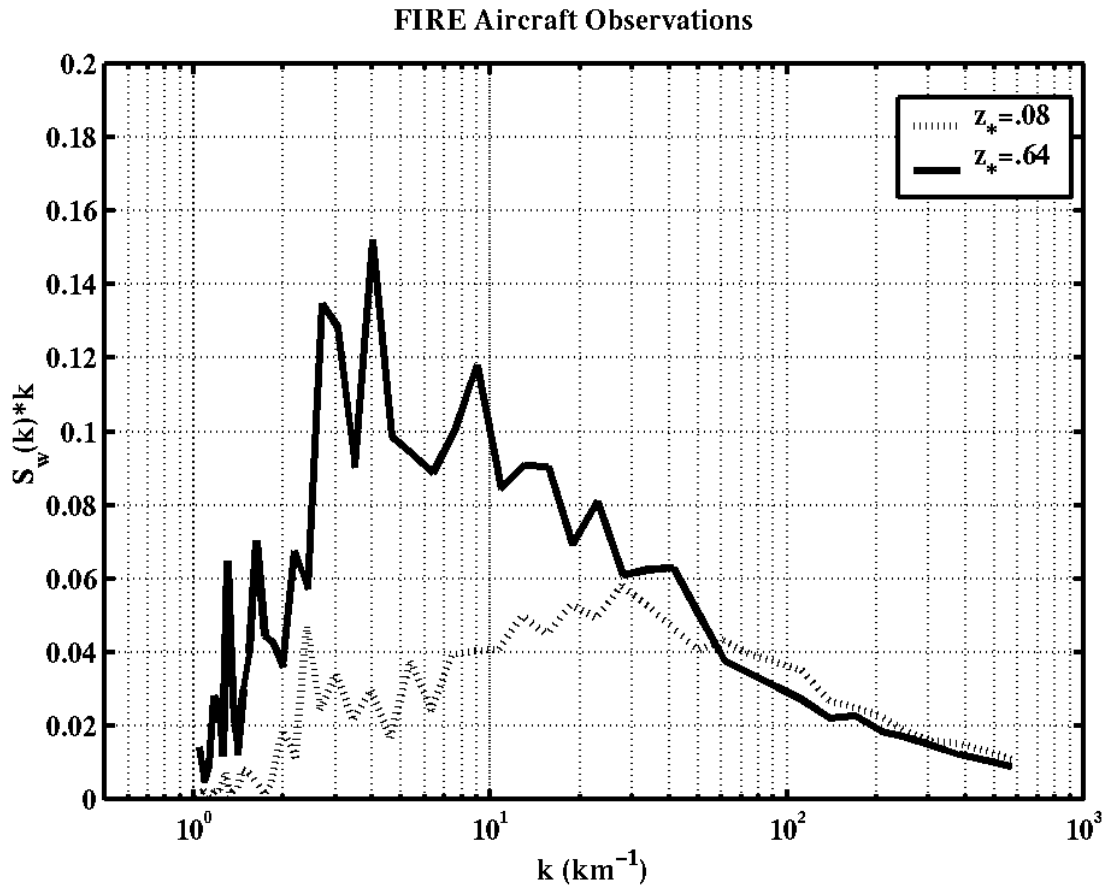


**Figure 3.6.** Vertical velocity spectra from FIRE aircraft observations, from figures 3.3 and 3.5, plotted together for comparison.

TOGA COARE Aircraft Observations

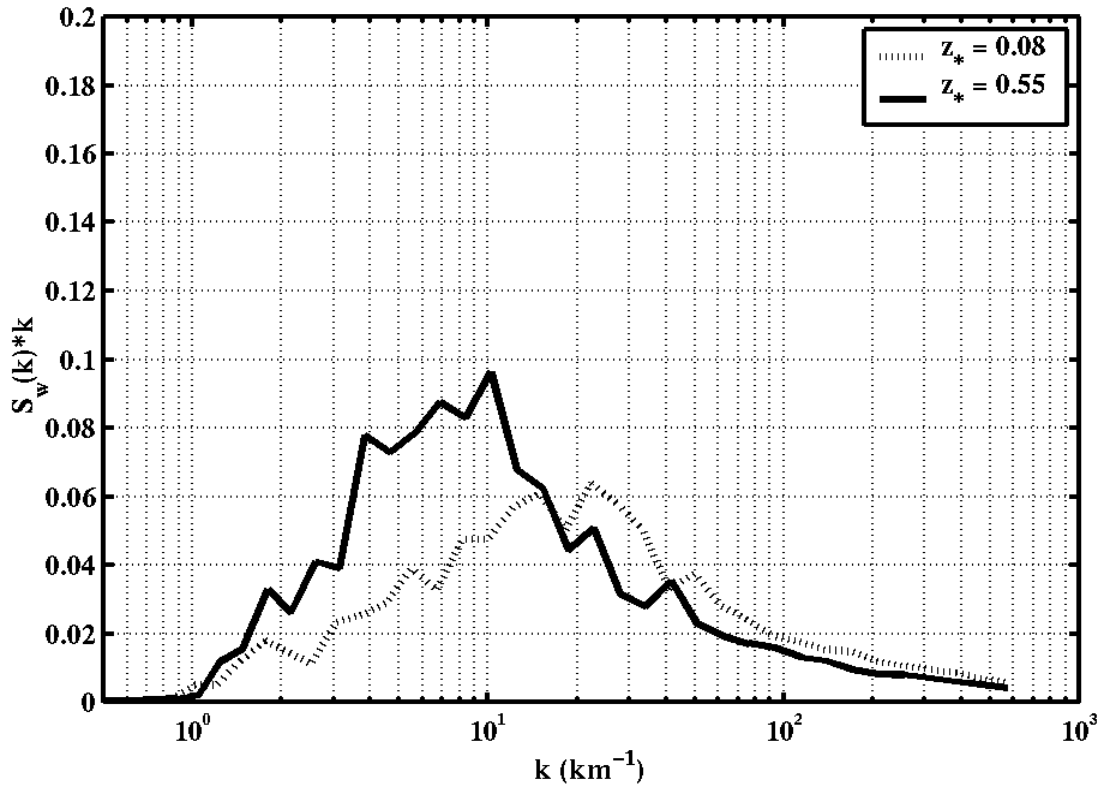


Figure 3.7. Same as Figure 3.6, except for figures 3.2 and 3.4 from TOGA COARE.

COARE). In general, the magnitude of the spectral peak at the km scale is much larger than near the surface, and the eddies at the km scale are now dominant. The  $\lambda_m$  has not changed significantly in magnitude nor has it shifted much compared to the near-surface spectra. The energy drop at 6 km (i.e., the filter scale) is now more abrupt than it was near the surface, since there is now a significant amount of energy at larger end of the turbulent scale near the spectral gap. These differences between the surface and ML spectra are consistent in both the FIRE and TOGA COARE spectra. We also observed complexity in the large scales of the individual spectra, where there are several peaks with significant energy, and no single dominant  $\lambda_m$ . These variations are expected since the calculations are from only one flight leg.

For the TOGA COARE case,  $\lambda_m$  has increased from about 400 m near the surface, to between 600 m and 1.5 km in the ML, and the spectral magnitude near the 1 km scale has nearly doubled (evident from the larger variation of the vertical velocity along the flight leg (top panel in the figures), compared to near the surface. With a BL height of 400 m, the energetic large-scale eddies have a size of about  $1.5 z_i$ , consistent with the findings from Kaimal (1976). More dramatic differences are seen between the surface and ML spectra from FIRE. Due to the more energetic large scale eddies, the ML spectrum is nearly four times larger in magnitude in the larger scales, near 1 km, compared to near the surface. The more drastic increase in magnitude between the near-surface and ML spectra compared to that of the TOGA COARE example is most likely due to the higher BL and more turbulent ML of the FIRE case (see Wang and Albrecht 1994). Unfortunately, no ML flight legs were flown during the JES experiment to include in this comparison. The empirical relationship in Kaimal (1976) appears to be valid since it is supported by the examples shown here from FIRE and TOGA COARE.

Consistent with the shift in turbulent energy to larger scales, the Ogives calculations for the ML examples (lower panel, Figures 3.4 and 3.5) show a shift in the fraction of turbulent energy at a given scale. We see that the ML Ogives indicate only about 15 to 20% of the total turbulence variance at wavelengths below 600 m, over 30% of the total turbulent eddy energy scales above 1 km. A mesoscale model operating at

500 m resolution could theoretically resolve four times more turbulent energy in the ML (30%), compared to near the surface (10%), implying that the resolvability issue is even more important within the ML.

#### *d. Conclusions*

The purpose of the spectral analysis was to determine the scales at which turbulence in the atmospheric BL occurs, and to determine the extent to which a high-resolution mesoscale model using ensemble parameterization accounts for that turbulence. The vertical velocity spectra from over-the-ocean convective BLs near the surface and within the ML were analyzed. No overland cases were shown here, but past studies by Kaimal (1976) and Young (1987) show that the vertical velocity spectra over land are similar in terms of shape and height dependence to the spectra over-the-ocean, but have a somewhat larger peak wavelength. While it is difficult to make general conclusions from a limited number of cases, our results were consistent and in agreement with previous studies. In addition, we discovered that while the majority of turbulence in the convective ML indeed occurs at scales near 1 km, a significant fraction of the total turbulence can extend to larger scales near the spectral gap, blurring the convenient separation between the mesoscale and turbulent scales.

The Ogives plots suggest that nearly 30% of the turbulent eddy energy in the ML exists at scales above 1 km. This suggests that as the resolution of a mesoscale model approaches the sub-kilometer scales, the model would partially resolve a significant portion of the total BL turbulent energy. Theoretically, an ensemble turbulence parameterization represents the turbulence from all scales, so if indeed the larger scale turbulence is theoretically resolved by a high resolution mesoscale model, the SGS parameterization should only account for part of the total turbulence variance. The spectral analysis performed here thus provides an indication of the amount of turbulent energy we can expect a high-resolution mesoscale model BL ensemble turbulence parameterization to account for at different levels within the convective BL. The results suggest that it is no longer appropriate to use ensemble turbulence closure in a mesoscale model when the grid resolution goes below 1 km.

## C. TURBULENCE INTEGRAL LENGTH SCALES FROM OBSERVATIONS

### 1. Importance of Integral Length Scale Analysis

To further understand the scale of BL turbulence, the same aircraft observations used in the spectral analysis are used here to obtain the integral length scale (defined in chapter II). The purpose here is to quantify the length scale and its variation with height in the BL. This analysis will allow us to determine the appropriateness of the mixing length used in ensemble turbulence parameterizations when horizontal resolution is smaller than the scale of the largest turbulent eddies in the BL, and will be the basis for adjustments made to the ensemble turbulence parameterization within COAMPS, via the mixing length calculation, to account for the partial resolution of the turbulent eddies.

### 2. Integral Length Scale Calculation

#### a. Formulation

For each horizontal flight leg used in the subsequent analysis, the integral length scale of vertical velocity is calculated for FIRE flight 3 and the TOGA COARE flights using Equation 2.2. The autocorrelation coefficient ( $\rho(t)$ ) is calculated by finding the covariance of the vertical velocity and the time lag at each point along the flight leg (the co-variance is normalized so that the co-variances at zero lag are identically 1.0).  $\rho(t)$  is the time lag corresponding to the point along the leg where the normalized covariance first falls below  $e^{-1}$ .  $U$  is the aircraft speed relative to the wind speed in the direction of the flight path.

#### b. Calculation of Partial Integral Length Scales

Using a 3<sup>rd</sup> order Butterworth filter in MATLAB, a high pass filter was designed to remove low frequency perturbations above a specified filter scale  $L$ . Figure 3.8 shows an example of the application of the filter function, where the energy from eddies larger than 500 m in scale is filtered out. Note that the filtering can be observed in the time series of the filtered vertical velocity, where the low frequency oscillations due to the larger eddies, seen in the unfiltered time series, are not present.

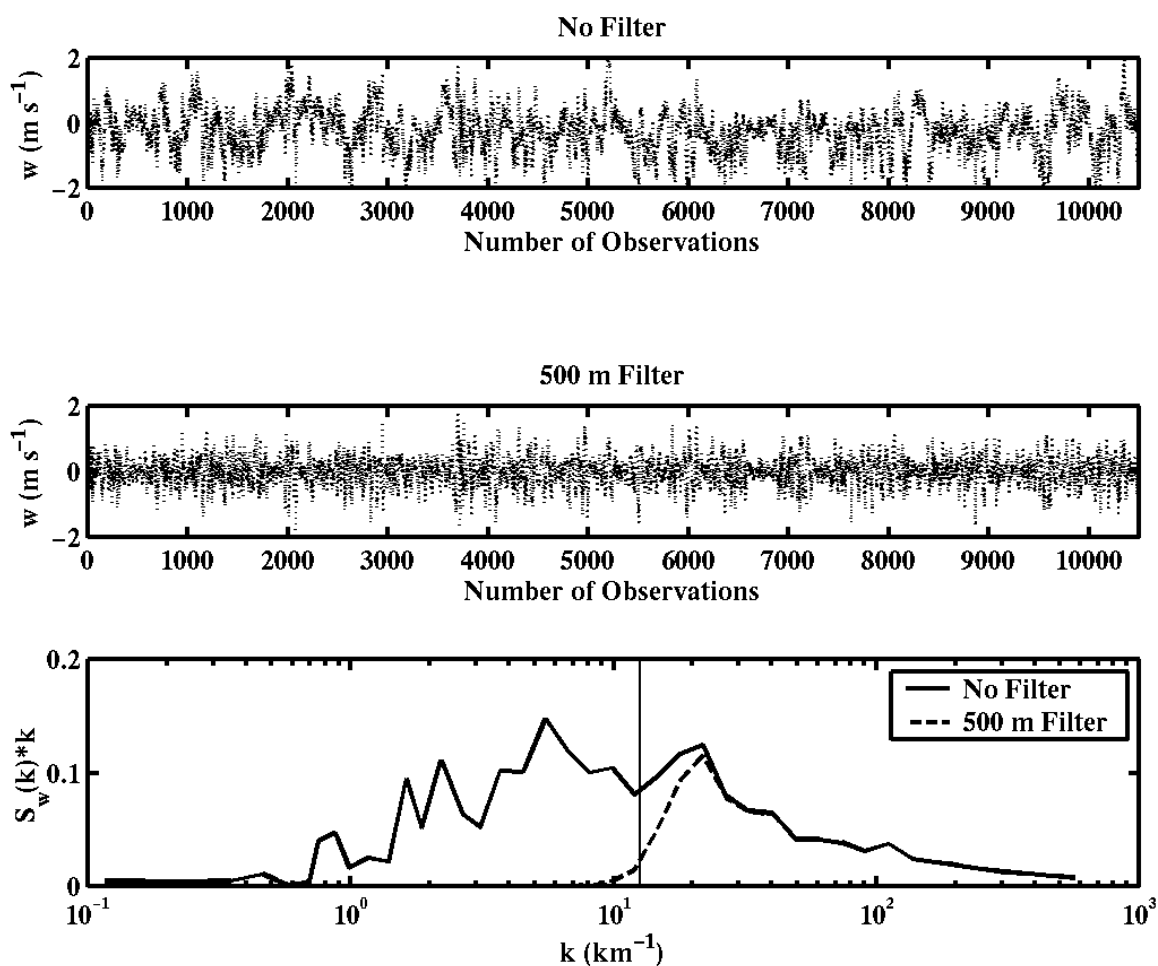


**Figure 3.8.** Example of time series and spectra of vertical velocity after filtering out energy from eddies scaling larger than 500 m. Observations are taken from a horizontal flight leg during FIRE Flight 3.

The filter is applied to the FIRE flight 3 and TOGA COARE data for the calculation of  $\rho(t)$ . The result is the calculation of partial integral length scale, defined as the integral scale of turbulence below a certain filter scale  $L$ . The ensemble integral scale representing all scales of turbulence was calculated by filtering out the signal from waves larger than 3 km in the vertical velocity time series, ensuring that the energy from all turbulent eddies are considered in the calculation. As implied by our results in the spectral analysis section, a 3 km filter would capture the energy from all scales of turbulence for the FIRE and TOGA COARE flight data, and is likely appropriate for most convective BLs.

This filter procedure was used to calculate the integral length scale for a range of  $L$  from 3 km down to 200 m. The partial integral scales from along and cross wind legs (flown in succession at the same level) were averaged together, based on Lenschow and Stankov (1986), where it was determined that there is only a slight difference between integral scales of the wind components calculated from along and cross wind flight legs.

### 3. Results

Following Lenschow and Stankov (1986), we plot the partial integral length scale, normalized by the BL height, for the different filter scales (Figure 3.9). The different symbols in Figure 3.9 represent the partial integral length scale for different  $L$ , as calculated from the observations. Using the normalized height scale  $z_*$ , we find that for both the FIRE and TOGA COARE observations, the ensemble integral length scale (i.e., at the 3 km filter scale) for vertical velocity ( $\Lambda_{ENS}$ ) is well represented at most  $z_*$  in the BL by

$$\Lambda_{ENS} / z_i = 0.43z_*^{1/2} . \quad (3.2)$$

This relationship also followed for the integral length scale for vertical velocity of Lenschow and Stankov (1986), using aircraft measurements taken in convective BLs over both ocean and land surfaces. The relationship does not fit the observations as well near the top of the BL, where the integral scale depends more on the stability of the overlying

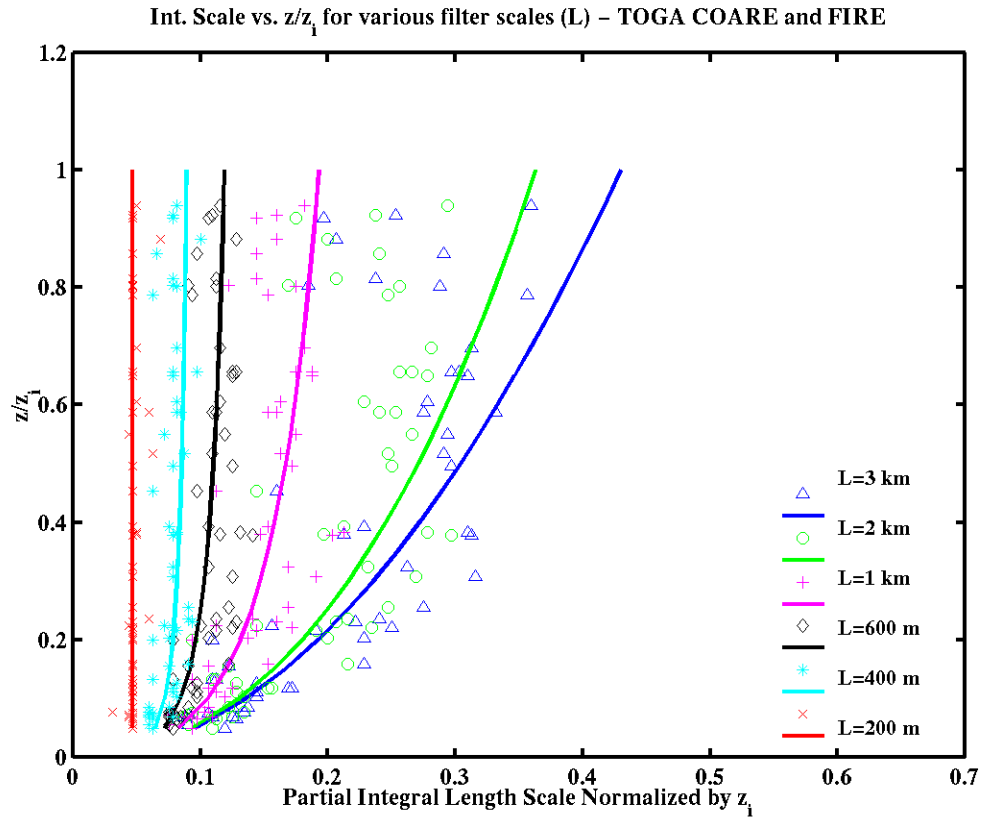


**Figure 3.9.** Integral length scale, normalized by the BL height ( $z_i$ ), for different filter scales (upper limit on the scale of motion) ( $L$ ). Calculations used observations from several horizontal flight legs at various levels in the BL from FIRE flight 3 and TOGA COARE. Different symbols represent the partial integral scale calculated along the flight leg for different  $L$ , as shown in the legend. The line that fits to the observations for  $L = 3$  km is calculated from Equation 3.2. The line that best fits the observations for  $L = 200$  m is a vertical line. Lines that fit to the observations for  $L$  between 200 m and 3 km are calculated from Equation 3.3.

layer and less on the scale of turbulent BL eddies (Carruthers and Hunt 1986).

As  $L$  decreases, such that only smaller and smaller scales of motion are considered in the calculation, the integral length scale expectedly decreases at all levels in the BL, as shown in Figure 3.9. The difference between integral scales for different  $L$  is largest in the middle and upper BL, where the majority of turbulent eddies are large, and smallest near the surface, where the size of most eddies is small. As  $L$  decreases, the integral length scale also becomes less variant with height in the BL, and we see that for  $L = 200$  m, representing eddies within the inertial sub-range, there is practically no variation in the integral scale with height.

Attempts were made to represent the partial integral length scale using the ensemble length scale ( $\Lambda_{ENS}$ ) and that from the 200 m cutoff filter ( $\Lambda_{200m}$ ). The latter is considered to represent the SGS length scale for a LES simulation, although the cutoff limit for LES is generally smaller than 200 m. Equation 3.3 is selected among many other alternatives for several reasons. First, this relationship should be applicable for the ensemble parameterizations currently used in COAMPS. Second, it should generate a length scale that approaches what is normally used in LES as the cutoff length falls into the range of the inertial sub-range. The above requirements ensure the asymptotic property of the length scale representation at large and small  $L$ . Third, it should fit the observed partial integral length scale shown in Figure 3.9 for intermediate  $L$ , where  $L$  relates to a horizontal grid resolution with  $L = 2 \Delta x$ . Therefore, in a high-resolution mesoscale model, the partial integral length scale using Equation (3.3) is essentially a weighted average between the ensemble and the LES length scales, where the weighting varies with  $\Delta x$ :

$$\frac{1}{\Lambda_{\Delta x}} = \frac{1 - e^{-R\Delta x}}{\Lambda_{ENS}} + \frac{e^{-R\Delta x}}{\Lambda_{200m}}. \quad (3.3)$$

The parameter  $R$  in Equation (3.3) should be obtained empirically. For the FIRE and TOGA COARE convective BL observations,  $R$  is determined to be  $3.8 \text{ km}^{-1}$ . At  $\Delta x = 500$  m,  $1 - e^{-R\Delta x}$  is about 0.85.

The physical processes that may affect  $R$  is worth discussion. Since  $e^{-R\Delta x}$  provides a weighting between the ensemble and the minimum length scales, conceivably, it is largely affected by the shape of the energy density spectrum. As a result, factors affecting the property of the energy density spectrum should eventually affect the magnitude of  $R$ . The results here were obtained from measurements within convective BLs over the ocean. In general,  $R$  may differ as the BL stability varies, which is a main factor affecting the boundary layer turbulent spectra. However, as revealed by Kaimal et al. (1976), the stability dependence of the turbulence spectra in the convective boundary layer is much weaker compared to that of the stable boundary layer. Consequently, we do not expect significant variation of  $R$  for other cases.

Equation (3.3) will not approach the LES length scale presently used in most of the LES models at  $\Delta x$  smaller than 100 m, the minimum filter scale used in our length scale calculation. Ideally, instead of using a constant  $\Lambda_{200m}$ , one should use the LES length scale which is also a function of the filter scale  $\Delta x$ . This is left for future research.

This experiment illustrates two major points. First, we can make the analogy that, for a given model resolution  $\Delta x$ , the turbulent length scale (mixing length) required to appropriately represent SGS turbulence is represented by the observations and associated curve for an  $L$  of  $2\Delta x$  as shown in Figure 3.9. It is clear that the mixing length profile that accounts for all scales of turbulent eddies in the BL (i.e.,  $\Lambda_{ENS}$ ) is inappropriate for the COAMPS BL parameterization scheme when the resolution is less than around 1.5 km. Thus, the parameterization scheme overestimates the SGS turbulent fluxes and the TKE, based on Equations 2.7 through 2.16 in chapter II. The formulation we derive from observations is the basis for an appropriate scale-dependent mixing length for model turbulence parameterization schemes when the model resolution is smaller than the size of large turbulent eddies. This formulation also provides a smooth transition from an ensemble mixing length, when  $\Delta x$  is large, to a typical LES turbulent parameterization mixing length, when  $\Delta x$  is small. In essence, the appropriate mixing length profile for a given  $\Delta x$  in Equation 3.3 is a weighted average between a typical mixing length profile appropriate for an LES model (appropriate for eddies scaling in the inertial sub-range and

below) at the small end, and a mixing length profile of the mesoscale model (appropriate for all scales of turbulence) at the large end.

#### **4. Conclusions**

As the resolution of mesoscale NWP models approaches the turbulence scales, the appropriateness the mixing length used in ensemble parameterization becomes questionable. The filter scale applied here to the calculation of the integral length scale is analogous to twice the horizontal grid resolution of NWP models. For example, a filter scale of 1 km gave an appropriate integral length scale representing eddies scaling 1 km or less. A high-resolution NWP model using a horizontal grid resolution of 500 m should parameterize all turbulence on the SGS, which is technically 1 km for this resolution. Thus, as discussed in chapter II, the mixing length used in the parameterization of the SGS eddies should also represent the 1 km and smaller eddies, and should not use a mixing length representing the turbulent eddies from all scales. Examination of Figure 3.9 provides the justification for this argument, as well as providing guidance in adjusting the length scale within the COAMPS model to appropriately consider the scales of turbulence that are being parameterized when the horizontal resolution is in and below the range of scale of the largest turbulent eddies. The formulation derived (Equation 3.3) will be needed to adjust to the current COAMPS MY82 mixing length formulation and will be tested in COAMPS in chapter V.

## **IV. CASE STUDY USING HIGH-RESOLUTION COAMPS™**

### **A. INTRODUCTION**

Using COAMPS™, we simulated a cold air outbreak (CAO) case during the JES experiment in which extensive roll vortices were observed. In this chapter, we will introduce this case and present the simulated COAMPS™ results. The objective of the initial COAMPS™ simulation of this case study is to analyze the model's performance at high-resolution (500 m). We will compare the high-resolution model output fields with satellite imagery, aircraft observations, and results of past studies on similar weather phenomena, to determine the model's ability to predict the state of the atmosphere, on both the mesoscale and turbulent scales. This chapter also discusses the effects of model horizontal diffusion and advection on the model results. The results of the initial case study will serve as the baseline simulation (or control run) with which we can compare the results from a modified COAMPS™ simulation.

### **B. COAMPS™**

The mesoscale model used in this research is in the Navy's Coupled Ocean-Atmosphere Mesoscale Prediction System (COAMPS™) developed at the Naval Research Laboratory (NRL), Monterey, CA. COAMPS™ is described in detail in Hodur (1997) and Hodur and Doyle (1998). The model includes a data assimilation system, non-hydrostatic atmosphere model components, a hydrostatic ocean circulation model, and an ocean wave model. The atmospheric and ocean models can be used separately, or in a fully coupled mode (still in development) which allows surface fluxes of heat, momentum, and moisture to be exchanged across the air-ocean interface every time step.

The COAMPS™ atmospheric model is currently used operationally by U.S. Navy forecasters for short-term regional forecasting (up to 72 hours), and is designed for both idealized and real data simulations. For real data simulations (performed in this study), COAMPS™ uses a complete data assimilation system comprised of data quality control, analysis, initialization, and forecast model components. The model grid projection is

specified along with the latitude and longitude of any one point in the grid, making COAMPS™ globally locatable. The model utilizes nested grids, allowing any number of meshes, with a 3:1 ratio reduction in grid spacing between the grids. Inner grids can be specified arbitrarily within the confines of the next coarser grid, allowing the highest resolution to be focused over a specific region of interest.

The COAMPS™ data analysis routine produces a set of initial conditions for the forecast model. The analysis specifies 3D atmospheric fields and lateral boundary conditions from the interpolation of global atmospheric model analysis or forecast fields generated by the Navy Operational Global Atmospheric Prediction System (NOGAPS) to the COAMPS™ grid(s). The interpolated COAMPS™ analysis fields for the u and v wind components and geopotential height are blended with real-time observations (such as rawinsonde, SSMI, satellite-derived data, and aircraft observations), if available, using 3-dimensional multi-variate optimum interpolation (MVOI) analysis. These model and observation fields are available from the Fleet Numerical Meteorology and Oceanography Center, Monterey, CA. In addition to the initial atmospheric fields, several surface conditions are set with various fields. Surface terrain height is obtained from the Defense Mapping Agency (DMA) Digital Terrain Elevation Data (DTED) level 1 data (1 km resolution), and is bilinearly interpolated to the COAMPS™ grid(s). Surface albedo, surface roughness, ground temperature, and ground wetness are also specified initially. Monthly climatological global fields of albedo and surface roughness are bilinearly interpolated to the COAMPS™ grid(s). Albedo is set to 0.09 over the water. Ground wetness and ground temperature are specified from a previous COAMPS™ forecast if available. SST is set by bilinearly interpolating the Fleet Numerical Meteorology and Oceanography Center (FNMOC) global SST analysis to the COAMPS™ grid(s).

The COAMPS™ analysis is performed on the Arakawa-Lamb scheme A grid (no staggering), while both the horizontal and vertical grids in the forecast model are staggered. Scalar forecast variables are defined at the center of the model grid box, with the forecast wind fields defined at half the grid distance from the center of the model grid box. The analysis fields are interpolated to the initial forecast fields using a bicubic spline to the Arakawa grid C grid configuration (staggering) in the horizontal, then

interpolated in the vertical to the model vertical coordinate. The vertical coordinate in COAMPS<sup>TM</sup> is a terrain-following sigma-z system (Gal-Chen and Somerville 1975).

The equations used in the COAMPS<sup>TM</sup> atmospheric model are comprised of a non-hydrostatic, compressible formulation of the primitive equations, and parameterizations for the sub-grid scale mixing, surface fluxes, explicit moist physics, cumulus convective processes, and radiation. The equations are solved in three dimensions with the terrain-following sigma-z vertical coordinate. The complete list of prognostic equations and their origination is found in Hodur (1997). The numerical scheme used is the leapfrog (centered-in-time, centered-in-space) second-order differencing. The PBL and free atmospheric turbulent mixing and diffusion are modeled after MY82 as described in chapter II.

## **C. JES CASE STUDY - DESCRIPTION**

### **1. Overview**

In this section we describe the weather event that will be simulated in our study. The entire modeling region (Figure 4.1) expands to the west over North and South Korea and eastern China, to the north over part of southern Russia, and to the east and south over the larger part of the JES. The small region of interest that will enclose the high-resolution domain of our simulation (outlined in Figure 4.1) is centered over the western JES south of Vladivostok, located at approximately 41 to 42 degrees north latitude and 132 to 133 degrees east longitude, enclosing about 1000 km<sup>2</sup>. The coastal mountain ranges west of the JES, the Hamgyong and Taebak Mountains in Korea and the Sikhotealin Range in Russia, are also seen clearly in Figure 4.1. A summary of the synoptic situation and resulting mesoscale weather features for the case, using descriptions from Dorman et al. (2002), is given below. A discussion of convective roll vortices, the main weather phenomenon of this case, is also presented.

### **2. Synoptic Conditions for JES0216**

On February 16 and 17, 2000, a Very Cold Siberian Air Outbreak (VCSAO) occurred over the JES. As described in Dorman et al. (2002), these events occur just a

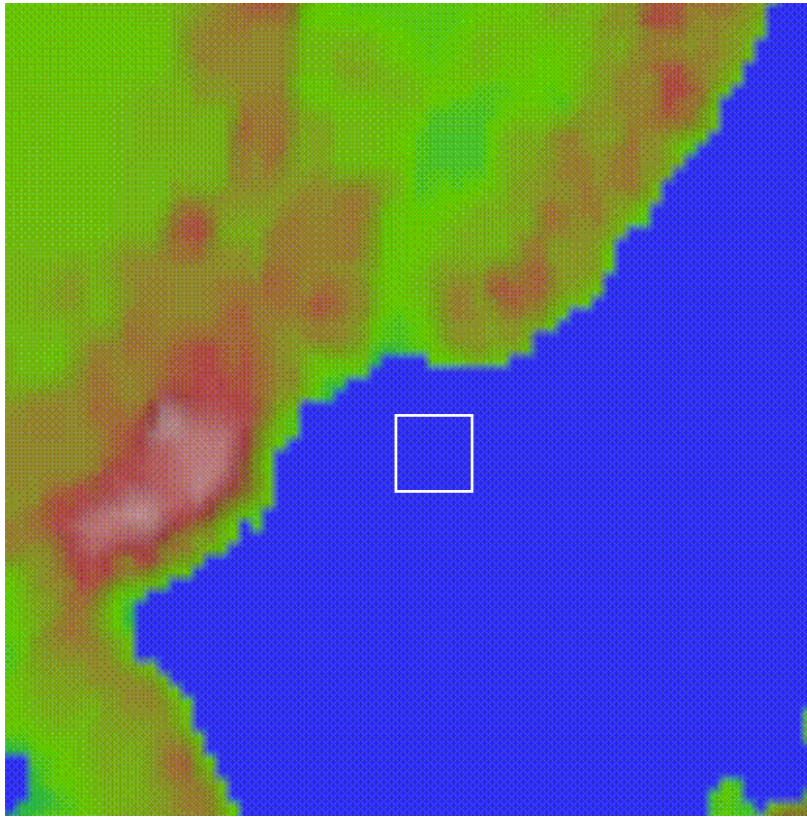


**Figure 4.1.** Region of model simulation, centered over the JES. The high-resolution domain of the simulation, the region of interest, is outlined in the figure. The coastal mountain ranges are seen as the shaded red regions.

few days a month during the winter over the JES. A VCSAO occurs when the Siberian High moves farther south of its mean position, generating northerly winds with  $-30^{\circ}$  to  $-20^{\circ}$  C air over the Russian Coast and JES, initiating a strong CAO. The The Navy Operational Global Atmospheric Prediction System (NOGAPS<sup>TM</sup>) analysis fields of pressure and 1000 to 500 mb thickness for 16 Feb 2000 1200Z and 17 Feb 2000 0000Z (Figure 4.2) and the vertical p-velocity ( $\omega$ ) at 850 mb for 17 Feb 2000 0000Z (Figure 4.3b) show that the Siberian high is indeed located farther south into China, directly west of the JES, creating subsidence (indicated by the positive  $\omega$  values) over our small region of interest. NOGAPS<sup>TM</sup> analysis fields also show that the cold front associated with the low pressure center northeast of the JES, and strongest cold air advection, has already moved east of the JES, indicated by the strong gradient of thickness contours in this region. Even though the thickness gradient is now weaker over our region of interest, very cold air, indicated by the low thickness values, continues to be advected eastward over the JES. The NOGAPS<sup>TM</sup> analyses in Figure 4.2 also show that the synoptic conditions have not changed much in the 12 hours between these analyses.

Ten-day composite SST imagery (1 to 10 February 2000) from the National Ocean and Atmospheric Administration's polar orbiting satellite number 15 (NOAA-15) Advanced Very High-resolution Radiometer (AVHRR) and the NOGAPS<sup>TM</sup> SST analysis (Figure 4.4) show the structure and gradient of the SST field for this case. The NOGAPS<sup>TM</sup> SST analysis was uniformly reduced  $2^{\circ}$  C to better match the magnitude of observed SST in our region of interest in the western JES. This corrected SST analysis will be used in the initialization of our COAMPS simulations. The satellite imagery and NOGAPS analysis show near  $0^{\circ}$  C SST over our small area of interest, while a stronger NW to SE SST gradient, from colder to warmer temperatures, exists over the southeastern JES. The equivalent potential temperature at 1013 mb (Figure 4.3a) indicates that the near-surface air temperature, between 258 and 264 K in our region of interest, is 8 to  $10^{\circ}$  C cooler than the SST. The large air-sea temperature difference is the driving force in the down-wind development of the turbulent BL over the JES for this case, as the BL air warms as it moves over the relatively warmer ocean, generating large surface fluxes of heat and moisture.

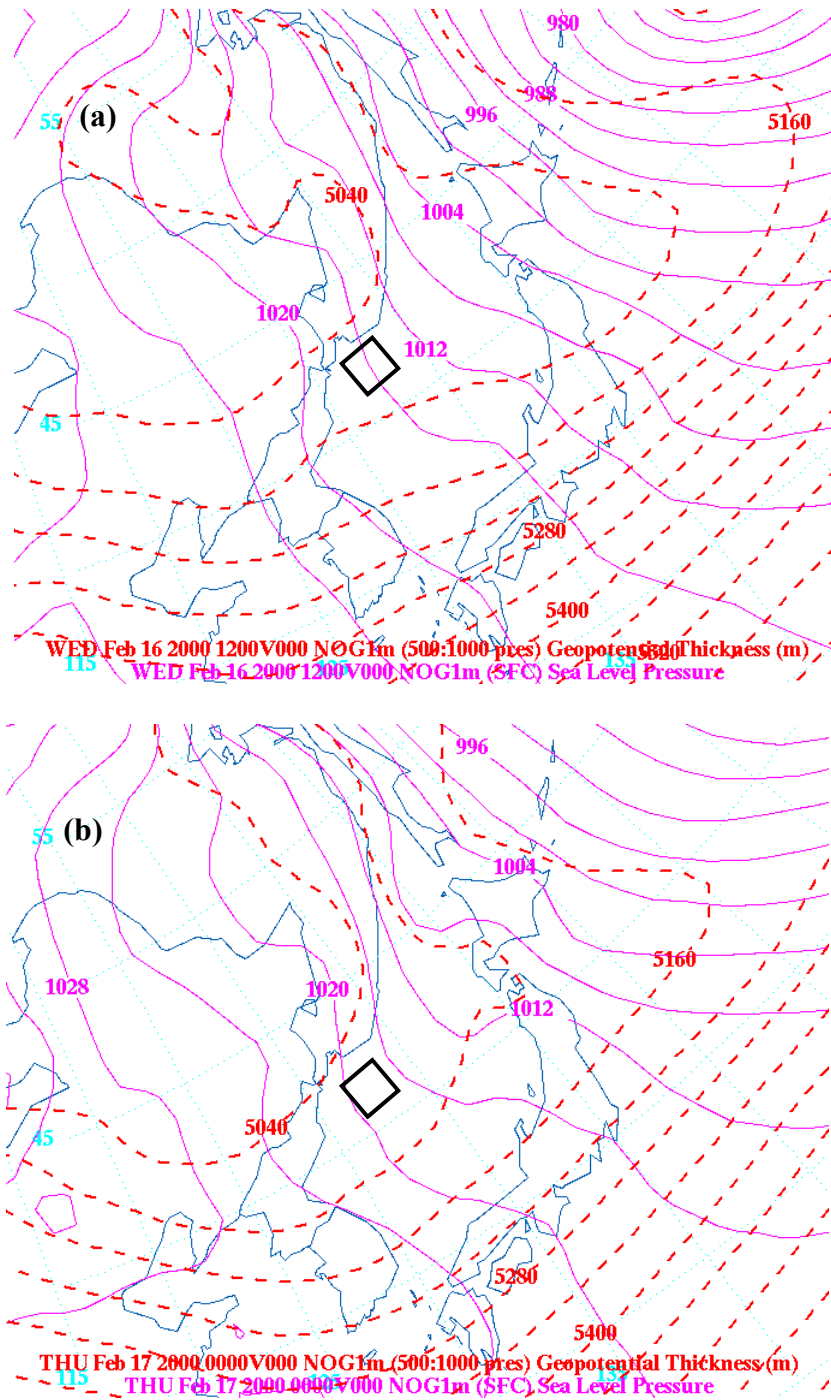


**Figure 4.2.** NOGAPS Global Analysis Fields, Valid (a) 16 Feb 2000, 1200Z and (b) 17 Feb 2000, 0000Z, showing mean sea level pressure in millibars (solid) and geopotential thickness in meters (dashed). The region of interest for the high-resolution domain is outlined.

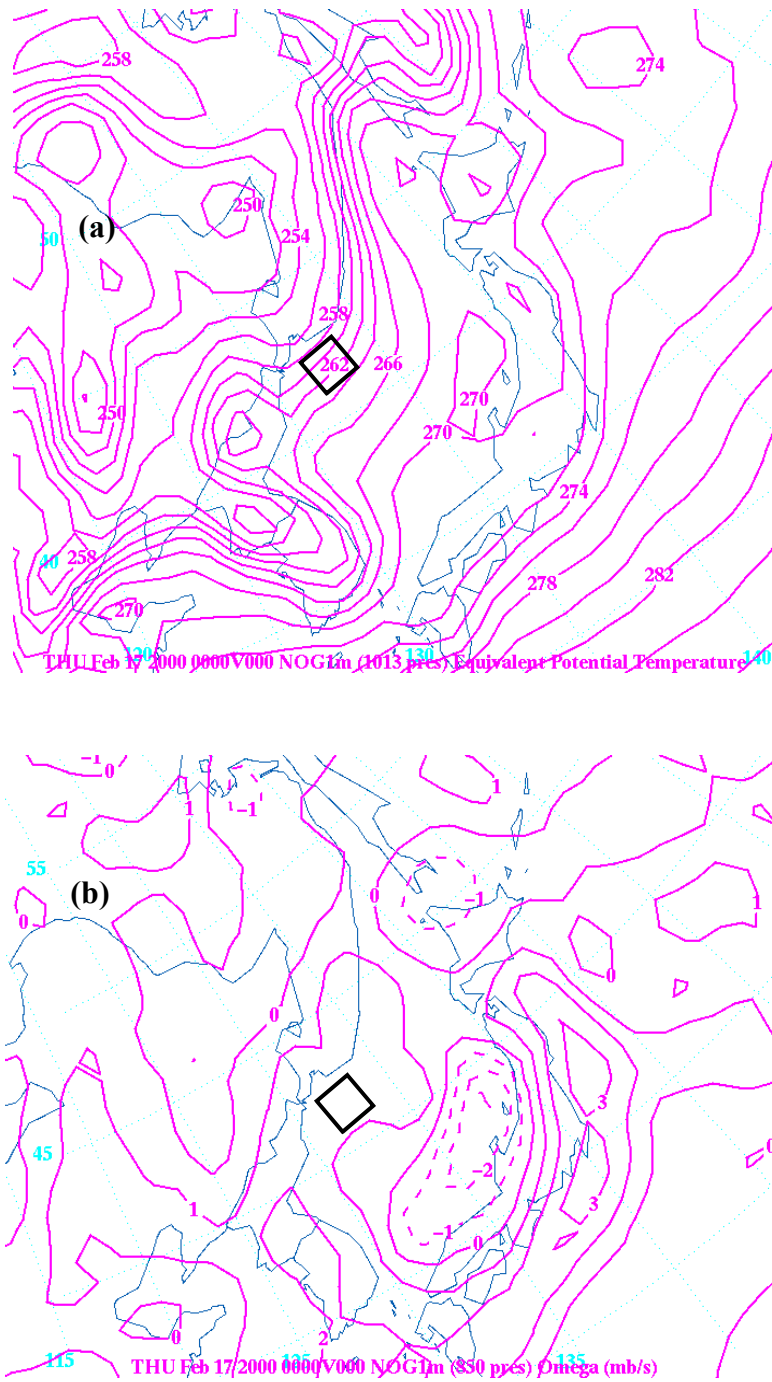


**Figure 4.3.** Same as in Figure 4.2, except for (a) near-surface equivalent potential temperature (K) and (b) omega (mbs<sup>-1</sup>). The region of interest for the high-resolution domain is outlined.

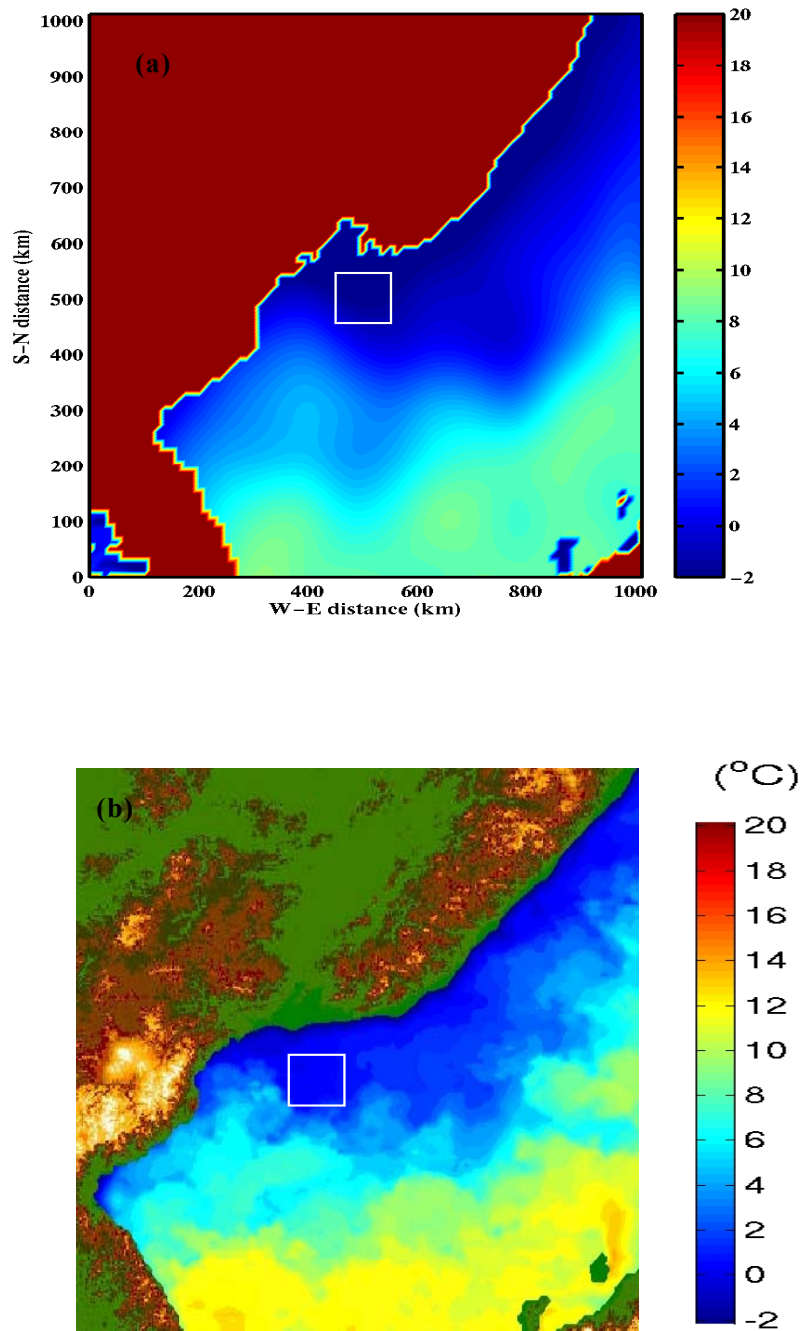


**Figure 4.4.** SST (in degrees C) variation over the JES. (a) NOGAPS SST Field for 16 February 2000, 1200 Z. (b) 10-day composite (1 to 10 February 2000) SST derived from NOAA AVHRR Satellite Imagery. The region of interest for the high-resolution domain is outlined.

Dorman et al. (2002) discusses the differences between typical CAO conditions and VCSAO conditions over the JES. In typical CAO conditions, a strong surface inversion and weaker northerly winds trap the coldest inland air to the west of the Russian coastal mountains. Reduced drag over the JES causes surface divergence, which pulls air down the lee of the mountains and adiabatically warms the coastal air such that the air-sea temperature difference is only around 5°C. In VCSAO conditions, the much colder surface air, which reduces stability and eliminates the surface inversion, coupled with stronger winds, allows much colder air to advect over the mountains and out over the JES compared to the typical CAO, creating much larger air sea temperature differences and surface heat fluxes. These differences between typical CAO and VCSAO conditions result in the larger magnitude of turbulence and more extensive and detailed formation of heat-flux driven horizontal roll vortices and cloud streets in the VCSAO. The VCSAO case of 17 February 2000, our case study, will be referred to from here on as JES0216.

### **3. BL Roll Vortices**

#### ***a. Satellite Imagery***

We can see the down-wind development of the BL over the JES on 17 February 2000 from the cloud structure. Visible satellite imagery from the Japanese Meteorological Agency (JMA) geostationary satellite (Figure 4.5) shows 80% of the Japan/East Sea covered in convective roll clouds and stratus. The clouds appear to be more roll-like in the western JES, in the region of stronger large-scale subsidence shown in the omega field (Figure 4.4), and more cellular in the eastern JES near Japan, where omega at 850 mb is negative and the large-scale subsidence is absent in the presence of the upper-level trough (not shown). There is a line of thin clouds streaming off the Russian coast and thorough the center of our region of interest (outlined in Figure 4.5), while the thickest clouds form farther off shore where there is more BL turbulence to generate large eddies and moisten the originally dry continental air to the point where low-level convective clouds develop at the top of the BL below the inversion. Roll vortices were observed over the JES on several days during the JES experiment (Dorman et al. 2002) in addition to the JES0216 case.

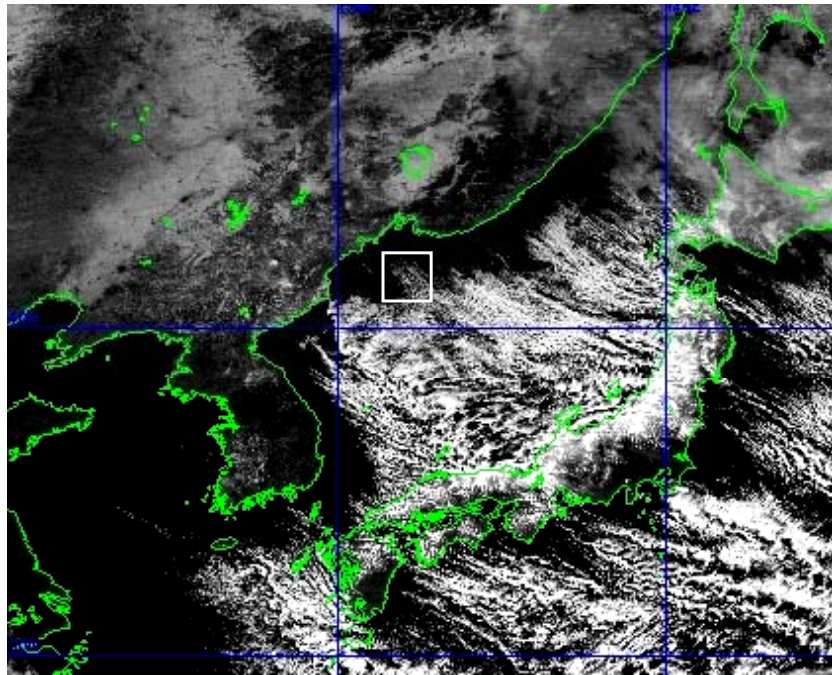


**Figure 4.5.** JMA visible satellite imagery over the JES on February 17, 2000, 0200 Z. Thin cloud streets are present within the region of interest (outlined).

*b. General Structure and Characteristics of Roll Vortices*

Roll vortices are frequently observed in the marine BL, especially in CAO conditions. Etling and Brown (1993) and Young et al. (2002) provide reviews of the convective roll vortices. They loosely define roll vortices as quasi two-dimensional (i.e., nearly linear) organized large eddies, extending through the entire depth of the PBL, with properties different from those of small-scale turbulence. Occurring usually in high wind conditions, these features exhibit coherent perturbations in the wind, temperature, and humidity fields (e.g., LeMone and Pennell 1976). The rolls contribute significantly to the vertical fluxes of heat, moisture, and humidity from the surface through the entire depth of the PBL, and thus play a significant role BL in mixing, transport, and entrainment processes.

A common feature associated with roll vortices, but not always present, is the manifestation of so-called cloud streets that are easily seen in satellite imagery (Figure 4.5). If adequate moisture is present for their formation, clouds streets can form in the updraft regions of the roll circulations, while cloud-free areas exist in between the streets in downdraft regions. The rolls and associated cloud streets are usually oriented more or less parallel to the mean PBL wind direction. Cloud streets are most impressively formed during cold-air outbreaks over the oceans, but can form over land as well. Figure 4.6 shows a simple schematic of horizontal roll vortices structure and the resulting cloud streets in the PBL.

Etling and Brown (1993) cite many studies that have been conducted, for both over land and over ocean cases, to investigate the vertical and horizontal structure of roll vortices. The results can be summarized as follows:

|   |            |
|---|------------|
| Vertical Extent (H)                       | 1-2 km     |
| Wavelength/horizontal scale ( $\lambda$ ) | 2-20 km    |
| Aspect ratio ( $\lambda/H$ )              | 2-15       |
| Down-wind extent (E)                      | 10-1000 km |

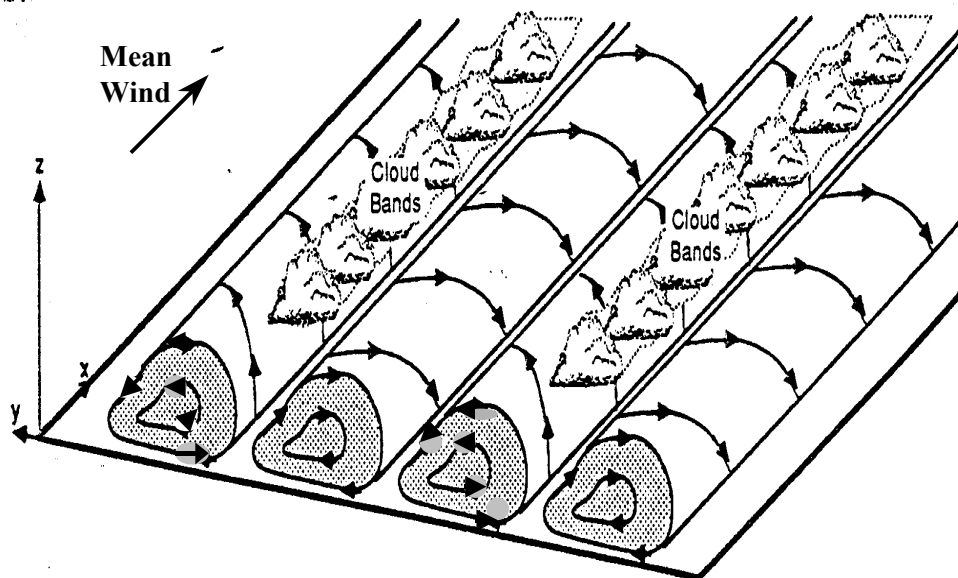


**Figure 4.6.** Typical horizontal roll vortices in the planetary BL (from Stull 1988).

|  |                |
|--|----------------|
| Orientation of roll axis to the mean wind ( $\epsilon$ ) | -20 to +30 deg |
| Life time ( $\tau$ )                                     | 1-72 h         |

The rolls have a vertical scale roughly equal to the BL depth, and a wide range of horizontal scales, leading to a wide range of aspect ratios. Observational and LES modeling results summarized by Young et al. (2002) give the aspect ratio as a function of BL depth. The results are somewhat varied, but for CAO cases with BL depths near 800 m (similar to JES0216), aspect ratios between 4 and 7 are most common. High-resolution observations indicate the presence of multiple thermals within the roll updraft regions (Brummer 1999). Typically, two or three stronger updraft “cores”, rather than a single updraft, are located within a region of overall weak roll updrafts, leading to a rather frothy appearance in satellite imagery for any associated cloud streets, as is apparent in Figure 4.5 for JES0216.

Conditions for the formation of these rolls has been the subject of many observational studies (see Brown 1980). The cause of the rolls has been attributed to both shear instability of the Ekman BL (inflection point instability) and convective instability, but typically a combination of these two instability mechanisms generates the roll structure. However, it has been shown by Brummer and Latif (1985) and by Etling and Raasch (1987) that inflection point instability is suppressed when the height of the inflection in the BL wind is greater than  $6z_i$ . In general, theory suggests that roll vortices occur for all convection regimes in the presence of little shear, and for neutral and even slightly stable stratification in the rotating frame of reference. Nearly all field studies of roll vortices have been conducted during CAO’s over the ocean, or in the daytime PBL over land, which implies that the rolls are related to unstable stratification and convective instability. Thus, these large eddies routinely form in an unstably stratified PBL heated at the surface.

The parameter,

$$\frac{z_i}{L} = -\frac{g}{\theta} \frac{z_i \kappa (\overline{w'\theta'})_0}{u_*^2}, \quad (4.1)$$

where  $L$  is the Monin-Obukov length scale for the surface layer, is often used as a measure of PBL stratification, and has become the criterion measurement for the onset of roll convection. Numerical and observational studies of convective BLs (see Etling and Brown 1993) related types of thermal convection to  $z_i/L$  as a stratification parameter with a negative  $z_i/L$  indicating thermal instability. Studies conclude in general that for  $-5 < z_i/L < -1.5$ , convection with roll vortices may exist, but for  $z_i/L < -25$ , three-dimensional convection is more likely. Hence the roll-regime exists in the unstably stratified regime,  $-25 < z_i/L < -1.5$ , but Etling and Brown (1993) state that roll vortices and cloud streets will most likely be observed for moderately unstable stratification,  $-15 < z_i/L < -5$ , with  $z_i/L$  usually less (more) negative for moderate (low) winds and moderate (strong) surface heating.

Because of the quasi two-dimensional structure of rolls, many two-dimensional modeling studies of these features have been employed. The first modern numerical attempt at simulating roll development was due to Mason and Sykes (1980) who used a finite difference model to simulate the development of roll vortices for the neutrally stratified BL. These authors extended their work to investigate various aspects of two-dimensional roll circulations in the unstably-stratified BL (Mason and Sykes 1982; Mason 1983; Mason 1985). Three-dimensional modeling of roll vortices has mostly been limited to LES modeling of the PBL. Numerical studies by Chlond (1992) and others cited in Etling and Brown (1993) indicate that large-eddy simulations of cases with convective instability produce roll vortices in the PBL. However, in contrast to 2-D numerical results and observations of PBL rolls, they do not show up clearly as permanent features (showing up at early integration times, then disappearing later on). The lack of permanency may be attributed to the limited domain sizes used in these LES experiments. Modeling of roll vortices using high-resolution mesoscale models has not yet been documented.

Complicating a simple picture of these two-dimensional rolls are other smaller scale PBL eddies, whose energy exchanges with the rolls may be important. As was illustrated in chapter III, partitioning of PBL vertical fluxes due to different scales of motion, i.e. small scale turbulence and larger eddies, may be done using spectral analysis

of observations or model results. Spectra of aircraft measurements during the GALE experiment analysis performed by Chou and Zimmerman (1989) illustrate that the mean vertical fluxes of heat, momentum, and moisture can be attributed to vertical motions on different scales: small scale turbulence ( $\lambda < 200$  m), thermal plumes ( $200 \text{ m} < \lambda < 2 \text{ km}$ ), and roll vortices ( $\lambda > 2 \text{ km}$ ). The energy exchange between large and small scale turbulent eddies implies the importance of correctly estimating the turbulent scale energy in a mesoscale NWP model in order to correctly predict the roll structure occurring on the mesoscale.

*c. Aircraft Observations*

Aircraft observations, from level legs near the surface and BL soundings, were taken within our small region of interest during the JES experiment on 17 February 2000 0000Z. Three level flight legs, each flown at a height of about 40 meters, and ten soundings through the depth of the BL were flown within this region. Specific times and exact locations of the flight legs and soundings can be found in Table 3.1. The general locations of the flight legs and soundings within the region are shown in Figure 4.7. The three level flight legs were flown in the East-West direction, located in northern, central, and southern positions within the region. These three legs were flown within one hour, between 0100 Z and 0200 Z. The high-rate (10 Hz) aircraft observations from the near-surface legs are filtered here to remove variations greater than 0.1 Hz for visual presentation. The BL soundings were made between heights of 35 m to 917 m above sea level. Eight of the sounding legs were flown in a zig-zag pattern in the vertical, forming a vertical cross-section in the along-wind direction (see Figure 4.10). These observations reveal the structure of the BL on this day in more detail.

Figure 4.8 shows the time series of vertical velocity, absolute humidity, and potential temperature from the near-surface flight legs. With the level flight legs oriented at about a 45 degree angle to the mean wind direction, the surface layer observations reveal both a signal of the down-wind development of the BL while at the same time traversing across the updraft and downdraft regions of the turbulent rolls. As expected, there is a general moistening and warming of the air mass, both from north to south and east to west. There is a well-defined oscillation in the temperature and water

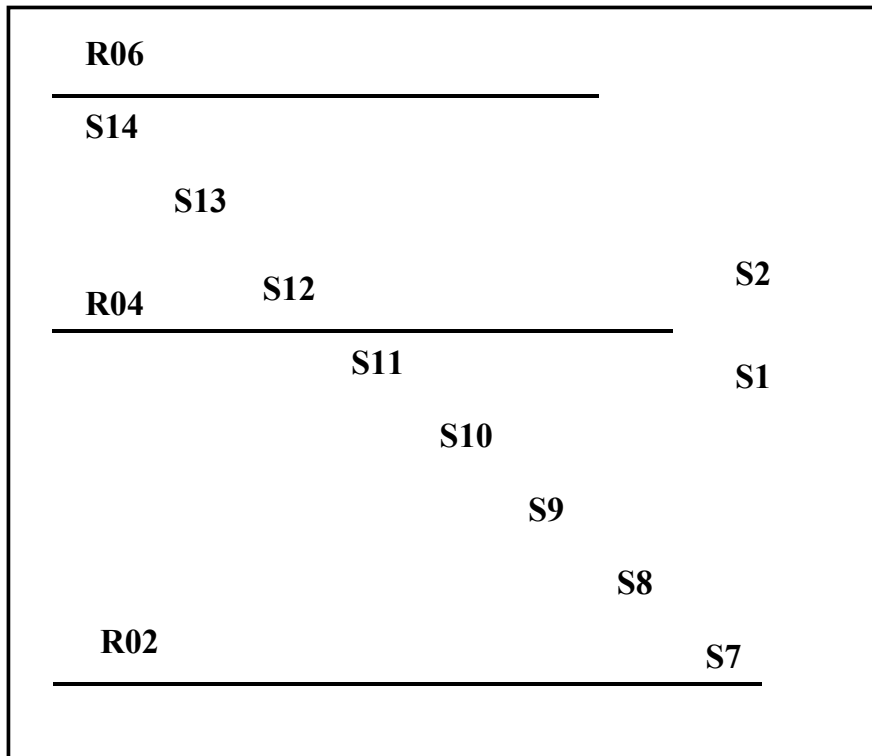


**Figure 4.7.** (a) General location of aircraft observation legs and soundings within the region of interest over the western JES (outlined region in figures 4.1 through 4.5).

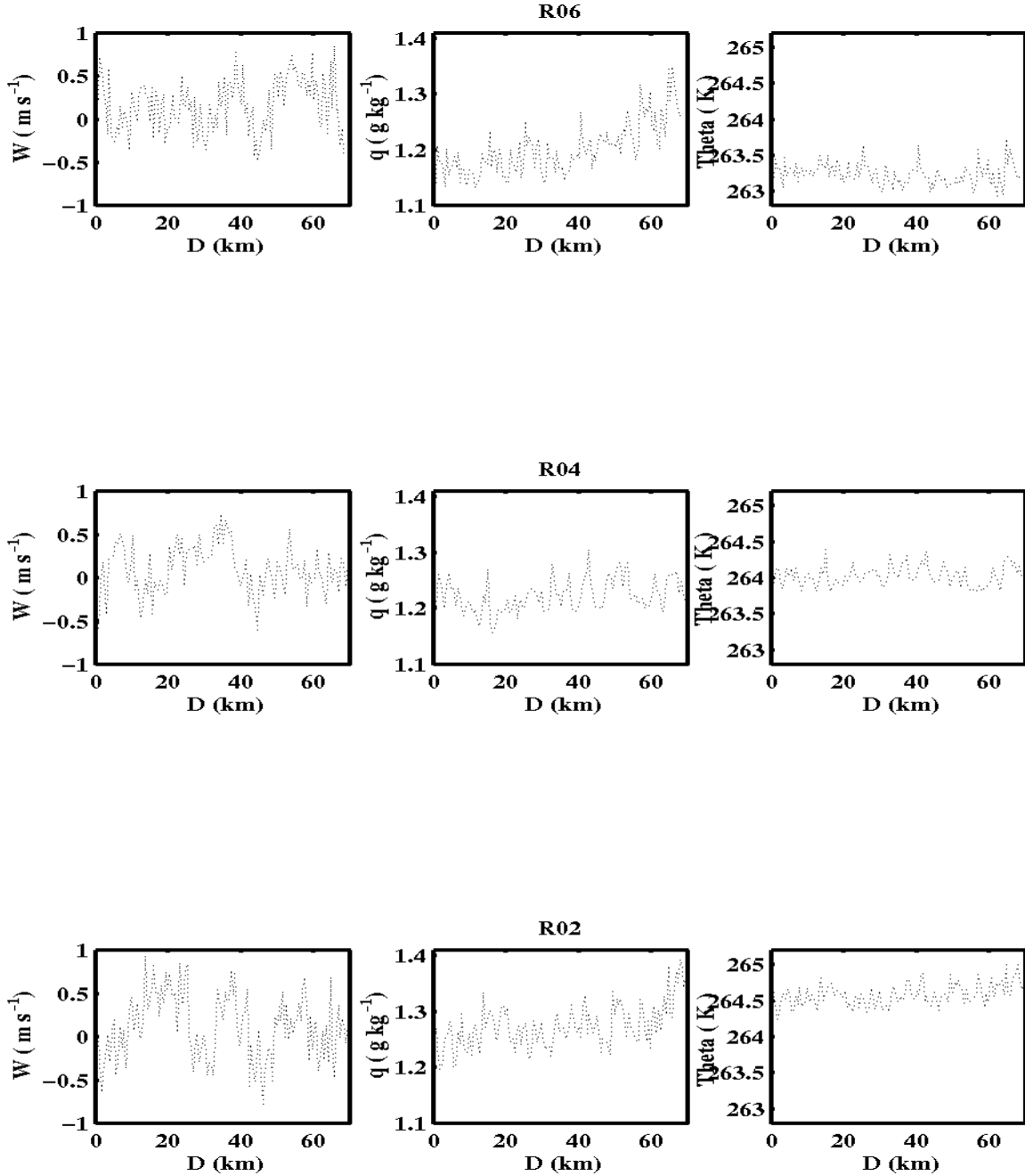


**Figure 4.8.** From left to right: Observed vertical velocity ( $\text{m s}^{-1}$ ), water vapor ( $\text{g kg}^{-1}$ ) and potential temperature (K) from near-surface (40 m above sea level) flight legs from north (R06) to south (R02) in the region of interest in the western JES. Observations taken 17 Feb 2000, 0100Z – 0200Z. Horizontal axes are distance ( $D$ , in km) from the beginning of the leg. See Figure 4.7 for the location of the flight legs.

vapor traces, which shows the presence of the roll vortices. The peaks of higher temperature and water vapor are collocated, as expected, with the peaks in vertical velocity, as warm, moist air is transported upward from the ocean surface within updrafts. The vertical velocity is also seen to become more variable and larger in magnitude from north to south as the BL develops and becomes more turbulent, with stronger and more clearly defined updraft and downdraft regions. We also observe the stronger updraft cores within regions of weaker upward vertical velocity, as is commonly observed in cases of roll convection (Young et al. 2002). The length scale of the rolls can be seen most clearly in the western half of the central and southernmost legs, where the horizontal distance between successive updraft regions and peaks in moisture is 5-7 km. Accounting for the aircraft flight path with respect to the mean horizontal wind direction and roll orientation, the actual scale of the rolls is likely closer to 3-5 km. Assuming the BL depth is around 850 m, based on the maximum height of the BL soundings, the roll aspect ratio is 4 to 6. These values of roll scale and aspect ratio are in agreement with cases of roll convection as described earlier.

Figure 4.9 reveals more typical BL conditions associated with a convective roll vortex regime. The Figure presents the time series of surface layer wind, air-sea temperature difference, and combined sensible and latent heat fluxes from the three near-surface level flight legs. The flight level winds range from 13 to 16 m s<sup>-1</sup> and air-sea temperature differences in the western JES are around 8.5 degrees, resulting in surface heat fluxes (sensible and latent heat) of up to 250 W m<sup>-2</sup>. We see that the combination of higher wind and large air-sea temperature difference creates the largest heat fluxes along the northernmost leg. The decrease in heat flux from north to south appears to be dominated by the corresponding decrease in wind speed. The vertical cross-sections in Figure 4.10 are derived from aircraft soundings in the intensive measurement area. The cross-sections show clearly that, in the down-wind direction (left to right in the cross-section), the BL is indeed undergoing slight warming (Figure 4.10 b) and moistening (Figure 4.10 a), as was also shown in the near-surface observations. It is also evident that the BL is becoming moister at higher levels down-wind. As a result of turbulent mixing in the boundary layer, the initially dry air originating from over land

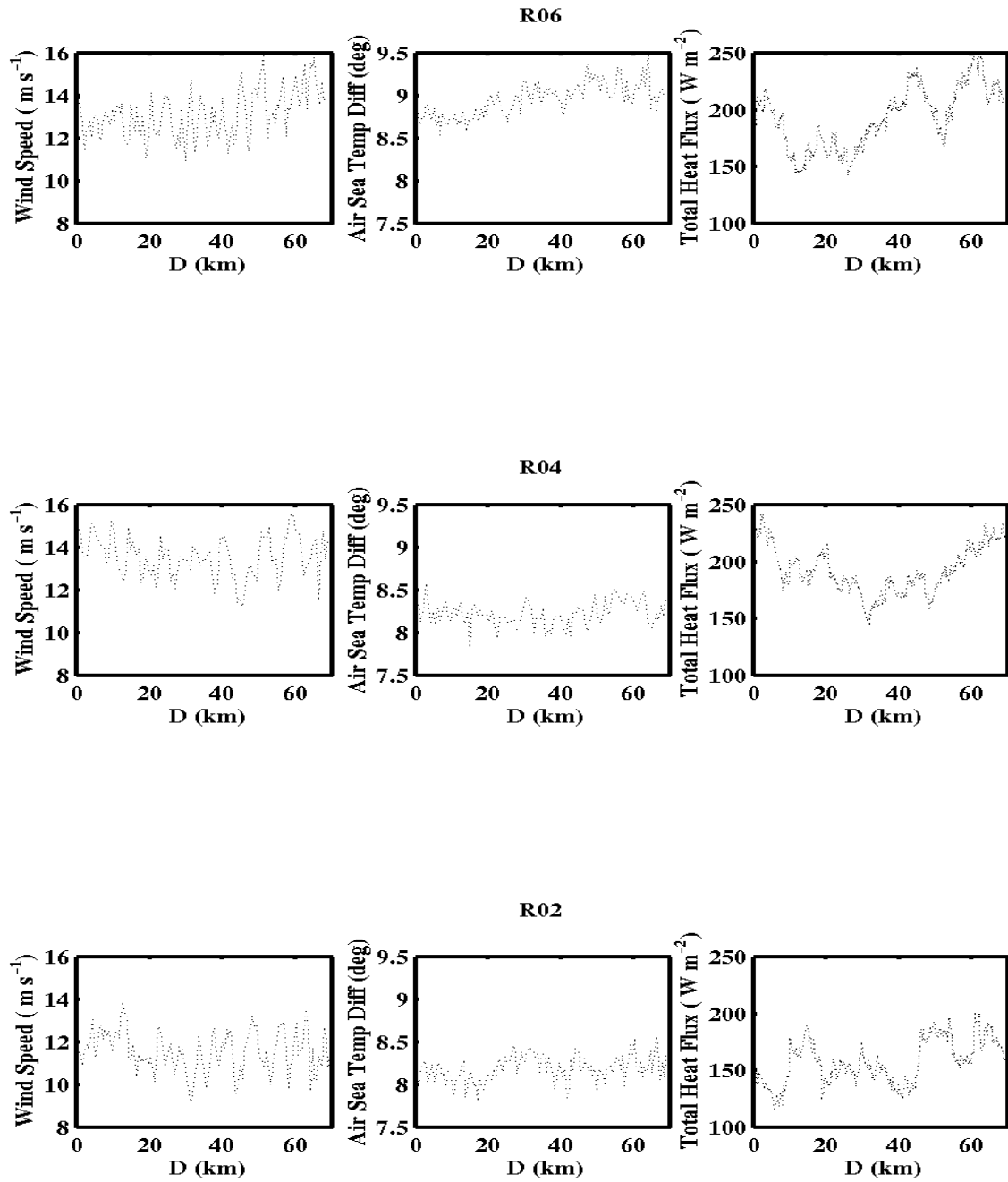


**Figure 4.9.** Same as Figure 4.8, except for (from left to right) horizontal wind speed ( $\text{m s}^{-1}$ ), air-sea temperature difference (K), and Total (latent and sensible) heat flux.

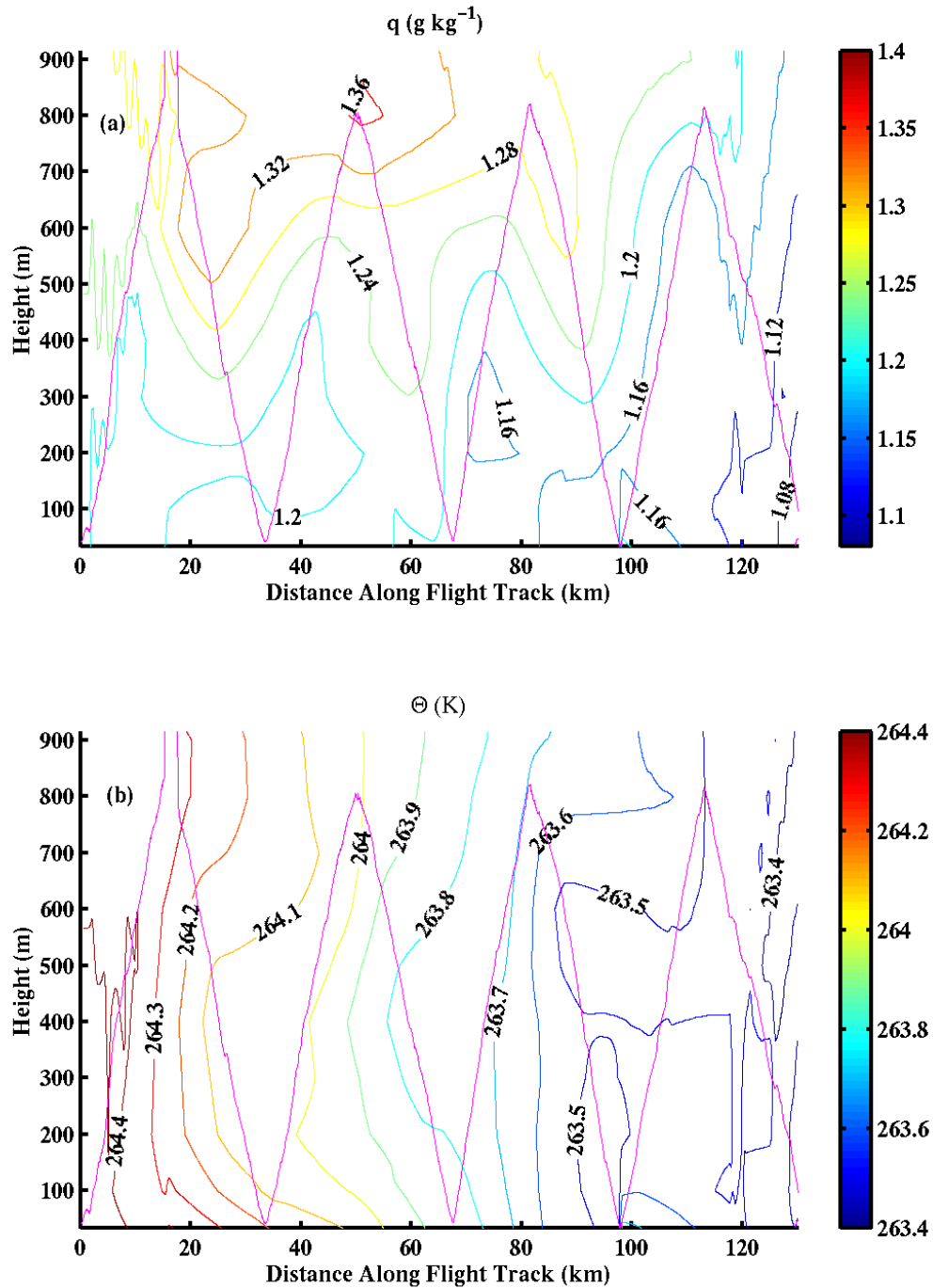


**Figure 4.10.** BL cross-sections in the up-wind direction (along the flight track) of (a) water vapor ( $\text{g kg}^{-1}$ ) and (b) potential temperature (K) derived from eight sounding legs. The sounding flight track is shown within the contour plots. See Figure 4.7 for the locations of the soundings.

gradually moistens reaches to higher and higher levels with down-wind distance within the BL, where the roll clouds eventually form in the updraft regions. In addition, Figures 4.10 a and b reveal that the aircraft soundings did not reach the inversion layer normally above the boundary layer since there is no inversion present from the soundings. Thus, the boundary layer top is above 900 m. The inversion is probably only slightly higher than 900 m, since the experiment soundings are intended to cover the entire depth of the BL (Kheilf et al. 2003). Assuming a BL depth of 950 m, and taking the mean potential temperature of the BL from the JES soundings, the surface layer sensible heat flux, and  $u^*$  calculated from the surface layer flux legs, the average  $z_i/L$  in the BL for our region of interest is  $-5.1$  (Equation 4.1). This value, predicting a moderately unstable regime, falls within the range of  $z_i/L$  given in the literature for convective roll development.

#### **D. DESCRIPTION OF COAMPS<sup>TM</sup> SIMULATIONS OVER THE JES**

We performed a high-resolution COAMPS<sup>TM</sup> simulation over the region of interest in the JES and for the JES0216 case described in the previous section. The modeling region consisted of 4 nested domains. The horizontal resolutions, sizes for each domain, and simulation times for the simulation are described in Table 4.1, and the locations of the domains are shown in Figure 4.11. The geographic locations of the outer domain (domain 1) was chosen such that the domain extended westward over the coastal mountains and farther to the west over land, such that topographic effects upwind would be simulated and modeled within the inner nests. The high-resolution inner domain, at a resolution of 500 m, was limited in size by computational constraints, and is the primary focus of this study. Unless otherwise specified, all simulation results presented will be from the JES0216 high-resolution innermost domain. The aircraft flight paths and locations of both surface layer flux legs and BL soundings within the inner 0.5 km resolution nest shown earlier (Figure 4.7) will be used in comparison to model output. The simulation start time, 12 to 16 hours prior to the time of the observations, was chosen to allow for adequate spin-up time for the model. For this simulation, the model contained 30 vertical levels, of which 12 were located below 1 km for better resolution of the marine BL. The simulation involved calculations at 30 second time steps over 16

**Table 4.1.** Domain Set Up for COAMPS™ JES0216

| Domain 1 (outer)<br>Resolution (km) / size (km <sup>2</sup> ) | Domain 2<br>Resolution (km)/ size (km <sup>2</sup> ) | Domain 3<br>Resolution (km)/ size (km <sup>2</sup> ) | Domain 4<br>(innermost)<br>Resolution<br>(km)/size (km <sup>2</sup> ) |
|---|--|--|---|
| 13.5 / 1107x 1107   | 4.5 / 585 x 585                                      | 1.5 / 272x 272                                       | 0.5 / 100 x 100   |

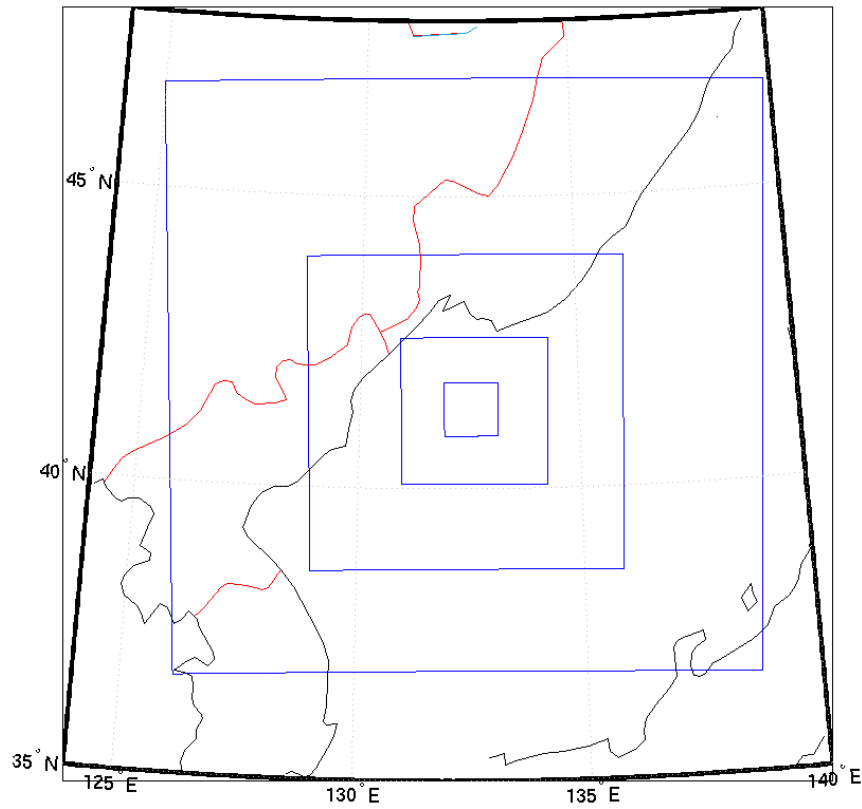


**Figure 4.11.** Four nested COAMPS™ domains over the JES region. Observation legs used for model-observation inter-comparison (shown in Figure 4.7) are within the innermost domain.

hours for  $2.88 \times 10^6$  grid points, which required a wall clock simulation time of over 120 hours running on 32 processors on a CRAY SV1ex supercomputer at the Arctic Regional Supercomputing Center in Anchorage, Alaska.

The persistence of the synoptic conditions from 16 February 1200Z and 17 February 0000Z (Figure 4.2) imply, assuming adequate spin-up time (typically around 6 to 9 hours for COAMPS<sup>TM</sup> (Hodur 1997), that a model forecast initialized from the 16 February 1200Z analysis fields of this region will be a valid representation of the development of the BL turbulent structure. It was determined by inspection of the model forecast fields throughout the forecast period that the 12-hour forecast best represents the turbulent BL structure. Thus we will present the simulated fields from the 12-hour forecast in our discussion and in comparison to aircraft observations. The observational analysis will be based on the limited set of observations available for comparison to the model results, so we will also rely on past modeling and observational studies to supplement our analysis of our case study.

## **E. ANALYSIS OF COAMPS<sup>TM</sup> SIMULATIONS**

### **1. Effects of Model Numerics**

Before we begin the analysis of the model output from the JES0216 case, a discussion on the issue of model resolvability is in order. As discussed in Pielke (2002) and Avissar et al. (1990), the energy cascade of turbulence to smaller and smaller wavelengths (described in chapter II) cannot occur in mesoscale numerical models. When wave interactions occur in the real world, a spectra of wavelengths result. Eventually the smallest eddies are removed by molecular dissipation. In a numerical model, however, the existence of a discrete grid results in aliasing in the resolvable scale phenomena due to perturbations in the SGS fields (also referred to as short waves). These erroneously produced larger scale waves again interact to produce larger and smaller waves. Because the proper cascade of energy to smaller and smaller scales is disrupted, a fictitious energy buildup occurs in the model. Pielke (2002) states that such short waves are badly handled and poorly represented in amplitude and/or phase by

various numerical schemes on a computational grid, even for linear scale advection. Thus, the solution adopted to control the shortest wavelengths is to damp or remove these waves using numerical filters. In COAMPS<sup>TM</sup> and other mesoscale NWP models, an explicit diffusion equation is used to parameterize the sub-grid scale correlation terms so that energy is extracted from the averaged equations in a manner consistent with reality. In COAMPS<sup>TM</sup>, a background second-order (for points on the grid boundaries) and fourth-order (for all other grid points) diffusion of all prognostic variables (except for pressure perturbation) is carried out on sigma surfaces. Hodur (1997) describes the form of the diffusion operator and criteria for choice of diffusion coefficients. Unfortunately, as discussed in chapter II, only the vertical sub-grid scale correlation terms are reasonably well known and can be parameterized accurately in terms of dependent variables. In contrast, horizontal sub-grid scale mixing is crudely estimated, since the horizontal averaging scale is much larger than the vertical scale, and due to a lack of understanding of the structure of horizontal mixing over heterogenous surfaces. Therefore, the form of the horizontal sub-grid scale correlation terms is chosen to control non-linear aliasing, and not to represent the actual physical processes accurately.

Avissar et al. (1990) states that because of added numerical diffusion schemes, motions on scales no less than  $4\Delta x$  are fully resolved in numerical models. However, more recent studies based on spectral analysis of model simulated fields yield slightly different conclusions. Bryan et al. (2003) conducted a series of large eddy simulations of deep moist convection using different 6<sup>th</sup> order explicit diffusion coefficients. Analysis of the energy spectra revealed a scale at which there was a discrete separation between the physical and computational solutions. They conclude that only information at scales greater than  $6\Delta x$  in the energy spectra represent a physical solution and should be considered useful in most applications. This conclusion is supported in Harris et al. (2001), who compare an explicit simulation at 3 km resolution of a squall line to radar data of the same case. Power spectrum analysis gave excellent comparisons from large scales to about  $5\Delta x$ , supporting their conclusion that only information larger than this scale can be considered physically real. Both Bryan et al. (2003) and Harris et al. (2001)

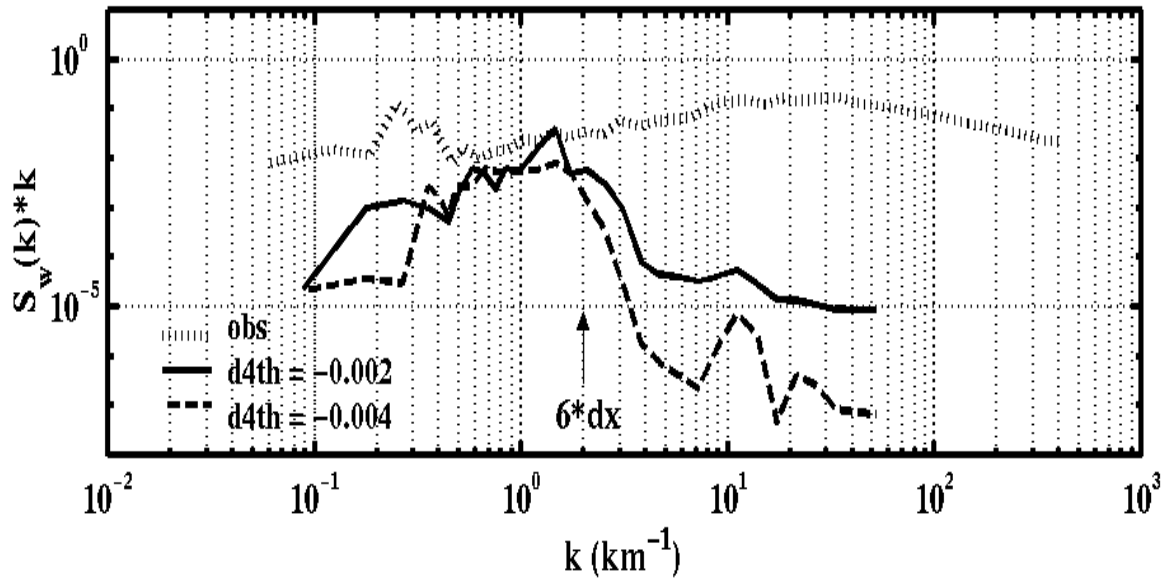


**Figure 4.12.** COAMPS surface layer vertical velocity spectra from simulations of JES0216 using 4<sup>th</sup> order diffusion coefficients of -0.002 (solid) and -0.004 (dashed).

conclude that numerical diffusion, both implicit and explicit, is the responsible for the fall off in variability at small scales.

Evidently, the numerical diffusion scheme will affect the physical representation of perturbations on the smallest resolvable scales. To test this diffusion and resolvability issue for the JES0216 case, we performed two COAMPS<sup>TM</sup> simulations for case JES0216 with different 4<sup>th</sup> order diffusion coefficients (0.002 and 0.004). A spectral analysis was then done for the simulated vertical velocity field. The energy density spectra along observation leg R02 (see Figure 4.7) for the two simulations are shown in Figure 4.12. The spectra show the separation between physical and computational solutions in the vertical velocity spectra referred to in Bryan et al. (2003). We find that the spectra for both runs are comparable to each other at scales between 3 km and 15 km. Below 3 km ( $6\Delta x$ ), the magnitude of the spectra decreases sharply from the observations. We conclude that, for the JES0216 model simulation, we cannot expect to fully resolve perturbations less than 3 km within the high-resolution ( $\Delta x = 500$  m) inner grid. Thus, while the model can theoretically resolve a 1 km ( $2\Delta x$ ) wave in the inner grid, all perturbations at or below the 3 km scale will be damped to some degree, if not completely, by the diffusion scheme and cannot be well represented in our results. In the COAMPS<sup>TM</sup> simulated results presented in the remainder of this chapter, a 4<sup>th</sup> order diffusion coefficient of 0.002 was used. This simulation will be referred to as the control run.

Another numerical issue worthy of discussion is the advection effect from the outer to the inner domains. Since the mean wind direction is from the northwest in JES0216, the effect of the model physics, within the innermost, highest resolution domain (i.e., smaller explicit and numerical diffusion), are not completely seen in the model output in the northwestern region of this small domain ( $10,000 \text{ km}^2$  in size), especially near the upwind boundaries. As a result, the model fields for the northwestern region of the domain show spatial variability similar to the corresponding geographic region in domain 3. As features advect into the relatively small inner domain from its parent domain, the model physics at higher resolution will have more noticeable effect as the down-wind distance increases and the spatial variation of the fields gets closer to the

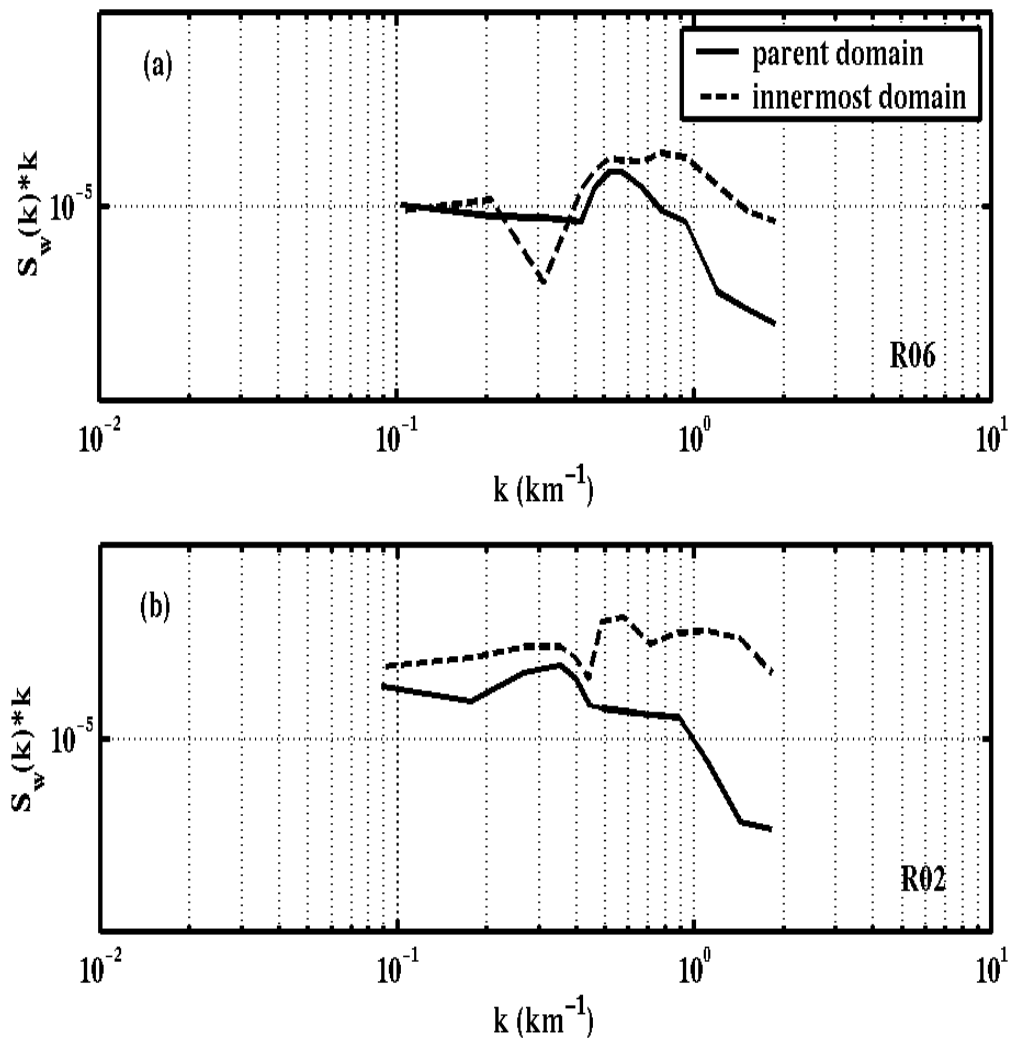


**Figure 4.13.** Energy density spectra COAMPS<sup>TM</sup> vertical velocity at 40 m above sea level for the parent domain (solid) and the innermost domain (dashed) from the simulation of JES0216 in both (a) northern (along flight leg R06) and (b) southern (along flight leg R02) geographic regions within the innermost domain. See Figure 4.7 for the locations of the flight legs.

true resolvability of the higher grid resolution. To illustrate this concept for the mean fields, a comparison between the innermost domain and its parent domain (domain 3 in Table 4.1) of the spectra in the BL (at 400 m above sea level) for the w wind component is shown in Figure 4.13. The spectra for each of the domains are calculated from model output along west to east lines for R02 (southernmost flight leg) and R06 (northernmost flight leg, see Figure 4.7) It is clear from the figure that the spectral energy in the resolvable scales (scale (wave number) greater than 3 km ( $2 \text{ km}^{-1}$ ) for the inner-most domain and 10 km ( $0.6 \text{ km}^{-1}$ ) for the parent domain) is similar for both domains in the northern region of domain 4, and increases with distance north to south for each domain. However, the increase in spectral energy for the innermost domain from north to south, nearly one order of magnitude, is clearly larger than for the parent domain. This illustration of the down-wind effect of the higher resolution model physics on the spatial variability within a given domain will be important in chapter V, when comparisons are made between two different simulations with different SGS mixing lengths.

## **2. Analysis of COAMPS<sup>TM</sup> Results from the Control Run**

### ***a. BL Development***

We will now determine the extent to which COAMPS<sup>TM</sup> represents the BL structure and features typical of CAO conditions. Figure 4.14 shows the COAMPS<sup>TM</sup> near-surface wind and temperature fields within the 13.5 km resolution outer domain, depicting conditions that exist within the innermost domain. The surface wind and surface air temperatures over the geographic region of the innermost domain (outlined in Figure 4.14) are from the northwest with magnitudes up to 30 kts ( $15 \text{ m s}^{-1}$ ) and between 261 and 263 K, respectively. The temperature gradient over most of the JES is relatively perpendicular to the wind direction. The effects of topography on the wind magnitude are evident, where a region of weaker wind within the innermost domain is present downstream of the coastal mountains.

Horizontal and vertical cross-sections of wind speed, vertical velocity, potential temperature, and moisture are shown in Figures 4.15 and 4.16. The horizontal cross-sections for the entire innermost domain region are shown for a height of 390 m (near the middle of the BL). The vertical cross section is taken along the line shown in

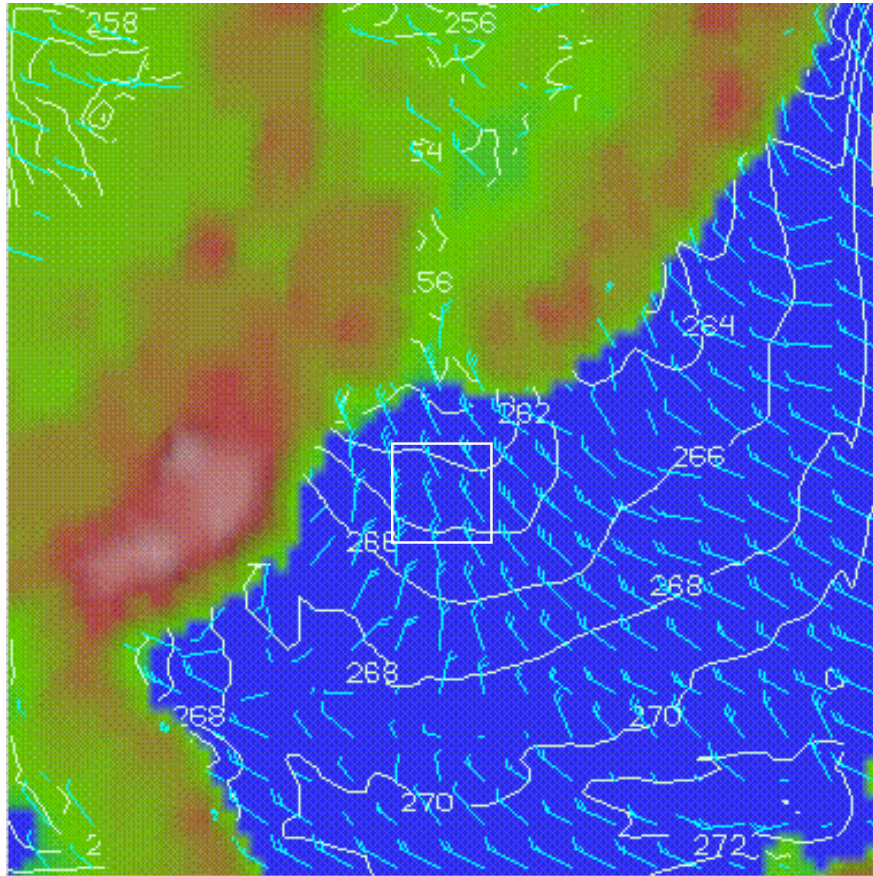


**Figure 4.14.** COAMPS 12.5 km resolution domain forecast fields, Valid 17 Feb 2000, 0000Z. The figure shows the wind speed in kts (barbs) and potential temperature in K at 40 m above sea level.

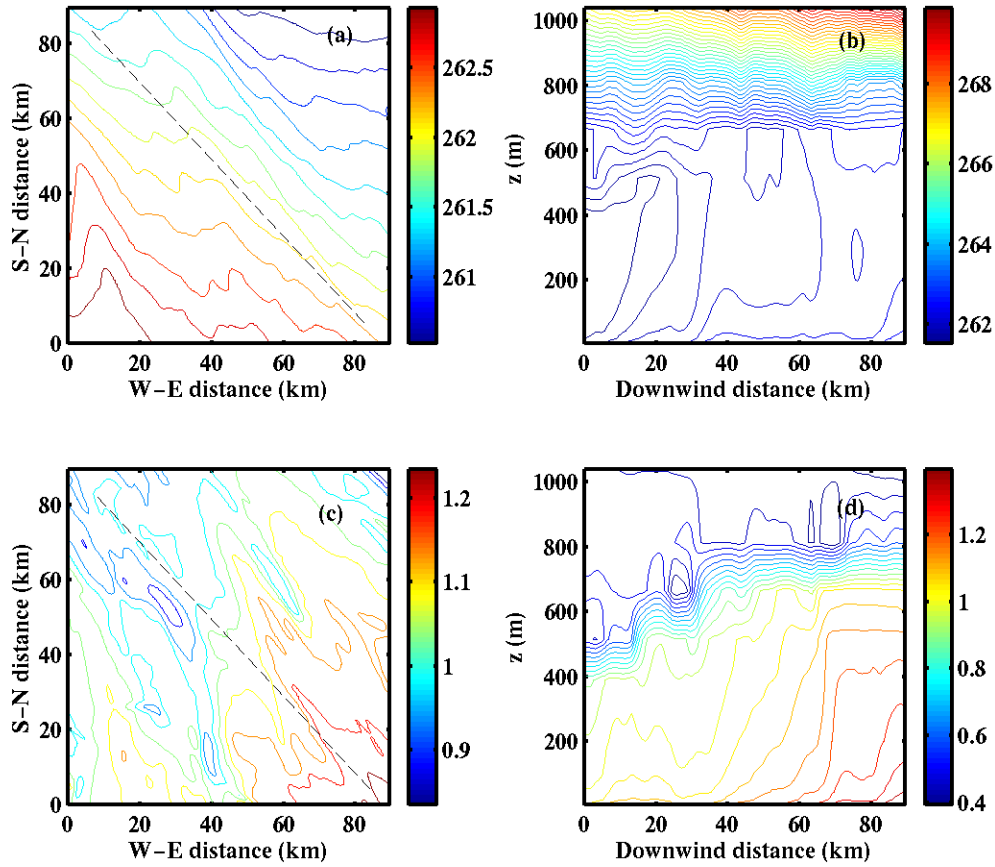


**Figure 4.15.** COAMPS<sup>TM</sup> JES0216 simulated fields, Valid 17 Feb 2000, 0000Z. Horizontal cross-sections at 390 m above sea level and vertical cross-sections along the line shown in the horizontal cross-sections for potential temperature (a and b) and water vapor (c and d). Contour intervals are 0.2 K for potential temperature and 0.05 g kg<sup>-1</sup> for water vapor.

the horizontal cross-sections, in the down-wind direction (viewing the plot from left to right), and from the surface to above the BL. To avoid erroneous data near the domain boundaries, the plot begins and ends 10 grid points (5 km) in from the boundaries. Figure 4.15a show small spatial variation in potential temperature that resembles that of the SST variation in the region, indicating the strong surface forcing in this case. The winter boundary layer over the simulated region is generally dry, with the specific humidity varying around  $1 \text{ g kg}^{-1}$ . However, downstream moistening is evident from both the horizontal cross-section (Figure 4.15c) and the downwind vertical cross-section (Figure 4.15d). From the vertical cross-section of potential temperature (Figure 4.15b), we can also identify the downwind development of the boundary layer as the air column moved over the JES. Here, the boundary layer growth was significant in the first 40 km of the vertical cross-section. There was also rapid warming as the BL grew. The BL height stabilized at around 700 m above sea level beyond the first 40 km where the BL became better mixed vertically in both potential temperature and water vapor. This simulated BL height is lower than the observation from the aircraft soundings (above 900 m), likely the result of an under-predicted BL air temperature. Compared to the aircraft observations, the BL potential temperature was in general under-predicted by COAMPS<sup>TM</sup> by 1 to 1.5 K. COAMPS<sup>TM</sup> generally has a cold bias recognized by NRL scientists (Dr. James Doyle, NRL Monterey, personal communication). Unfortunately, the source of this cold bias is not known yet. The simulated BL water vapor is consistent with the observed amount. We also note that while some thin clouds are seen in the satellite imagery of Figure 4.5 for this case, COAMPS<sup>TM</sup> did not produce any clouds in the control run.

The simulated wind speed in the down-wind direction at 390 m above sea level (Figure 4.16 a) shows a region of weaker wind with little spatial variability in the center of the grid, along the line of the vertical cross-section, and stronger winds with slightly more spatial variation in other regions. As shown in the outer domain wind field (Figure 4.14), the difference in wind speed magnitudes across the domain are likely due to the topographic effects of the nearby coastal mountains and valleys to the west. The simulated mean BL wind speed magnitude along the center/down-wind region of the

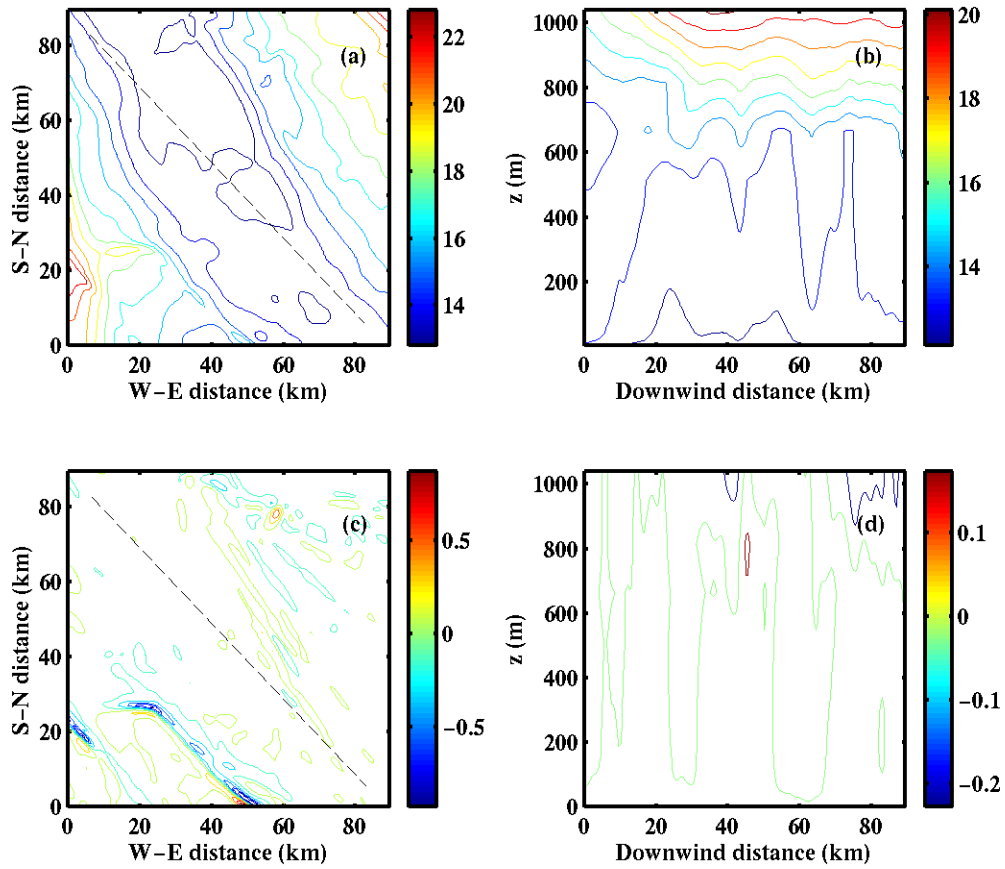


**Figure 4.16.** Same as in Figure 4.15, except for wind speed (a and b) and vertical velocity (c and d). Contour intervals are  $1 \text{ ms}^{-1}$  for wind speed and  $0.1 \text{ ms}^{-1}$  for vertical velocity.

domain is around  $14 \text{ m s}^{-1}$ , comparable to the near-surface aircraft observations (see Figure 4.9). However, the increase in wind speed magnitudes in the southwest and northeast corners of the domain is not as large in the observations and thus are over-predicted by the model. In addition, more horizontal spatial variability in the simulated wind speed is expected in the resolvable scales, since the wind speed variations in the aircraft observations in Figure 4.9 are on the scale of 4 to 10 km. In the vertical cross-section (Figure 4.16 b) there is indeed little variation along the down-wind direction through the depth of the BL, but significant wind shear is seen above the inversion, with an evident inflection point at around 1 km above sea level. Unfortunately, the wind speed increase above the BL cannot be verified since there were no observations above the BL.

The simulated vertical velocity cross-sections (Figure 4.16 c and d) should indicate the BL updraft and downdraft regions on the resolvable scale. While the observations showed near-surface updrafts and downdrafts of up to  $1 \text{ m s}^{-1}$  in magnitude, the model predicts magnitudes along the cross-section within the surface layer, and most of the BL, of only  $0.2 \text{ m s}^{-1}$ . One noteworthy roll-like turbulent eddy structure is seen on the horizontal cross-section at 390 m above sea level in the southwest corner of the grid, with updraft/downdraft magnitudes comparable to those expected near the middle of a convective BL, and a width of around 5 km. Another more cellular-like eddy appears in the NE corner of the horizontal cross-section. Other than these isolated features, the simulated vertical velocity magnitudes overall are too weak, and we see again that the spatial variability of eddies is in general much less than in the observations.

Another notable feature in the vertical cross-section of vertical velocity is the presence of eddies above the BL inversion. These features are likely internal gravity waves, which, as discussed in Clark et al. (1986), Mason and Sykes (1982) and others, are features that exist in nature as well as being simulated in numerical models. These features are commonly seen in cases with a convective BL and strong vertical wind shear above the inversion. The waves are produced as thermally-forced eddies formed in the BL push up on the inversion and into the stable layer. These ripples then produce vertically-propagating gravity waves. The wind shear above the inversion also

contributes to the gravity wave production and propagation, as the differential air motions exist relative to the thermals. The shear is obstructed (known as “form drag”) by the BL eddies, and as the wind flows up and over eddies to uphold the continuity of mass, vertically propagating waves form. Thermal forcing is a pre-requisite for the production of internal gravity waves, while the shear facilitates the wave production and propagation. Mason and Sykes (1982) obtained numerical solutions without clouds where BL eddies were produced and coupled with internal gravity waves of distinct but small magnitude ( $0.4 \text{ m s}^{-1}$ ). Clark et al. (1986) simulated idealized cases of convective BLs where internal gravity waves were produced in the cases of moderate to strong shear, and describe the development of the gravity waves. Once the eddies produced in the simulation fill the BL, they become obstacles to the flow, causing the formation of the gravity waves, which are launched vertically up and over the BL thermals into the stable layer. The eddies propagate both horizontally and vertically away from their origin, increasing in both horizontal and vertical scale. While this is all very interesting, we will conclude by acknowledging the realistic existence of these features as cited and discussed in the literature and move on. Again, the existence of the simulated internal gravity waves is however not verified for our case, since we have no observations above the BL.

#### ***b. Surface Fluxes***

While we will save more detailed descriptions of the parameterized turbulent fields (fluxes and TKE) for next chapter, we will briefly discuss the model surface fluxes (Figure 4.17) in comparison to observation. The heat and momentum fluxes show a region of relatively weaker fluxes in the center of the domain, along the diagonal in the down-wind direction, which corresponds to the region of relatively weaker (but comparable to observations) and relatively homogenous simulated horizontal winds. The combined sensible and latent heat fluxes are comparable to observations in the center/down-wind region, and clearly overestimated in the regions of over-predicted winds in the northeast and southwest. Also, because the comparison here is between bulk flux method parameterized surface fluxes and the observed fluxes at 40 m above sea level, we do expect some differences between the observed and simulated surface fluxes. There is better horizontal spatial variability in the fluxes in the southeastern region of the

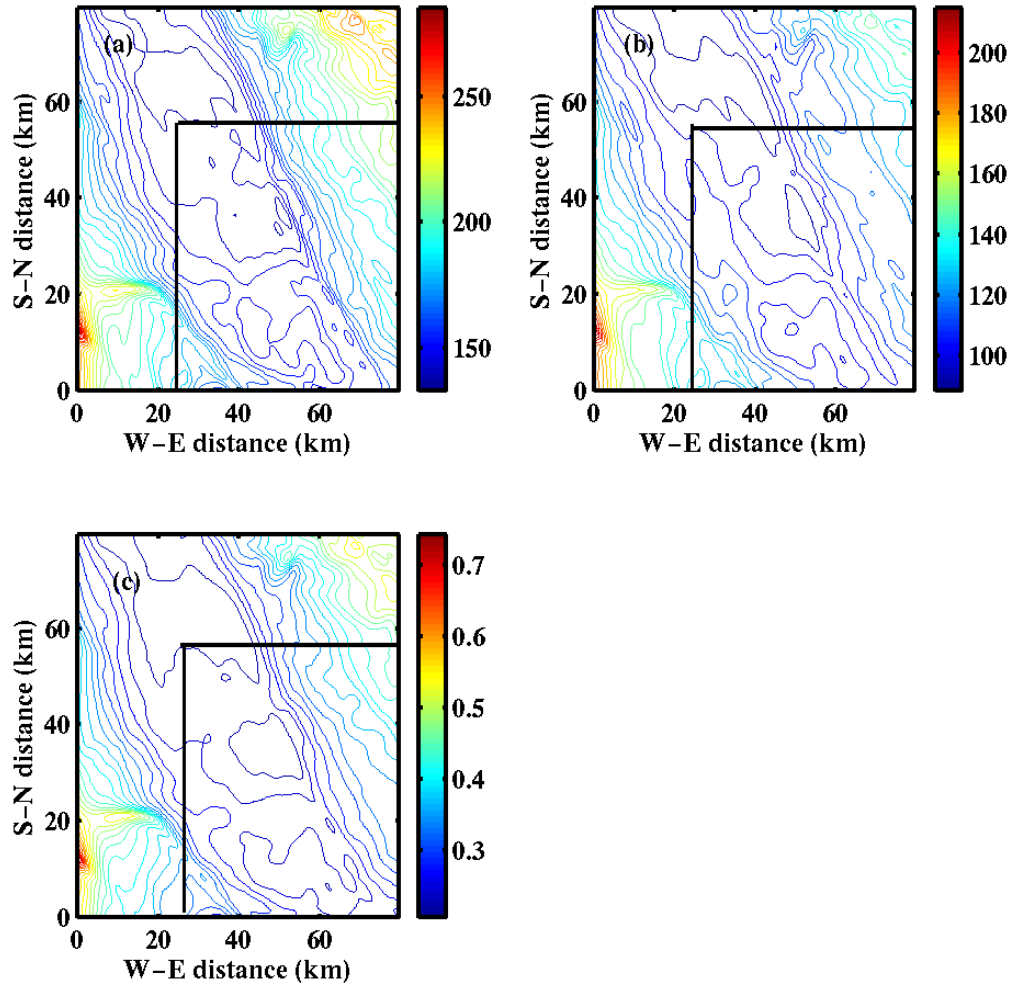


**Figure 4.17.** Horizontal cross sections from JES0216 control run, valid 17 Feb 2000, 0000Z for (a) surface sensible and (b) surface latent heat fluxes ( $\text{W m}^{-2}$ ), and (c) surface wind stress ( $\text{N m}^{-2}$ ). Contour intervals are 5  $\text{W m}^{-2}$  for sensible and latent and 0.02  $\text{N m}^{-2}$  for wind stress.

domain (outlined in each of cross-sections in Figure 4.14), which was not as evident in the cross-sections of the simulated mean fields. This is due to the affect of advection from the 1.5 km resolution parent domain into the 500 m resolution innermost domain, with the model physics improving the spatial resolvability down-wind, as discussed earlier. More issues will be raised and closer model-observations comparisons will be made using the SGS BL turbulent fluxes in the next chapter.

We also calculate the  $z_i/L$  from the simulated surface sensible heat flux,  $u^*$ , BL height and potential temperature. The mean  $z_i/L$  for the domain 4 region is calculated as  $-5$ , which is comparable to the calculation made from the observations and thus also predicts a regime where convective rolls would develop.

## **F. SUMMARY AND CONCLUSIONS**

In this chapter, we described the JES0216 case study. Global model analysis fields showed a persistent synoptic situation in the region of interest in the western JES (post-cold frontal, CAO conditions with strong subsidence) between 16 February 1200 Z and 17 February 0000 Z. Satellite imagery and aircraft observations illustrated the presence of convective roll vortices in the location of the high-resolution inner domain of our control run simulation. The value of  $z_i/L$  calculated from the aircraft observations was  $-4.6$ , which falls within the  $z_i/L$  range given in the literature for convective roll development. The aircraft observations also indicated large air-sea temperature differences coupled with relatively high near-surface winds. The combined effects generated large surface heat fluxes, which drove the development of the rolls. The scale of the rolls, based on mean field perturbations in the near-surface aircraft observations was around 3 to 5 km.

A COAMPS<sup>TM</sup> control run simulation for the JES0216 case was performed. In-depth analysis of the model output fields showed that that the model is adequately representing the mean state of the BL for this post-frontal, CAO case. The control run showed good comparison to observations in terms of magnitudes of the mean fields and surface heat fluxes. The control run realistically simulated development of the BL in the down-wind direction, becoming warmer and moistening with distance off-shore.

However, the control run failed to simulate the convective roll vortices. Simulated vertical velocities were too weak, and there was an overall lack of horizontal spatial variability in the simulated mean fields compared to the observations. In light of the discussion on the explicit and numerical effects of diffusion and advection on the simulation, the results indicate that the BL structure on the true resolvable scale ( $> 3$  km) is not well represented by the model. Therefore, adjustments will be made within COAMPS<sup>TM</sup> in an attempt to improve the simulation of the resolvable scale features. The method, objective and rationale for this adjustment, and the results of the simulation using the modified COAMPS<sup>TM</sup> code, will be discussed in chapter V.

THIS PAGE INTENTIONALLY LEFT BLANK

## V. COAMPS<sup>TM</sup> CASE STUDY SIMULATION USING A RESOLUTION-DEPENDENT TURBULENCE PARAMETERIZATION

### A. MODIFICATION TO COAMPS<sup>TM</sup> MIXING LENGTH

#### 1. Rationale and Motivation

It is apparent from the results in chapter IV that, based on the known limits of resolvability in the COAMPS<sup>TM</sup> model, the highest resolution domain should be resolving a greater degree of variability. Our proposed theory to explain the lack of variation in the model results for the JES0216 control run is that the model mixing length, used in the turbulent parameterization calculations, is too large. Based on the use of mixing length in the SGS parameterization of the vertical fluxes, with the turbulent mixing length too large, the vertical mixing that occurs with each time step in the model would generate too much mixing of properties in the BL, and thus likely underestimates the spatial variability on the true resolvable scale ( $6\Delta x$ ).

Recall from the length scale analysis in chapter III that, for a horizontal grid spacing that falls below the scale of large turbulent eddies (as is in the JES0216 simulation with a  $\Delta x$  of 500 m) the integral length scale profile should be smaller in magnitude than that calculated by an ensemble turbulence parameterization scheme (see Figure 3.9). The smaller length scale would more correctly represent the turbulent eddies that scale at and below the technical resolvability ( $2\Delta x$ ) of the domain. It can be hypothesized, based on the reference by Chou and Zimmerman (1989) to the dependence of the mesoscale roll vortices on the large scale turbulent eddies, that improved simulation of the large-scale turbulence could also improve the simulation of the mesoscale convective rolls.

This chapter will discuss the changes made to the mixing length calculation in COAMPS<sup>TM</sup> in an effort to improve the horizontal spatial variability of the high-resolution output to be more realistic, and compare the modified mixing length simulated output to the JES0216 control run simulation and to observations to see if improvement is indeed made. Based on the results of our control simulation of the JES0216 case, we will

apply an attempted improvement to the COAMPS<sup>TM</sup> SGS parameterization in the high-resolution innermost domain, in an effort to better simulate the true spatial variability of the atmosphere in high-resolution output.

## 2. Modified Mixing Length Formulation for COAMPS<sup>TM</sup>

Based on our study in previous chapters, we introduce a resolution-dependent mixing length ( $l_{\Delta x}$ ) formulation into COAMPS<sup>TM</sup> with modifications suitable for the model. This new formulation (applied only within the high resolution nest of our simulation) adjusts the original COAMPS<sup>TM</sup> ensemble turbulence parameterization mixing length calculated using the MY82 vertically integrated TKE formulation, to a magnitude and profile appropriate for the resolution of the simulation. The equation used to adjust the mixing length is based on equation 3.3, but adjusted for COAMPS<sup>TM</sup>. Here, the integral scale accounting for all scales of turbulence ( $\Lambda_{ENS}$  in equation 3.3) is replaced with the mixing length as originally calculated in COAMPS<sup>TM</sup> using the MY82 formulation ( $l_{MY82}$ ), and the integral scale accounting for the smallest scales considered ( $\Lambda_{200m}$  in equation 3.3) is taken as a constant value,  $l_{LES}$ , of 37.5 m. Therefore, equation 3.3 becomes, for our numerical adjustments,

$$\frac{1}{l_{\Delta x}} = \frac{1 - e^{-R\Delta x}}{l_{MY82}} + \frac{e^{-R\Delta x}}{l_{LES}}, \quad (5.1)$$

with R equal to 3.8 when  $\Delta x$  is in km, as in equation 3.3. As  $R\Delta x$  becomes large, equation 5.1 approaches  $l_{MY82}$ , where all turbulence scales below  $2\Delta x$  and should be entirely accounted for in the parameterization. As  $\Delta x$  approaches LES resolution (i.e.,  $\Delta x \sim O(100 \text{ m})$ ), equation 5.1 approaches  $l_{LES}$ , which would be appropriate for parameterization of eddies in the inertial sub-range and below. Thus, this modified equation allows for a smooth transition from a mixing length appropriate for total ensemble parameterization at larger  $\Delta x$ , to one appropriate for an LES-type parameterization at small  $\Delta x$ .

Equation 5.1 was applied in a simulation of JES0216, where the simulation is identical to that presented in chapter IV, except for the modification to the mixing length. We will refer to the modified simulation as RESDEP, for the resolution-dependent

mixing length modification. The modified mixing length at the 12-hour forecast time is shown in Figures 5.1 and 5.2. Here, Figure 5.1 shows the domain-averaged mixing length profile. The magnitude of the resolution-dependent mixing length is seen to decrease in magnitude from that of the control run by about one-half. Based on the results of the observational study of integral scales in chapter III, the magnitude decrease and shape of the profile is appropriate for parameterization of 1 km eddies and smaller. The horizontal cross-section of mixing length at 390 m above sea level is shown in Figure 5.2. This level is near the middle of the BL where the magnitude of mixing length is generally largest, as seen from Figure 5.1. From Figure 5.2, we see the general decrease in the magnitude shown in Figure 5.1. The steeper slope of the NOMOD mixing length profile ( $l_{MY82}$ ) near 390 m generates more variation of the mixing length in the horizontal cross-section across the domain at this level. Because the mixing length formulations are sensitive to the vertically integrated TKE (Equation 2.21), the horizontal distribution of the mixing length is also dependent on the distribution of TKE in the BL, which is driven by the surface forcing (total heat flux for JES0216).

Next we will examine the extent to which this new resolution-dependent mixing length formulation affects the simulation of the BL structure for JES0216. Recall from chapter IV that the  $z_i/L$  of  $-5$ , calculated from both observations and the NOMOD simulation, suggested the possible formation of horizontal roll vortices within the BL for JES0216. Indeed the roll vortices were observed at 5 km spacing. From our test simulations on model numerics effects, COAMPS<sup>TM</sup>, at 500 m resolution, should be able to resolve these roll structures. Unfortunately, the rolls were not simulated well in the NOMOD simulation. It is hoped that the modification to the mixing length in the RESDEP simulation will improve the simulated structure of the convective rolls. We will analyze and compare the control and modified simulations from two aspects: the differences in the resolvable scale structure of the BL, in terms of both magnitude and spatial variability of the mean quantities, and the differences in the magnitude and structure of the SGS parameterized fluxes and TKE.

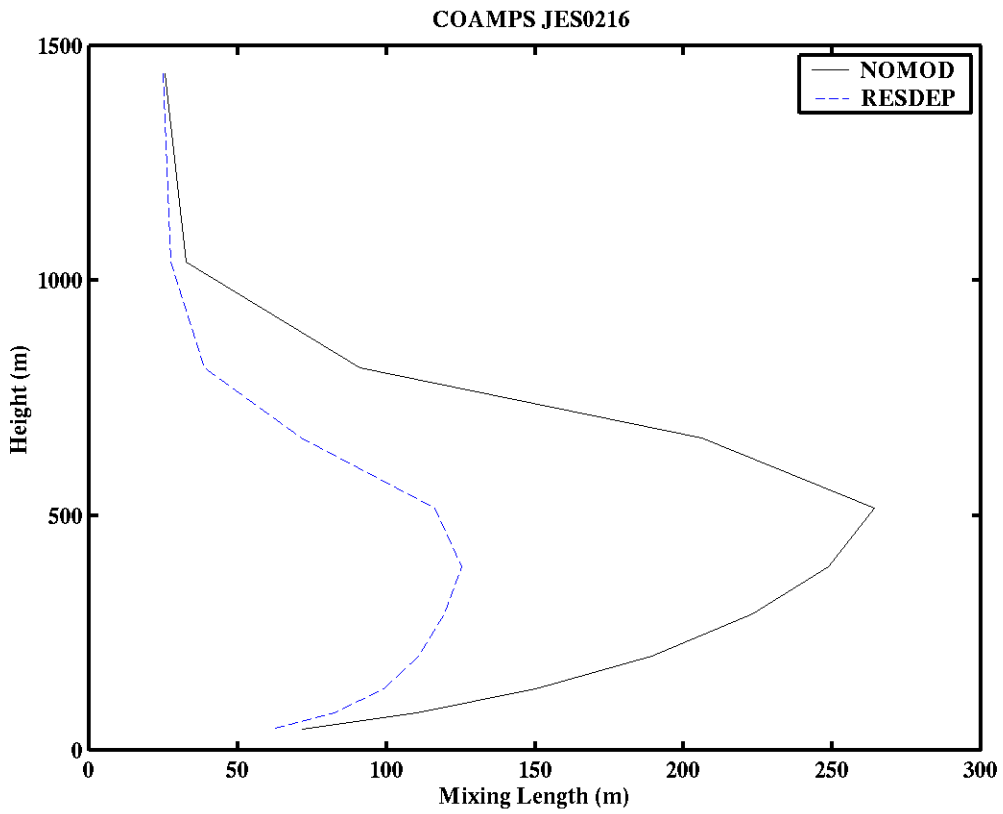
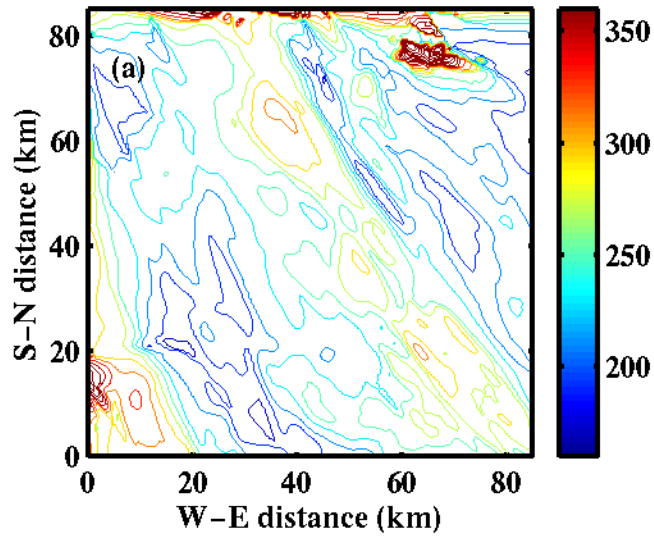


**Figure 5.1.** COAMPS<sup>TM</sup> domain-averaged profiles of mixing length (m) from NOMOD (solid) and from the resolution-dependent formulation from RESDEP (dashed) for JES0216. Data shown is from the 12-hour forecast fields, valid 17 Feb 2000, 0000Z.

COAMPS JES0216

NOMOD



RESDEP

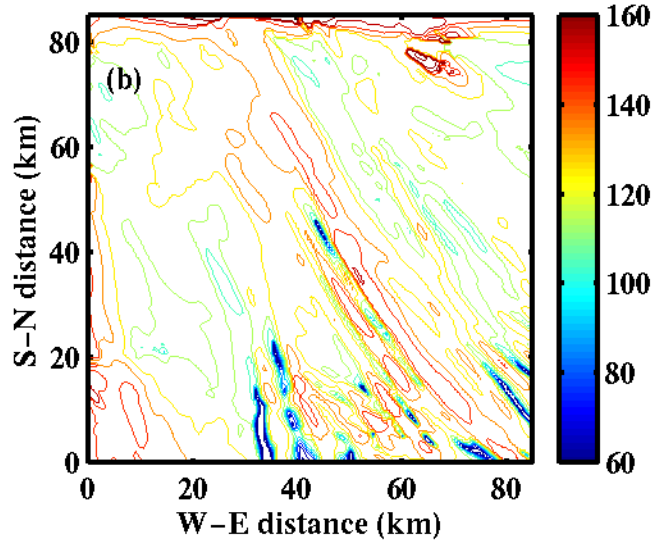


**Figure 5.2.** Same as in Figure 5.1, except horizontal cross-sections for the entire domain at 390 m above sea level, for NOMOD (a) and RESDEP (b) simulations.

## **B. EFFECTS OF MODIFIED MIXING LENGTH ON SIMULATING THE ROLL STRUCTURE**

### **1. Boundary Layer Mean Structure**

In the following comparisons of the mean quantities (horizontal wind, temperature, and water vapor), we will focus on the southeastern region of the domain, where the spatial variability is considered to be representative of the 500 m resolution (due to advection affect from the parent nest, as discussed in chapter IV). This region is defined, from inspection of the spatial variability of the SGS fluxes from the control run, by the region outlined within the high-resolution domain in Figure 4.17. Unless otherwise noted, the horizontal boundaries of the horizontal and vertical cross-sections presented in this chapter are defined by this region of the domain. In addition, the vertical cross-sections are now taken along a West-to-East line at the southern end of this region instead of a line in the downwind direction as was done for the vertical cross-sections presented in chapter IV.

In the comparison between the horizontal and vertical cross-sections of the mean quantities between NOMOD and RESDEP in Figures 5.3 to 5.6, it is immediately apparent that the horizontal spatial variability is increased in RESDEP. In the horizontal cross-sections, a clear signature of the observed roll structure is now simulated in all of the mean quantities, as represented by the longitudinal alignment of small-scale features in the horizontal wind, temperature, and moisture with the mean wind direction (from NW to SE), which were not present in the NOMOD simulation. The signature of the rolls is clearest in the water vapor and vertical velocity fields. From the horizontal cross-sections of water vapor and vertical velocity from RESDEP (Figures 5.5 c and 5.6 c), the scale of the rolls (the measured distance across adjacent moist updraft and drier downdraft features) vary between 3 and 7 km, which is fairly consistent with the scale of the rolls determined from the aircraft observations. The BL height and structure of the inversion in RESDEP is very similar to that of NOMOD, clearly seen in the vertical cross-sections of potential temperature (Figure 5.4 b and d). Using a

COAMPS JES0216 Wind Speed

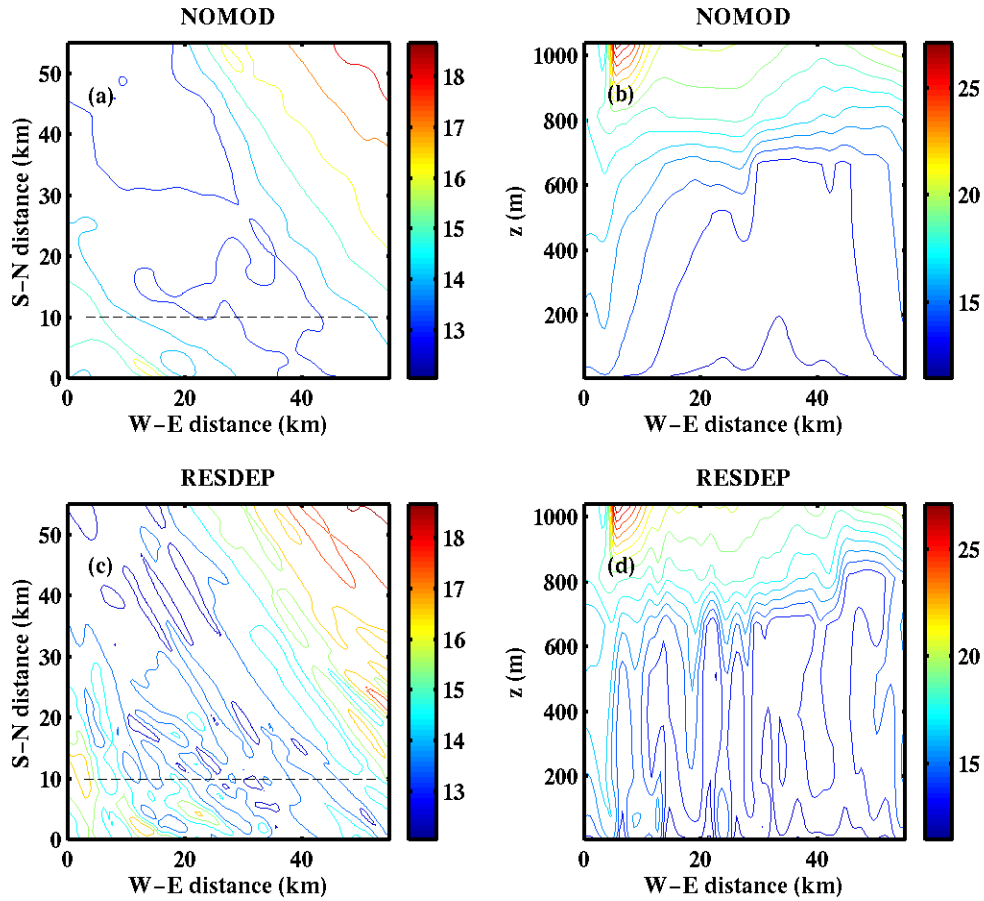


**Figure 5.3.** Comparisons of simulated wind fields between NOMOD and RESDEP. Horizontal cross-sections and W-E vertical cross-sections of the horizontal wind ( $\text{m s}^{-1}$ ) for NOMOD (a and b) and RESDEP (c and d). Area shown in horizontal cross-sections (a and c) is the southeastern region ( $\sim 60 \times 60 \text{ km}^2$ ) of the domain. Vertical cross-sections (b and d) are along the line shown in the horizontal cross-sections. Contour interval is  $1 \text{ m s}^{-1}$  for all plots.

COAMPS JES0216 Potential Temperature

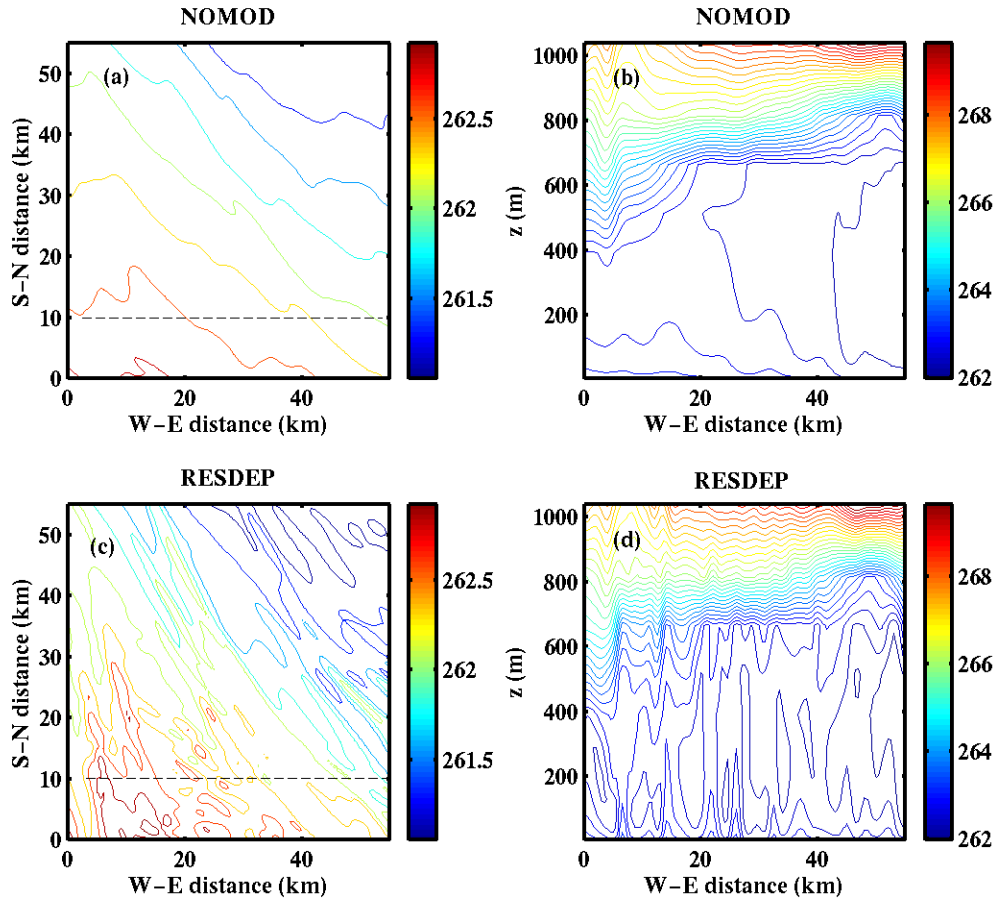


**Figure 5.4.** Same as in Figure 5.3, except for potential temperature (K). Contour interval is 0.25 for all plots.

COAMPS JES0216 Water Vapor

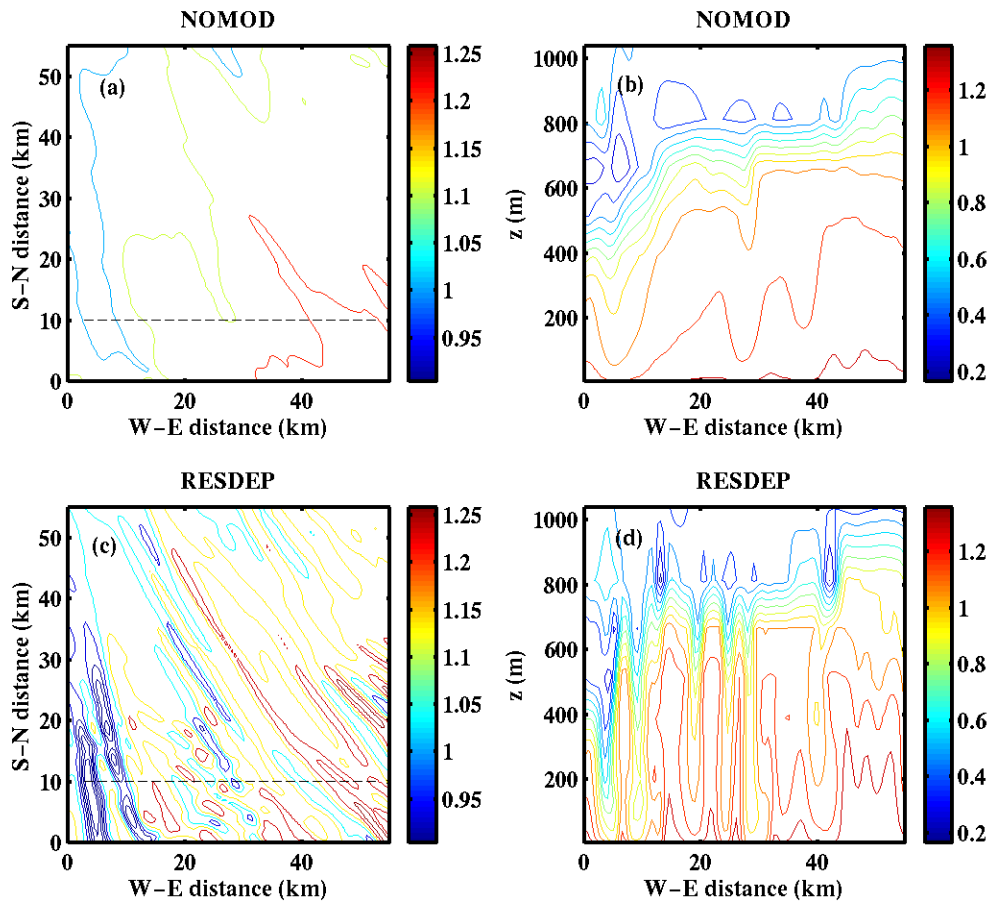


**Figure 5.5.** Same as Figure 5.3, except for water vapor ( $\text{g kg}^{-1}$ ). Contour interval is 0.1 for all plots.

COAMPS JES0216 Vertical Velocity

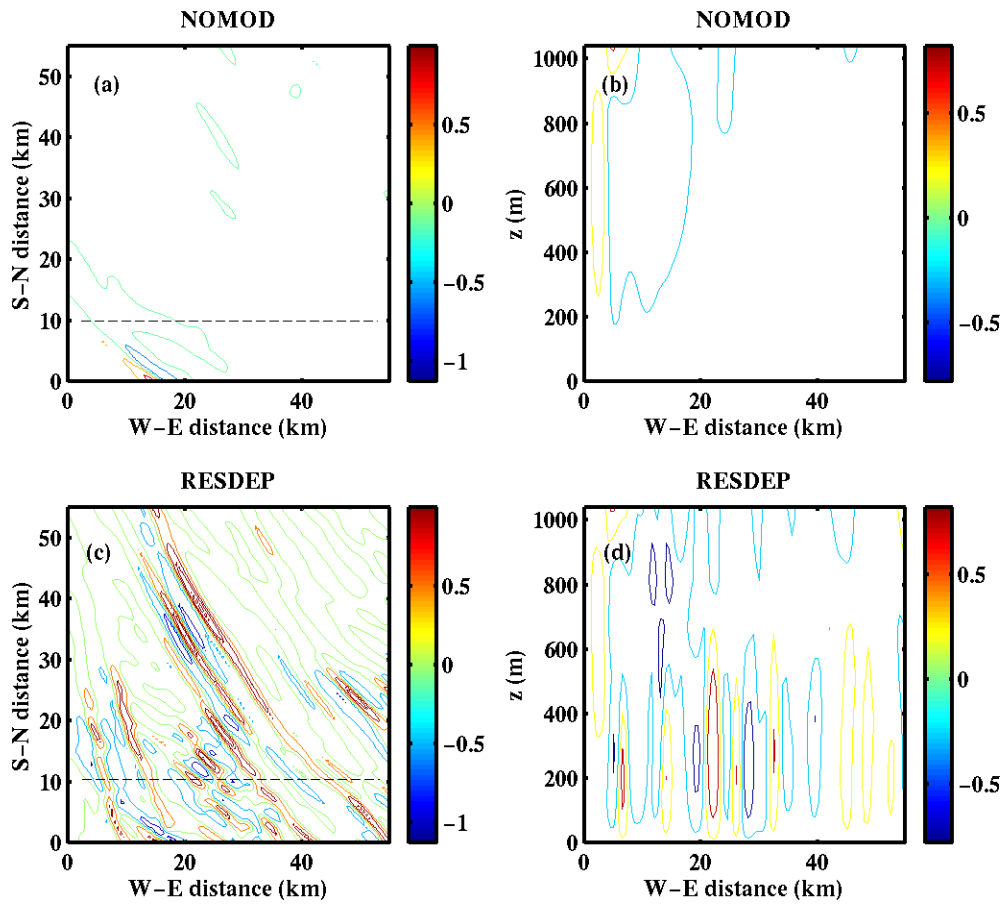


**Figure 5.6.** Same as in Figure 5.3, except for vertical velocity ( $\text{m s}^{-1}$ ). Contour interval is 0.5 for all plots.

mean BL height of this cross-section (around 600 m), the aspect ratio of the rolls is 5 to 11.6, which is somewhat larger (due to the lower than observed simulated BL depth) than the 4 to 6 range of aspect ratio calculated from the observations in chapter IV, but is within the range for a BL containing roll vortices (Etling and Brown 1993). In Figure 5.6, the differences in eddy structure modeled by the two simulations are evident. In the NOMOD run, the only roll updraft and downdraft events were simulated on the western end of the cross-section, with weak resolvable scale vertical motion for the rest of the cross-section. In contrast, the RESDEP simulation shows considerable updrafts/downdrafts throughout the cross-section, which clearly defines the role structure of the BL. Furthermore, the RESDEP results show narrower updraft cores and broader downdraft regions being realistically simulated. The vertical cross-sections for the different mean quantities are cutting through the rolls at about a 45 degree angle, and together they show the simulated BL roll structure clearly, with the warm, moist eddies corresponding to updraft cores, and cooler, drier eddies corresponding to the downdraft cores. The simulated magnitude of roll updrafts/downdrafts in RESDEP is also larger and more realistic, with the maximum updraft core reaching  $1.3 \text{ m s}^{-1}$ , twice that of the NOMOD simulation.

To further determine if the spatial variability and magnitudes of the mean fields simulated in RESDEP is realistic, we directly compare the simulated fields to aircraft observations. Due to the relative lack of spatial coverage of the observations for JES0216, our model-observation validation is limited only to near the surface and to profiles within the BL. The simulated mean quantities are compared to the JES sounding observations in Figures 5.7 and 5.8. The sounding used for comparison in this figure is S7, whose location within the domain is shown in Figure 4.7. Because the aircraft travels 8 to 10 km from SE to NW during the sounding, there is significant variability seen in the observed profiles of the horizontal wind components (Figure 5.7), and some, but less, variability in the observed water vapor and potential temperature profiles (Figure 5.8) as the aircraft passes through locally different air masses in the horizontal. This variability is not present in the simulated profile, which is made up of data from the corresponding vertical levels at the same horizontal grid point, located in the region of the S7

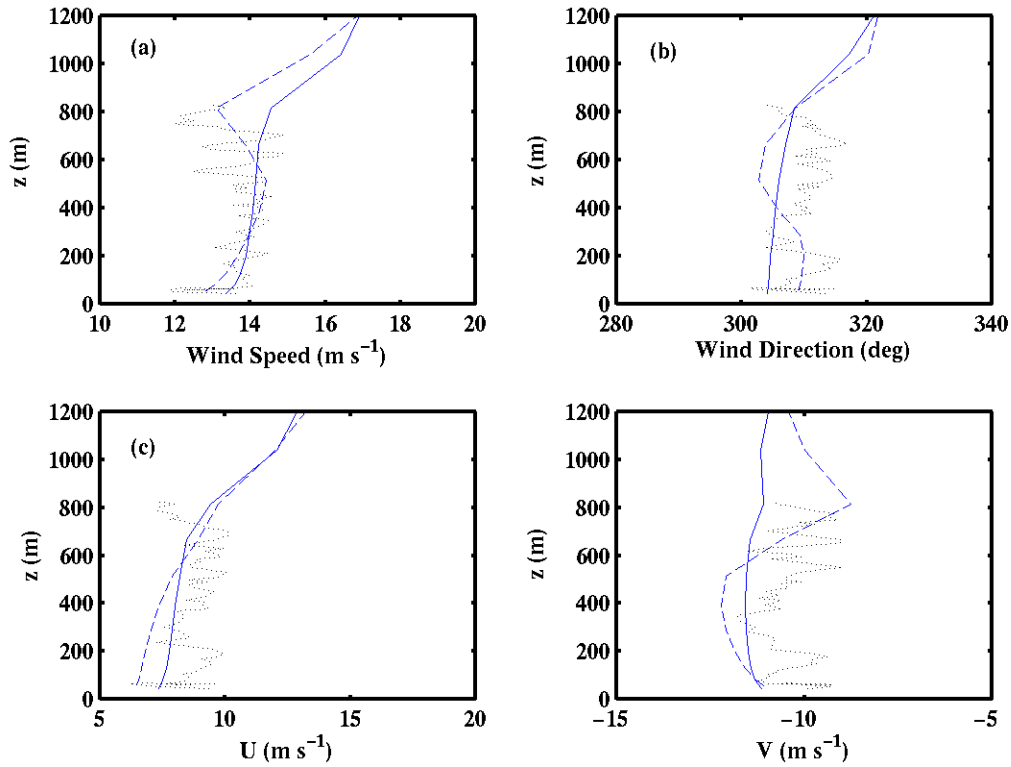


**Figure 5.7.** COAMPS vertical profiles of (a) wind speed, (b) wind direction, (c)  $U$  wind component, and (d)  $V$  wind component (units shown) for NOMOD (solid), RESDEP (dashed), and aircraft sounding observations taken near the location of the model vertical profiles (dotted).

JES0216

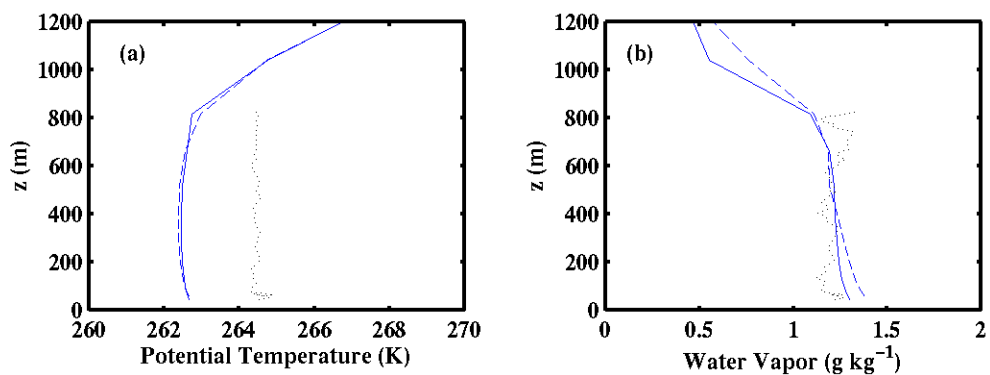


**Figure 5.8.** Same as Figure 5.7, except for potential temperature (a) and water vapor (b).

observations. We observe only small differences between the simulated profiles at this particular location in the domain, and in comparison to observations, there is fairly good agreement in both the trend with height and magnitudes for all quantities except the potential temperature, which is simulated between 1 and 2 degrees too cool, as already discussed in chapter IV. This is at least part of the reason for the lower than observed BL depth and smaller than observed roll aspect ratio. Significant wind shear in both magnitude and direction are seen above the BL inversion. The simulated profiles for RESDEP clearly show significant wind shear near the middle of the BL, with an inflection point at a height of about 530 m, and significant veering of the wind within the BL as well. This BL wind shear depicts the inflection point instability that, in conjunction with convective instability, enhances the development of convective rolls, as discussed in Etling and Brown (1993). The signature of the inflection point instability is not present in the NOMOD wind profiles. The wind shear above the inversion is present in both simulations, and enhances the internal gravity waves in the free atmosphere above the BL (discussed in chapter IV), visible in the vertical velocity vertical cross-sections (Figure 5.6 b and d) for both simulations. The observed and simulated BL wind profiles, which show very little wind shear within the BL, also indicate that the mechanism for the roll development is mainly convective instability vice inflection point instability (Etling and Brown 1993). Comparisons between BL profiles from NOMOD, RESDEP, and other aircraft soundings yield similar results to those shown in Figures 5.8 and 5.9.

## **2. Spectral Analysis of Resolvable Scale Mean Fields**

The horizontal variations of the mean quantities along the near-surface flight track R02, near the south end of the domain (see Figure 4.7) are compared in Figures 5.9a to 5.13a. Both NOMOD and RESDEP compare fairly well in magnitude with the observations for the wind components and water vapor, but the potential temperature is, again, simulated about 2 degrees too low in comparison to the near-surface observations, consistent with the profile of Figure 5.8. The simulated vertical velocity at the flight level is significantly weak in magnitude for both NOMOD and RESDEP, with more variation in RESDEP that is closer to that observed.

While the increase in horizontal variability is evident from the RESDEP simulation along the near-surface flight leg, the scales at which the variability increases is more clearly evident from the analysis of the energy density spectra, shown in Figures 5.9b to 5.13b for each of the mean quantities. The spectra can only illustrate the resolved scale variations above the resolvable limit of the model. In chapter IV, this resolvable limit was determined to be  $6\Delta x$ , or 3 km for our 500 m resolution domain. The spectra are plotted versus wave number, so the 3 km limit corresponds to a wave number of around  $2 \text{ km}^{-1}$ . At the largest scales (smallest wave numbers), the statistical significance of the spectra for both the model output and observations is limited by the length of the data for spectral analysis, which is about 60 km. Therefore, we focus our spectral comparison between the model and observations to within the scales of 3 to 12 km (wave numbers  $0.5$  to  $2 \text{ km}^{-1}$ ), where we consider the spectra to present the most accurate representation of the perturbation energy. Within this range, we observe that the NOMOD spectra energy for all three wind components, heat, and moisture, is one to three orders of magnitude smaller than that for RESDEP, while the RESDEP energy spectra compare to the observed spectra within one order of magnitude, with vertical velocity being the most underestimated (but most improved over NOMOD). All of the observed spectral quantities show a peak in energy at around 4 to 6 km, indicative of the presence of the convectively-driven roll vortices at that scale range (LeMone 1976). In general, the horizontal variations on the scale of the rolls in RESDEP are much more comparable with those from observations, although the comparisons in vertical velocity and water vapor are less ideal. This is a significant improvement from the control run with the original COAMPS<sup>TM</sup> length scale formulation.

We also calculated the co-spectra between vertical velocity and scalar variables such as potential temperature and water vapor to examine the resolvable scale flux transport (Figure 5.14). The aircraft observation shows sizable co-spectra between wave numbers  $0.8$  and  $2 \text{ km}^{-1}$ , suggesting flux contribution from the roll scale perturbation ( $\sim 3$  to  $8$  km wavelength). The RESDEP simulation reveals similar flux contribution by the rolls with some discrepancy in sensible heat flux (Figure 5.14a). In contrast, there is very little co-spectral energy at all resolvable scales in NOMOD. Overall, the resolvable

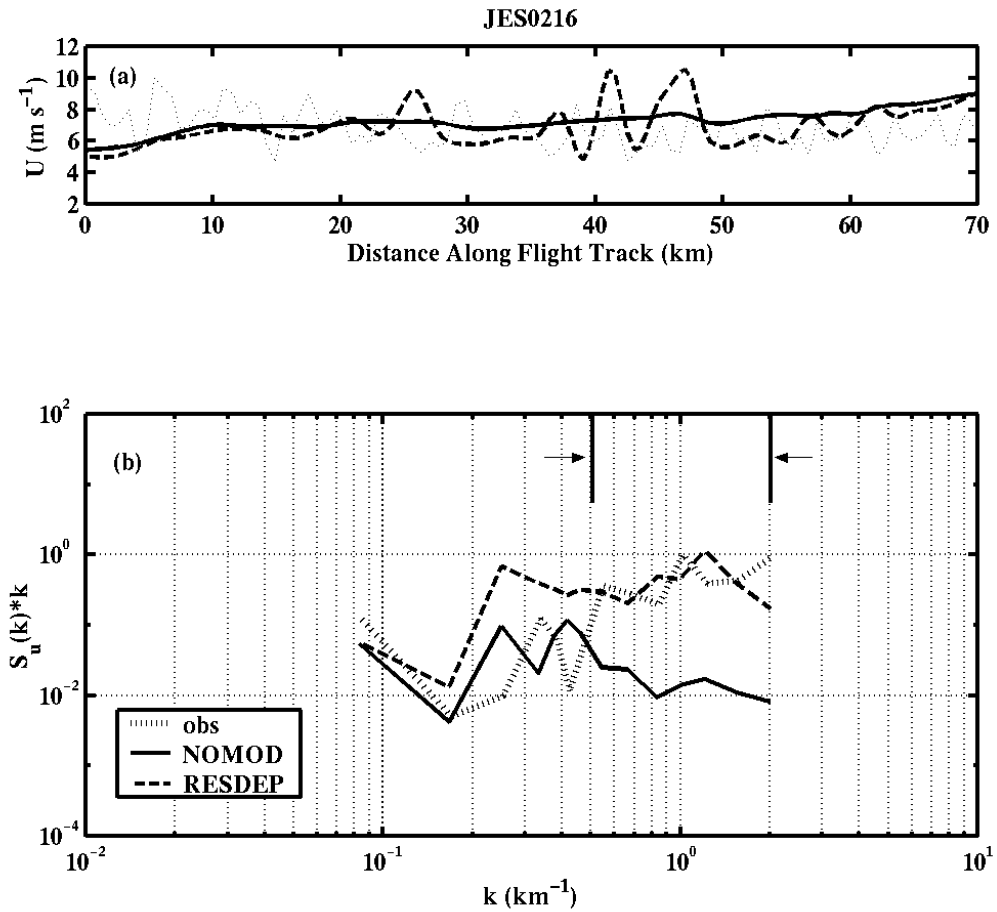


**Figure 5.9.** Comparison of the horizontal variability of the U wind component among aircraft observations (dotted), NOMOD (solid), and RESDEP (dash). All data were taken from the same horizontal path along R02 at 40 m above sea level. (a) Spatial series plot; (b) Energy density spectra. The spectra are cutoff at  $2 \text{ km}^{-1}$  in wave number ( $k$ ) corresponding to a wavelength of  $\sim 3 \text{ km}$ . The two short vertical bars denote the range over which the spectral analysis are statistically significant (see discussions in text).

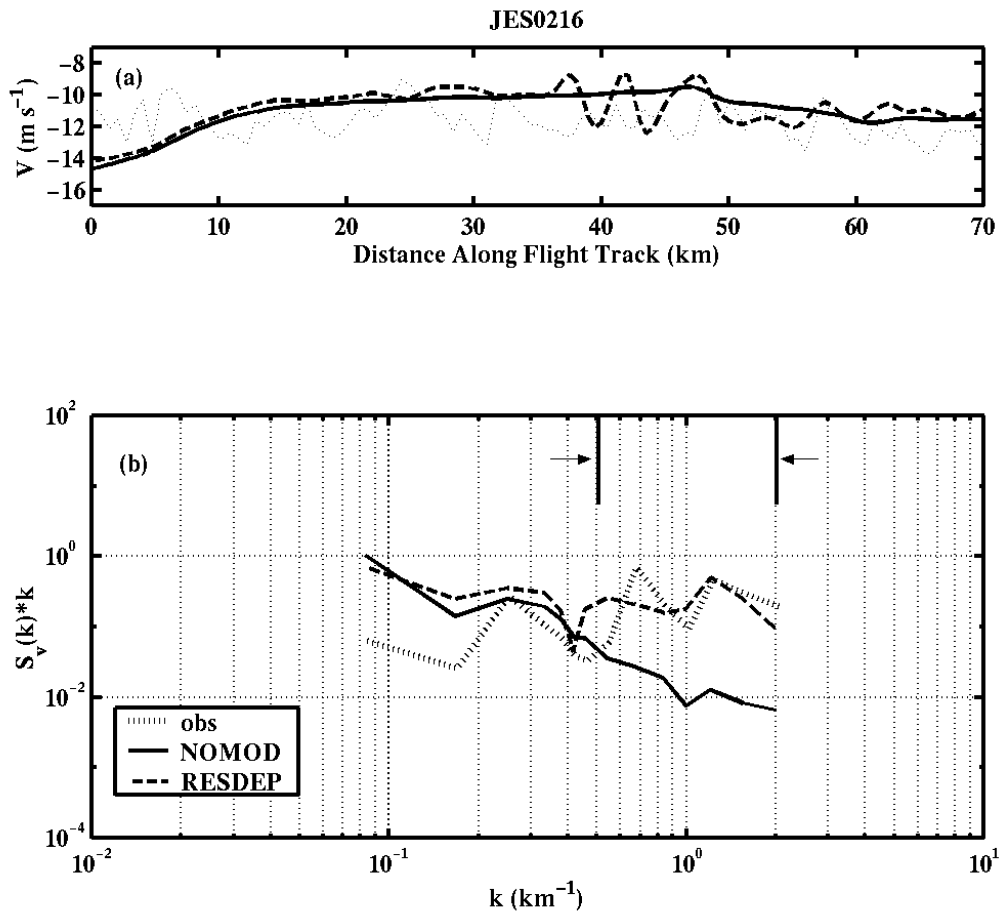
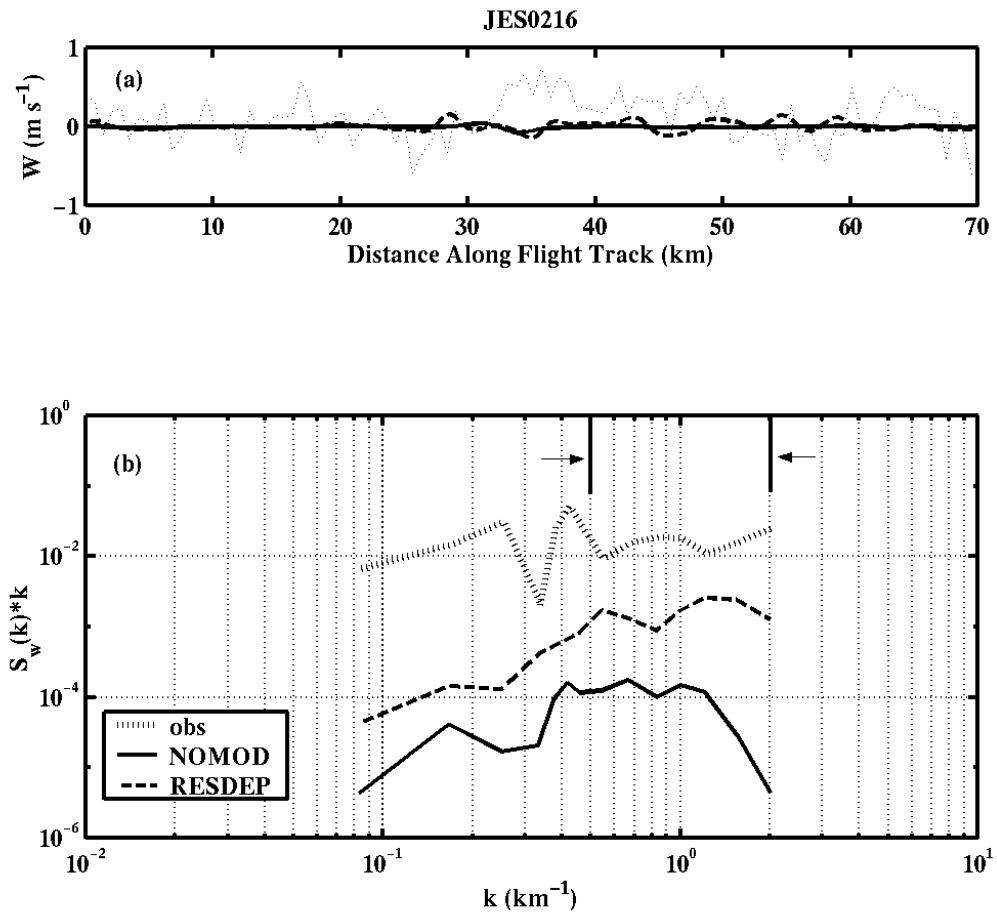
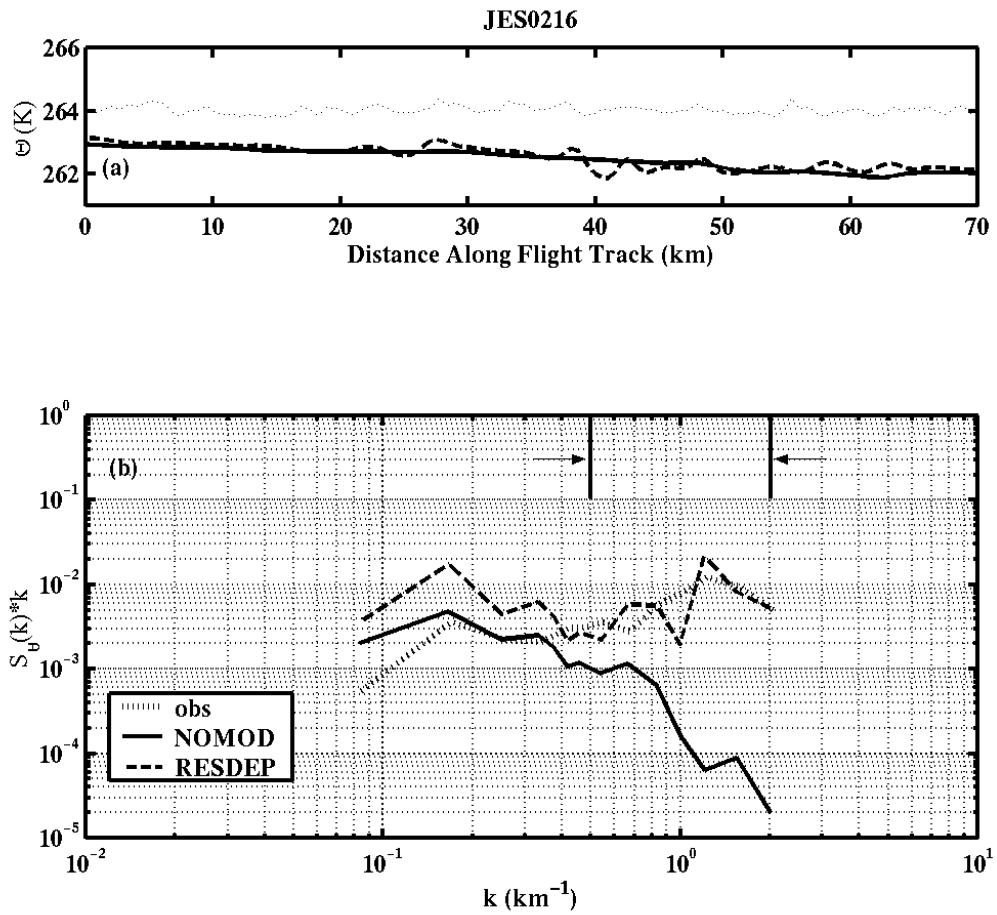


Figure 5.10. Same as in Figure 5.9, except for V wind component.



**Figure 5.11.** Same as in Figure 5.9, except for vertical velocity ( $W$ ).



**Figure 5.12.** Same as Figure 5.9, except for potential temperature ( $\theta$ ).

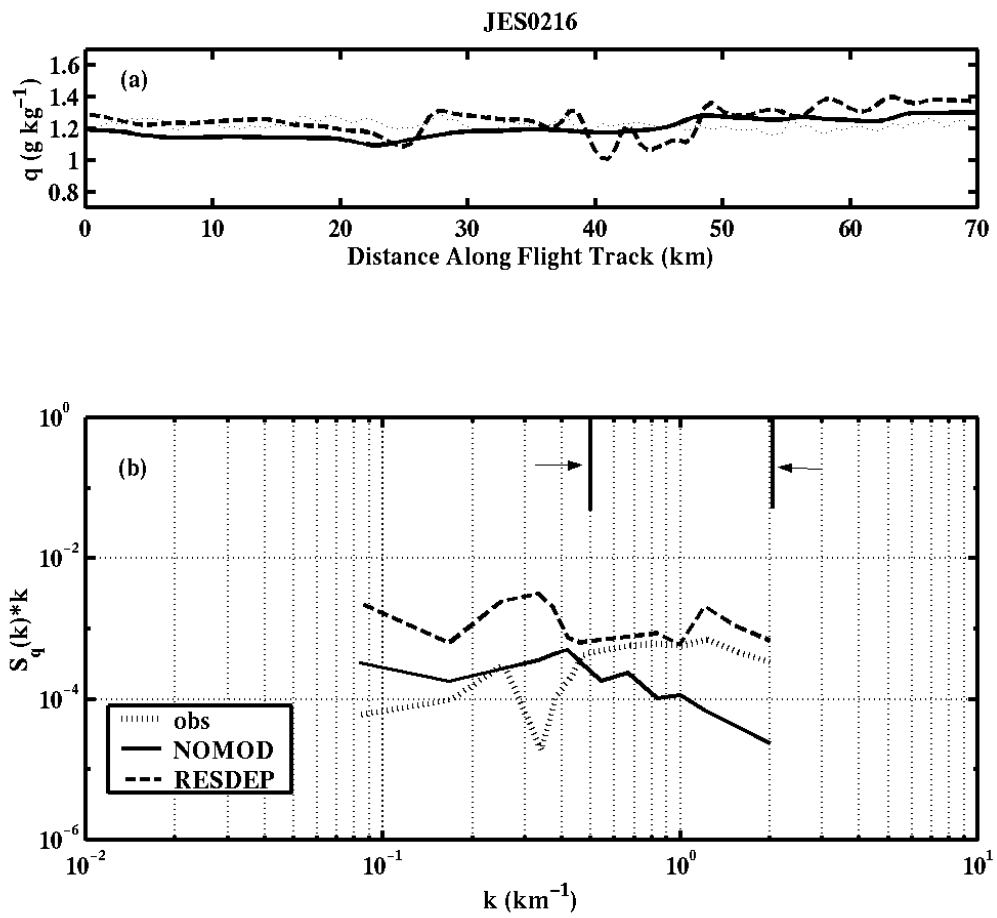
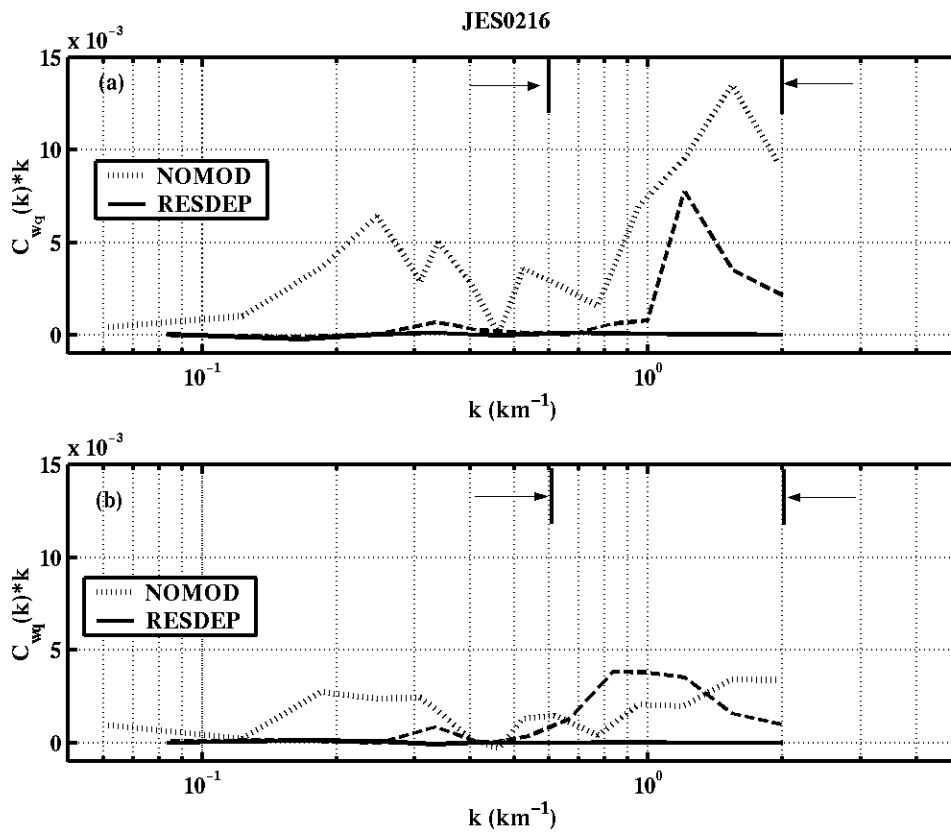


Figure 5.13. Same as in Figure 5.9, except for water vapor ( $q$ ).



**Figure 5.15.** Co-spectra between vertical velocity ( $w$ , in  $\text{ms}^{-1}$ ) and (a) potential temperature ( $\theta$ , in K); and (b) water vapor ( $q$  in  $\text{g kg}^{-1}$ ).

scale co-spectra, particularly at the small scales close to the resolvable limit of the model and near the scale of the convective roll vortices, appear to be more realistically simulated in RESDEP, based on the comparisons to the available observations.

### **3. SGS TKE and Fluxes**

The improved resolvability of the BL roll structure as the result of changes in RESDEP mixing length profile also result in changes in the SGS TKE and flux fields. The horizontal cross-sections for the simulated SGS sensible heat and latent heat fluxes in Figures 5.15 and 5.16 a and c, are shown at 5 m above sea level, where the total (SGS and resolved) heat fluxes are large (since the forcing is from the surface), and the SGS fluxes make up the majority of the total heat flux within the roll circulation (LeMone 1976). For NOMOD (Figures 5.15a and 5.6a), the sensible and latent heat fluxes are relatively invariant in the horizontal. The vertical cross-sections for the NOMOD heat fluxes (Figures 5.15b and 5.16b) have a fairly uniform vertical profile across the domain, and illustrate a BL in the CAA regime, undergoing both warming and moistening with time, since the heat and moisture fluxes are generally decreasing with height in the BL. As expected for a well-mixed BL, the fluxes are largest near the surface, due to the strong transfer of heat and moisture from the relatively warm ocean surface to the cooler, drier air above. We also see pockets of negative sensible heat fluxes and positive latent heat fluxes near the BL inversion, where warmer and drier air from the free atmosphere is being mixed downward into the cooler, moister BL air in the regions of downdraft eddies within the BL. The NOMOD SGS TKE distribution in the BL (Figure 5.17 a and b) shows no longitudinal alignment in the plane view of the middle of the BL, and has a more uniform profile along the vertical cross-section, showing no clear signal of enhancement with roll convection. Thus, we see no sign of the roll structure in the NOMOD SGS fields, reflective of their absence in the mean fields.

In contrast to NOMOD, the horizontal cross-sections for RESDEP SGS sensible and latent heat fluxes near the surface (Figures 5.15c and 5.16c) show significantly more spatial variation and slightly smaller magnitudes. This structure appears to be realistic for the fluxes, based on the description of LeMone (1976) of high-frequency (i.e., SGS) turbulence and fluxes of varying intensity superimposed on the mean roll circulation.

COAMPS JES0216 SGS Sensible Heat Flux

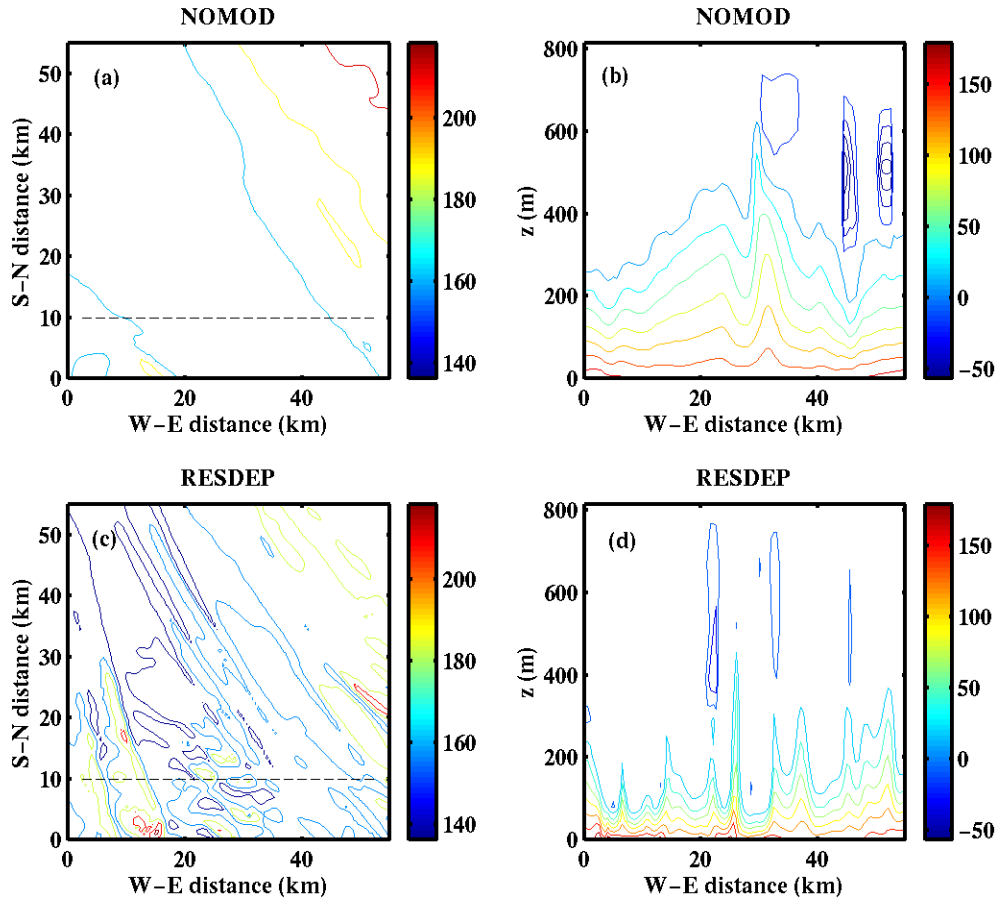


**Figure 5.15.** Same as in Figure 5.3, except for SGS Sensible Heat Flux ( $\text{W m}^{-2}$ ). Horizontal cross-section is at a height of 5 m. Contour interval is 25 for all plots.

COAMPS JES0216 SGS Latent Heat Flux

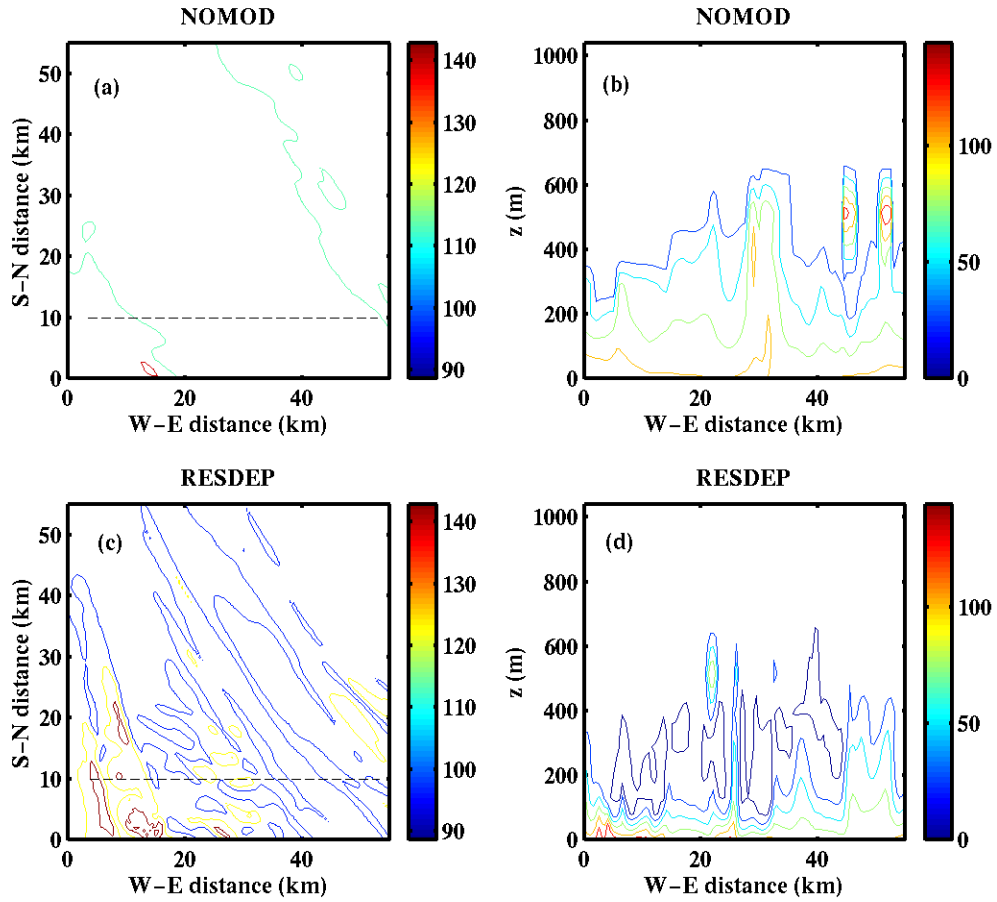
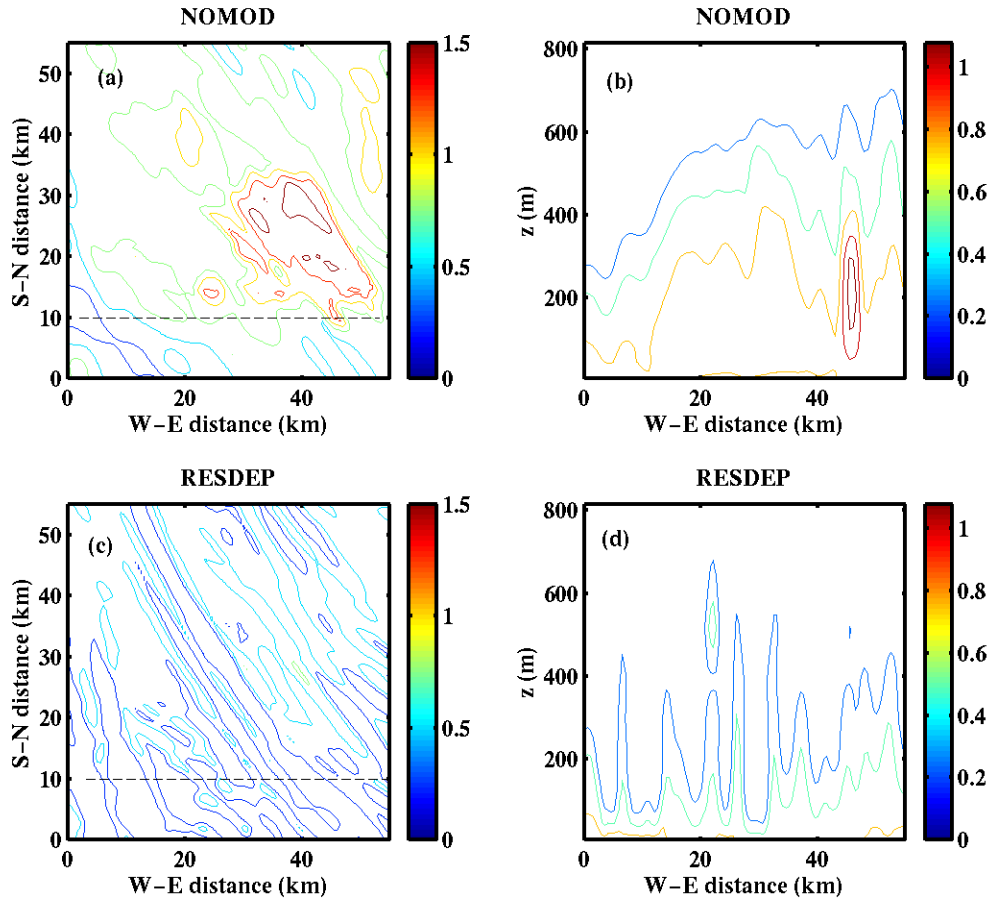


Figure 5.16. Same as in Figure 5.15, except for SGS Latent Heat Flux ( $\text{W m}^{-2}$ ).

The cross-sections of RESDEP TKE (Figure 5.17 c and d) present a TKE structure more indicative of a BL containing convective roll vortices. As was simulated in the mean fields, the BL TKE structure in the horizontal at 390 m above sea level shows longitudinal alignment in the direction of the mean BL wind. The locations of high TKE coincide with the locations of vertical velocity updraft cores (Figure 5.6d) at this height in the BL. The implication of the horizontal structure is seen in the vertical cross-section of the RESDEP SGS TKE (Figure 5.17d) showing TKE transport upwards in the updraft regions, while the TKE in the downdraft regions remains concentrated near the surface. This same structure is seen in the vertical cross-sections of the RESDEP SGS latent and sensible heat fluxes (Figures 5.15d and 5.16d).

The structure shown in the simulated flux and TKE cross-sections is supported by past observational and numerical studies. The observational study of LeMone (1976), states that the circulation of roll vortices in the convective BL influences the distribution of smaller scale turbulence (analogous to the SGS turbulence simulated here), with turbulent variances and fluxes systematically concentrated in regions of positive roll vertical velocity. LeMone (1976) refers to the systematic variation of turbulence across the rolls as modulated. The turbulence modulation was found to be the result of the redistribution of turbulence-producing elements by the mean roll circulation. Near the surface, the mean wind in the along-roll direction transports turbulent elements horizontally into regions of upward vertical motion, where the elements are then transported upward. If the turbulent elements are smaller scale eddies, the eddies will grow upward at an accelerated rate. LeMone (1976) also states that the modulation of the small-scale turbulence by the quasi-two dimensional rolls is maintained near the surface as well as at higher levels in the BL. Near the surface, the maintenance is due to horizontal variation in the shear production from the mean flow and buoyancy production. At higher BL levels, upward vertical transport of the TKE and fluxes within the roll updraft cores maintain the modulation. Chlond (1992) performed an idealized

COAMPS JES0216 SGS TKE



**Figure 5.17.** Same as in Figure 5.15, except for TKE ( $\text{m}^2 \text{s}^{-2}$ ). Horizontal cross-section is 390 m above sea level. Contour interval is 0.1 for all plots.

three-dimensional large-eddy simulation based on an observed case of cloud street development during a cold air outbreak over the Greenland Sea. Chlond's numerical results of the TKE field at 2 hours into the simulation are illustrated in Figure 5.18, and show a BL TKE structure similar to that described in LeMone (1976) and RESDEP. Similar TKE structure is also discussed in the two-dimensional simulation study of roll vortices developed in CAA conditions in Raasch (1990).

In validating the magnitudes of the COAMPS<sup>TM</sup> SGS parameterized fluxes and TKE near the surface with that derived from aircraft observations, it is important to note that the observed fluxes and TKE derived from the moving flux averaging represent the TOTAL turbulent energy from all scales, while the model parameterized quantities only represent the SGS portion of the energy. In order to compare the observations with the SGS model output, it is necessary to calculate only the observed turbulent energy from scales at and below the resolvable limit of  $2\Delta x$ , since this is the energy that should be represented by the model SGS parameterization scheme. The observed fluxes at and below the  $2\Delta x$  scale were calculated by first filtering out variances due to scales above 1 km, using a high-pass filter as was done in chapter III. The filtered observations were used to calculate a moving average variance and co-variance, where the length of the averaging leg was 10 km. These variances and co-variances were then used to calculate the TKE and fluxes. Figure 5.17 shows that the NOMOD SGS TKE and fluxes near the surface are slightly larger in magnitude than those from RESDEP. This is expected, since the smaller mixing length in RESDEP directly results in smaller eddy exchange coefficients used in the TKE and flux parameterizations (see equations 2.8 and 2.11-2.14). Except for the latent heat flux, which is simulated too large in magnitude in both simulations, the calculated TKE and fluxes from observations better compare to those from RESDEP. This close comparison is most clearly seen by inspection of the mean fluxes and TKE for the observations and RESDEP along the near-surface leg shown in Figure 5.19 a-d. However, the biggest differences are, again, in the spatial variability. The RESDEP fluxes and TKE have variability more closely resembling that of the observations, and the observed structure in LeMone (1976).

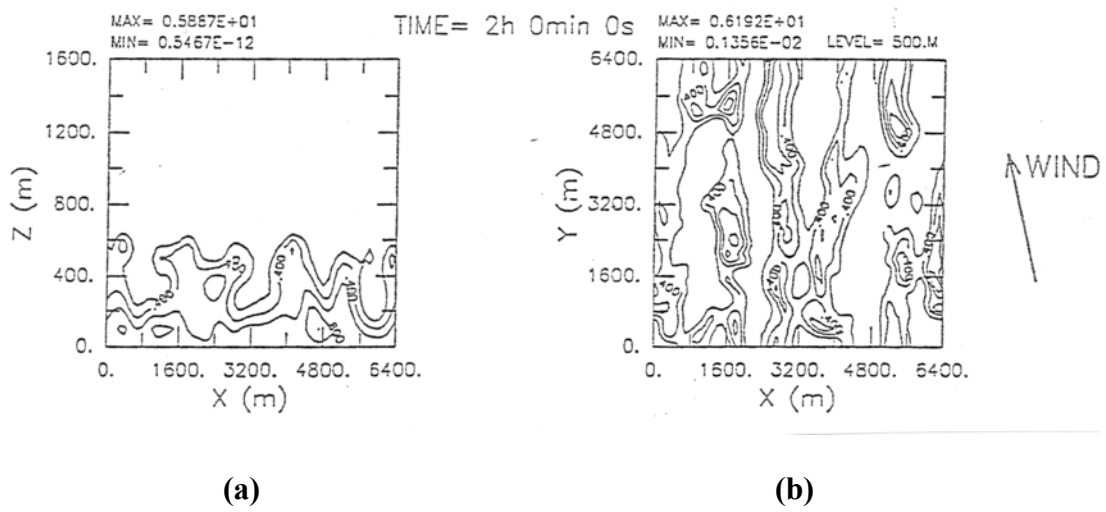


**Figure 5.18.** From Chlond (1992): vertical (a) and horizontal (b) cross-sections of simulated TKE from a roll convection case using a LES model.

## C. SUMMARY

Thorough comparisons of the NOMOD and RESDEP simulations have clearly shown that modification to the mixing length in the SGS turbulence parameterization within COAMPS<sup>TM</sup> yields a more realistic simulation of the BL roll structure observed in the JES0216 case study. The mixing length adjustment resulted in a reduction of the mixing of BL properties, and perpetuated the simulation of the roll vortices and associated BL structure, reflected in both the mean and SGS model fields. The RESDEP near-surface spectra for the wind, temperature, and moisture fields showed good agreement with observations in resolvable scale energy, especially near the scales of the rolls, at 4 to 6 km. Validation with aircraft near-surface horizontal leg and BL sounding observations of the mean quantities showed good agreement with both simulations, but RESDEP, unlike NOMOD, simulated the BL wind shear associated with the inflection point instability that contributes to the roll circulation. RESDEP SGS sensible and latent heat fluxes and TKE magnitudes and structure in the BL more realistically illustrate the transfer of near-surface heat and moisture in the along-roll direction near the surface and upwards in the regions of the updraft eddies, as described by LeMone (1976) and simulated by Chlond (1992) and Raasch (1990) for the roll convection case. The magnitudes of SGS turbulent fluxes and TKE for the RESDEP simulation were slightly lower than the NOMOD simulation and closer to the observed fluxes and TKE calculated for scales at 1 km and below, indicating a more correct simulation of the convective forcing and turbulence near the surface.

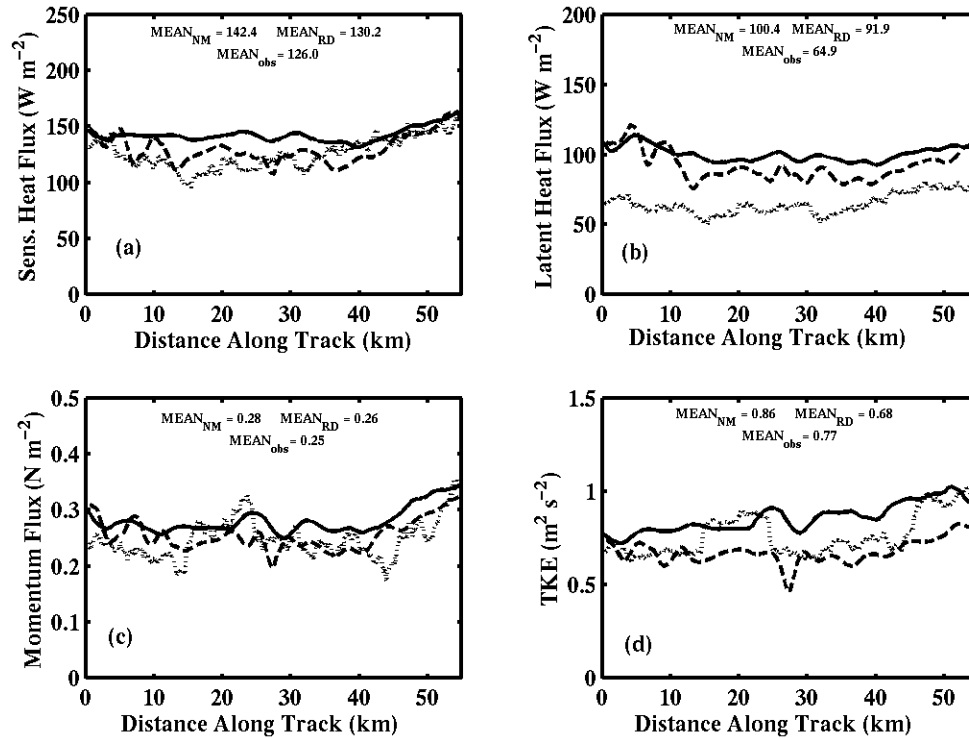


**Figure 5.19.** SGS Fluxes and TKE, and their means, derived from along-leg simulated data and aircraft observations from the near the surface (40 m above sea level) near the center of JES0216 domain 4. Shown in the figure is (a) sensible heat flux, (b) latent heat flux, (c) TKE, and (d) momentum flux (units shown) for NOMOD (NM) (solid), RESDEP (RD) (dashed) and aircraft observations (obs) (dotted).

## VI. SUMMARY, CONCLUSIONS, AND RECOMMENDATIONS

### A. SUMMARY AND CONCLUSIONS

This study focuses on evaluating the use of ensemble turbulence parameterization when the resolution of the model reaches that of the turbulent energy scale. The Navy COAMPS<sup>TM</sup> mesoscale model, at 500 m resolution, is used to simulate an over-ocean wintertime case (referred to as JES 0216 in this study) involving a VCSAO over the JES in which convective roll vortices were observed. The simulation was set up over the western JES region using a four-nest domain, where the inner nest, at 500 m resolution and 100x100 km<sup>2</sup> in size, covered regions of BL aircraft observations from the JES experiment. Our modeling study focused on the simulated output from the 500 m resolution nest at 12 hours into the simulation. Analysis of aircraft observations from this case revealed that the scale of the convective rolls was around 4 to 7 km. Testing of the true spatial resolvability of the COAMPS<sup>TM</sup> model revealed that the resolvable limit of the model was near the scale of  $6\Delta x$ , or 3 km for the 500 m resolution nest, and thus we expect the COAMPS<sup>TM</sup> high resolution nest to resolve these small mesoscale features.

The mixing length, which is a measure of turbulence mixing, is used within the parameterization for the calculation of the SGS eddy viscosity coefficients. In the COAMPS<sup>TM</sup> ensemble turbulence parameterization, the mixing length profile is based on the MY82 formulation, with the assumption that all turbulent motions are below the theoretical resolvable limit of the model ( $2\Delta x$ ). The resolution of domain 4 in the JES0216 simulation, at 500 m, falls within the scale of turbulence, since the model could theoretically resolve a 1 km turbulent eddy. Thus, the mixing length profile, using the ensemble assumptions, is not valid for the 500 m resolution model, since part of the turbulence is technically resolvable. Using a mixing length profile based on the size of the largest turbulent eddy would be inappropriate for the 500 m resolution nest, and result in overestimated turbulence mixing. It is likely that this overestimation of the mixing would result in a reduction of the resolvable scale spatial resolution of the simulated features.

The results of the control run simulation (NOMOD) revealed that this was indeed the case. NOMOD, using the MY82 mixing length formulation, adequately simulated the mean structure of an over-the-ocean boundary layer during a cold air outbreak, but failed to produce a clear signature of the observed convective rolls. Too much mixing by the model could prevent the simulation of the distinct alternating updraft/downdraft structure and resulting longitudinal alignment of the roll eddies by the mean BL wind. NOMOD simulated very little spatial variation in the mean fields, with no clear signature of roll-like convective eddy structure present in both horizontal and vertical cross-sections within the BL, the result of a very weak and unstructured simulated vertical velocity field. The small variability present at mid-BL levels shows no roll-like structure, as viewed in the horizontal plane. Visual inspection of BL cross-sections of the mean fields, supported by spectral analysis of the simulated fields in comparison with surface layer aircraft observations, revealed that the NOMOD simulation was not adequately simulating energies less than about 10 km, and not the expected 3 km resolvability or even the 4 to 7 km scale range of the observed rolls. The simulated SGS turbulent flux and energy structure was fairly uniform across the domain throughout the depth of the BL, signifying the over-mixing by the turbulence parameterization scheme.

Modifications are made to the ensemble turbulence parameterization in COAMPS<sup>TM</sup> through a modification to the turbulence mixing length scale. It is hoped that the new mixing length would yield the appropriate spatial resolution of the mean fields in the resolvable scale, and an appropriate representation of the turbulent structure in the SGS. The modification is based on observational analysis of the integral length scale (analogous to the mixing length) of over-the-ocean convective boundary layers, which illustrated that the integral scale profile in the BL expectedly decreases in magnitude as the maximum scale of turbulent eddies being considered decreases. From the integral scale analysis, we derived a resolution-dependent relationship that calculates the appropriate integral scale profile in the BL for the maximum scale of turbulent eddies considered. The equation for the integral length scale, as applied to the results from observations, is based on taking a weighted average between the integral length scale calculated for the smallest scales of turbulence considered (200 m) and the integral length

scale appropriate for the largest turbulent eddies (6 km), where the weighting is dependent on the scale being considered.

The resolution-dependent integral length scale formulation developed from the results of our observational study is adapted for use in a numerical model, and applied within COAMPS<sup>TM</sup> for the JES0216 case. This resolution-dependent mixing length formulation in COAMPS<sup>TM</sup> uses a weighted average between a mixing length appropriate for turbulent eddies within the inertial sub-range and the original COAMPS<sup>TM</sup> MY82 mixing length formulation, where again the weighting is based on the domain resolution. The resolution-dependent mixing length equation is then applied only to the 500 m resolution inner nest in the RESDEP simulation, where the appropriate mixing length profile is calculated by considering mixing by only the turbulent eddies at and below 1 km.

The RESDEP simulation resulted in much better simulation of the roll structure in all respects. RESDEP simulated turbulent roll eddies in both the momentum and scalar mean fields that are consistent with the aircraft observations and with past observational and numerical studies. The model simulated a much stronger and well-defined eddy structure in the vertical velocity field compared to NOMOD, with warm, moist updrafts and cooler, drier, downdrafts, aligned with the mean BL wind direction into longitudinal rolls, which scaled comparatively to the size of the observed rolls. RESDEP mean wind profiles illustrated significant wind shear within the BL, with an inflection-point in the wind components near the middle of the BL. This simulated shear signature, that was present in the observation profiles, but not present in the NOMOD wind profiles, indicates inflection-point instability as a contributor to production of the rolls. Energy spectra of the RESDEP surface layer mean fields showed improved spatial resolution in the convective roll scale range, comparing to the observations within one order of magnitude. SGS flux and TKE fields were also more realistic in comparison to NOMOD for the roll structure, where the flux and TKE modulation depicted the redistribution of turbulence-producing elements by the mean roll circulation. This structure was not validated with observations, due to the lack of spatial coverage, but was supported by the

observational study of LeMone (1976) and numerical studies by Chlond (1992) and Raasch (1990).

The convective roll case of JES0216 appropriately illustrated the issue that appropriate mixing is required to achieve the correct simulation of the convective roll structure in both the simulated mean fields and SGS fields. The implications for the use of a modified mixing length formulation within COAMPS<sup>TM</sup> is encouraging for the simulation of other mesoscale features whose development and maintenance via the interaction with eddies in the turbulent scale is important. However, further study to completely understand this issue and to improve the parameterization is obviously desired.

## **B. RECOMMENDATIONS FOR FURTHER STUDY**

The conclusion that the change in mixing length profile within COAMPS<sup>TM</sup> resulted in improvements to the simulated BL structure is thus far tested with the single case of JES 0216 for a resolution of 500 m. Further study is required to determine if the formulation for mixing length presented here is adequate for general use in COAMPS<sup>TM</sup>. First, the modified parameterization should also be tested for this case at even higher resolutions, to determine if the formulation is valid in the limit as  $\Delta x$  approaches the 100 m range. This test was not possible here, as the lack of computer resources prohibited a simulation of an adequately sized domain, with resolution below 500 m, for proper analysis of the issue. Model analysis becomes more difficult when the resolution of the model falls below 200 or 300 m, where large turbulent eddies are above the  $6\Delta x$  resolvable limit of the model. In this case, both SGS and resolved scale turbulence and fluxes must be considered in the model analysis, as in the case of LES studies. In addition to testing of different resolutions, sensitivity testing of the formulation using different values of minimum mixing length limits and different values of the constant parameter R is also suggested. Different ensemble turbulence parameterization schemes could also be tested, where a formulations for the mixing length and/or the eddy mixing coefficients other than the MY82 is used. In COAMPS<sup>TM</sup>, the MY82 scheme is most

commonly used for mixing length, but other built in options are available, such as the Therry and Lacarrere (1983) formulation.

In addition, we recommend testing of the validity of this mixing length modification for mesoscale features of varying type and scale, for cases over ocean and over land. In JES0216, the feature being simulated was very close to the  $6\Delta x$  resolvable limit of the model at 500 m resolution. Results may differ as the scale of the feature compared to the resolvable limit of the model increases. Cases where clouds form may also yield different results, since the parameterization scheme in COAMPS<sup>TM</sup> handles fluxes differently when clouds are present in the BL. For more complex mesoscale phenomena that are more intense, such as squall lines, convective cell thunderstorms, or sea-breeze convergence for instance, the real data simulation may not allow improvements to be easily seen. Testing of the formulation using idealized, vice real data simulations, may present clearer differences between control runs and modified runs for these more complex cases.

The JES 0216 case model-observation validation was limited by the lack of spatial coverage of the aircraft observations, where only BL soundings and surface layer flux legs were available. Cases where more complete aircraft data sets are available, containing long level flight legs at different levels within the BL and soundings to greater vertical levels would allow for a more complete inter-comparison of the simulated data and observations. High resolution satellite imagery, allowing for scale comparisons of simulated mesoscale cloud features, would also prove useful.

THIS PAGE INTENTIONALLY LEFT BLANK

## LIST OF REFERENCES

- Albrecht, B. A., D. A. Randall, and S. Nicholls, 1988: Observations of marine stratocumulus during FIRE. *Bull. Amer. Met. Soc.*, **69**, 618-626.
- Andreas, E. L. and K. A. Emanuel, 2001: Effects of sea spray on tropical cyclone intensity. *J. Atmos. Sci.*, **58**, 3741-3751.
- Arakawa, A., and J.-M. Chen, 1987: Closure assumptions in the cumulus parameterization problem. *Short and Medium Range Numerical Weather Prediction*. T. Matsuno, Ed., Meteor. Soc. Japan, Universal Academic Press, 107-131.
- Avissar, R., M. D. Moran, G. Wu, R. N. Meroney, and R. A. Peilke, 1990: Operating ranges of mesoscale numerical models and meteorological wind tunnels for the simulation of sea and land breezes. *Bound.-Layer Meteor.*, **50**, 227-275.
- Barker, D. M., A. Bourgeois, Y.-R. Guo, W. Huang, and Q. N. Xiao, 2003. A three-dimensional (3DVAR) data assimilation system for use with MM5. *NCAR Tech Note*, submitted.
- Bélair, S., P. Lacarrère, J. Noilhan, V. Masson, and J. Stein, 1998: High-resolution simulation of surface and turbulent fluxes during HAPEX-MOBILHY. *Mon. Wea. Rev.*, **126**, 2234-2253.
- \_\_\_\_\_, and J. Mailhot, 2001: Impact of horizontal resolution on the numerical simulation of a midlatitude squall line: Implicit versus explicit parameterization. *Mon. Wea. Rev.*, **129**, 2362-2375.
- Bernadet, L. R., L. D. Grasso, J. E. Nachamkin, C. A. Finley, and W. R. Cotton, 2000: Simulating convective events using a high-resolution mesoscale model. *J. Geophys. Res.*, **105**, 14963-14982.
- Blackadar, A. K., 1962: The vertical distribution of wind and turbulent exchange in neutral atmosphere. *J. Geophys. Res.*, **67**, 3095-3102.
- Bougeault, P., and J.-C. André, 1986: On the stability of the third-order turbulence closure for the modeling of the stratocumulus-topped boundary layer. *J. Atmos. Sci.*, **43**, 1574-1581.
- Braun, S. A., and W.-K. Tao, 2000: Sensitivity of high-resolution simulations of hurricane Bob (1991) to planetary boundary layer parameterizations. *Mon. Wea. Rev.*, **128**, 3941-3961.

- Bresch, J. F., R. J. Reed, and M. D. Albright, 1997: A polar low development over the Bering Sea: Analysis, numerical simulation, and sensitivity experiments. *Mon. Wea. Rev.*, **125**, 3109-3130.
- Bright, D. R., and S. L. Mullen, 2002: The sensitivity of numerical simulation of the southwest monsoon boundary layer to the choice of PBL turbulence parameterization in MM5. *Wea. Forecasting*, **17**, 99-114.
- Brown, R. A., 1980: Longitudinal instabilities and secondary flows in the planetary boundary layer: A review. *Rev. Geophys. Space. Phys.*, **18**, 683-697.
- Bruintjes, R. T., T. L. Clark, and W. D. Hall, 1995: The dispersion of tracer plumes in mountainous regions in central Arizona: Comparisons between observations and modeling results. *J. Appl. Meteor.*, **34**, 971-988.
- Brümmer, B., 1999: Roll and cell convection in wintertime arctic cold-air outbreaks. *J. Atmos. Sci.*, **29**, 2613-2636.
- \_\_\_\_\_, and M. Latif, 1985: Some studies on inflection point instability. *Beitr. Phys. Atmosph.*, **58**, 117-126.
- Bryan, G. H., J. C. Wyngaard, and J. M. Fritsch, 2003: Resolution requirements for the simulation of deep moist convection. *Mon. Wea. Rev.*, **131**, 2394-2416.
- Buckley, B. W., and L. M. Leslie, 2000: The Australian Boxing Day storm of 1998 – Synoptic description and numerical simulations. *Wea. Forecasting*, **15**, 543-558.
- Burk, S. D., and T. Haack, 2000: The dynamics of wave clouds upwind of coastal orography. *Mon. Wea. Rev.*, **128**, 1438-1455.
- Carruthers, D. J., and J. C. R. Hunt, 1986: Velocity fluctuations near and interface between a turbulent region and a stably stratified layer. *J. Fluid Mech.*, **165**, 475-501.
- Chien, F.-C., C. F. Mass, and P. J. Neiman, 2001: An observational and numerical study of an intense land-falling front along the northwest coast of the U.S. during COAST IOP2. *Mon. Wea. Rev.*, **129**, 934-955.
- Chlond, A., 1992: Three-dimensional simulation of cloud street development during a cold air outbreak. *Bound.-Layer Meteor.*, **58**, 161-200.
- Chou, S.-H., and J. Zimmerman, 1989: Bivariate conditional sampling of buoyancy flux during an intense cold-air outbreak. *Bound.-Layer Meteor.*, **46**, 93-112.

- Clark, T. L., T. Hauf, and J. P. Kuettner, 1986: Convectively forced internal gravity waves: Results from two-dimensional numerical experiments. *Quart. J. Roy. Meteor. Soc.*, **112**, 899-925.
- Colle, B.A., and C.F. Mass, 1996: An observational and modeling study of the interaction of low-level southwesterly flow with the Olympic mountains during COAST IOP 4. *Mon. Wea. Rev.*, **124**, 2152-2175.
- \_\_\_\_\_, and \_\_\_\_\_, 2000a: High-resolution observations and numerical simulations of easterly gap flow through the Strait of Juan de Fuca on 9-10 December, 1995. *Mon. Wea. Rev.*, **128**, 2398-2422.
- \_\_\_\_\_, and \_\_\_\_\_, 2000b: The 5-9 February 1996 flooding event over the Pacific Northwest: Sensitivity studies and evaluation of the MM5 precipitation forecasts. *Mon. Wea. Rev.*, **128**, 593-617.
- Cotton, W. R., and R. A. Anthes, 1989: *Storm and Cloud Dynamics*. Academic Press, 883 pp.
- Cox, S. K., D. S. McDougal, D. A. Randall, and R. A. Schiffer, 1987: FIRE—The first ISCCP regional experiment. *Bull. Amer. Met. Soc.*, **68**, 114–118.
- Deardorff, J. W., 1972: Numerical investigation of neutral and unstable planetary boundary layers. *J. Atmos. Sci.*, **29**, 91-115.
- \_\_\_\_\_, 1980: Stratocumulus-capped mixed layers derived from a three-dimensional model. *Bound.-Layer Meteor.*, **18**, 495-527.
- Delage, Y., 1974: A numerical study of the nocturnal atmospheric boundary layer. *Quart. J. Roy. Meteor. Soc.*, **100**, 351-364.
- Deng, A., N. L. Seaman, and J. S. Kain, 2003: A shallow-convection parameterization for mesoscale models. Part I: Submodel description and preliminary applications. *J. Atmos. Sci.*, **60**, 34-56.
- Dorman, C. E., R. C. Beardsley, N. A. Dashko, C. A. Friehe, D. Kheilf, K. Cho, R. Limeburner, and S. M. Varlamov, 2002: Winter marine conditions over the Japan Sea. *J. Geophys. Res.*, **98**, 23245-23263.
- Doyle, J. A., Naval Research Laboratory, Monterey, CA. Personal communication with the author, 30 September 2003.
- Droegemeier, K. K., G. Bassett, D. K. Lilly, and M. Xue, 1994: Very high resolution, uniform grid simulations of deep convection on a massively parallel processor:

Implications for small-scale predictability. Preprints, *Tenth Conf. On Numerical Weather Prediction*, Portland, OR, Amer. Meteor. Soc., 376-379.

Durran, D. R., 1999: Numerical methods for wave equations in geophysical fluid dynamics. *Springer, New York*, 465 pp.

Estournel, C. and D. Guedalia, 1987: A new parameterization of eddy diffusivities for nocturnal boundary layer modeling. *Bound.-Layer Meteor.*, **39**, 191-203.

Etling, D., and S. Raasch, 1987: Numerical simulation of vortex roll development during a cold air outbreak. *Dyn. Atmos. Oceans*, **10**, 277-290.

\_\_\_\_\_, and R. A. Brown, 1993: Roll vortices in the planetary boundary layer: A review. *Bound.-Layer Meteor.*, **75**, 215-248.

Fairall, C. W., E. F. Bradley, D. P. Rogers, J. B. Edson, and G. S. Young, 1996: Bulk parameterization of air-sea fluxes for Tropical Ocean Global Atmosphere Coupled Ocean-Atmosphere Response Experiment. *J. Geophys. Res.*, **101**, C2, 3747-3764.

Frank, W. M., 1983: The cumulus parameterization problem. *Mon. Wea. Rev.*, **111**, 1859-1871.

\_\_\_\_\_, and C. Cohen, 1987: Simulation of tropical convective systems. Part I: A cumulus parameterization. *J. Atmos. Sci.*, **44**, 3787-3799.

Fritsch, J. M., and C. F. Chappell, 1980: Numerical prediction of convectively driven mesoscale pressure systems. Part I: Convective parameterization. *J. Atmos. Sci.*, **37**, 1722-1733.

Gal-Chen, T., and C. J. Sommerville, 1975: On the use of a coordinate transformation for the solution of the Navier-Stokes equations. *J. Comput. Phys.*, **17**, 208-228.

Gaudet, B., and W. R. Cotton, 1998: Statistical characteristics of a real-time precipitation forecasting model. *Wea. Forecasting*, **13**, 966-982.

Gayno, G. A., 1994: Development of a higher-order, fog producing boundary layer model suitable for use in numerical weather prediction. M.S. thesis, Dept. of Meteorology, The Pennsylvania State University, 104 pp. [Available from the Dept. of Meteorology, The Pennsylvania State University, University Park, PA 16802].

Gossard, E. E., R. B. Chadwick, W. D. Neff, and K. P. Moran, 1982: The use of ground-based radars to measure gradients, fluxes and structure parameters in elevated layers. *J. Appl. Meteor.*, **21**, 211-226.

- Grossman, R. L., 1982: An analysis of vertical velocity spectra obtained in the BOMEX fair-weather, trade-wind boundary layer. *Bound.-Layer Meteor.*, **23**, 323-357.
- Harris, D. E., Foufoula-Georgiou, K. K. Droegemeier, and J. J. Levit, 2001: Multi-scale statistical properties of a high-resolution precipitation forecast. *J. Hydrometeor.*, **2**, 406-418.
- Hodur, R. M., 1997: The Naval Research Laboratory's Coupled Ocean/Atmosphere Mesoscale Prediction System (COAMPS). *Mon. Wea. Rev.*, **125**, 1414-1430.
- \_\_\_\_\_, and J. D. Doyle, 1998: The coupled ocean/atmosphere mesoscale model prediction system (COAMPS). *Coastal Ocean Prediction*, Coastal and Marine Estuarine Studies, **56**, 125-155.
- Holstag, A. A. M., and B. A. Boville, 1993: Local versus non-local boundary layer diffusion in a global climate model. *J. Climate*, **6**, 1825-1842.
- Hong, S.-H., and H.-L. Pan, 1996: Non-local boundary layer vertical diffusion in a medium-range forecast model. *Mon. Wea. Rev.*, **124**, 2322-2339.
- Janjic, Z. I., J. P. Gerrity Jr., and S. Nickovic, 2001: An alternative approach to nonhydrostatic modeling. *Mon. Wea. Rev.*, **129**, 1164-1178.
- Kaimal, J. C., 1973: Turbulence spectra, length scales, and structure parameters in the stable surface layer. *Bound.-Layer Meteor.*, **4**, 289-309.
- \_\_\_\_\_, J. C. Wyngaard, D. A. Haugen, O. R. Coté, Y. Izumi, S. J. Caughey, and C. J. Readings, 1976: Turbulence structure in the convective boundary layer. *J. Atmos. Sci.*, **33**, 2152-2169.
- \_\_\_\_\_, J. C. Wyngaard, Y. Izumi and O. R. Coté, 1972: Spectral characteristics of surface layer turbulence. *Quart. J. Roy. Meteor. Soc.*, **98**, 563-589.
- Kain, J. S., and J. M. Fritsch, 1990: A one-dimensional entraining/detraining plume model and its application in convective parameterization. *J. Atmos. Sci.*, **47**, 2784-2802.
- Kalnay, E., S. J. Lord, and R. D. McPherson, 1998. Maturity of operational numerical weather prediction: medium range. *Bull. Amer. Met. Soc.*, **179**, 2753-2769.
- Khelif, D., C. A. Friehe, H. Jonsson, Q. Wang, and K. Rados, 2003: Wintertime boundary layer structure and air-sea interaction over the Japan/East Sea. Accepted by *Deep Sea Research*.

- Klemp, J. B., and R. B. Wilhelmson, 1978: The simulation of three-dimensional convective storm dynamics. *J. Atmos. Sci.*, **35**, 1070-1096.
- Kloesel, K. A., B. A. Albrecht, and D. P. Wylie, 1988: FIRE marine stratocumulus observations – summary of operations and synoptic conditions. FIRE Tech. Rep. No. 1., The Pennsylvania State University, Dept. of Meteorology, University Park, PA.
- Kolmogorov, A. N., 1941: Energy dissipation in locally isotropic turbulence. *Doklady AN SSSR*, **32**, No. 1, 19-21.
- Kuo, Y.-H., W. Wang, Q. Zhang, W.-C. Lee, and M. Bell, 2001: High-resolution simulation of Hurricane Danny (1997): Comparison with radar observations. Preprints, *11<sup>th</sup> PSU/NCAR Mesoscale Modeling System Workshop*, Boulder, CO, PSU/NCAR, 94-97. [Available from MMM Division, NCAR, P.O. Box 3000, Boulder, CO 80303.]
- Lacser, A., and S. P. S. Arya, 1986: A comparative assessment of mixing length parameterizations in the stably stratified nocturnal boundary layer (NBL). *Bound.-Layer Meteor.*, **38**, 1-22.
- LeMone, M. A., 1976: Modulation of turbulent energy by longitudinal rolls in an unstable boundary layer. *J. Atmos. Sci.*, **33**, 1308-1320.
- \_\_\_\_\_, and W. T. Pennell, 1976: The relationship of trade wind cumulus distribution to subcloud layer fluxes and structure. *Mon. Wea. Rev.*, **104**, 524-539.
- Lenschow, D. H., and B. B. Stankov, 1986: Length scales in the convective boundary layer. *J. Atmos. Sci.*, **43**, 1198-1209.
- Lilly, D. K., 1967: The representation of small-scale turbulence in numerical simulation experiments. *Proceedings of the Tenth IBM scientific computing symposium on environmental sciences*, Yorktown Heights, NY, IBM DP Division, 195-210.
- Lorenc, A. C., S. P. Ballard, R. S. Bell, N. B. Ingleby, P. L. F. Andrews, D. M. Barker, J. R. Bray, A. M. Clayton, T. Dalby, D. Li, T. J. Payne, and F. W. Saunders, 2000: The Met. Office global three-dimensional variational data assimilation scheme. *Quart. J. Roy. Meteor. Soc.*, **126**, 2991-3012.
- Louis, J.F., 1979: A parametric model of vertical eddy fluxes in the atmosphere. *Bound.-Layer Meteor.*, **17**, 187-202.
- Lynn, B. H., D. R. Stauffer, P. J. Wetzel, W.-K. Tao, P. Alpert, N. Perlin, R. D. Baker, R. Muñoz, A. Boone, and Y. Jia, 2001: Improved simulation of Florida summertime convection using the PLACE land model and 1.5-order turbulence parameterization

- coupled to the Penn-State-NCAR mesoscale model. *Mon. Wea. Rev.*, **129**, 1441–1461.
- Mason, P. J., 1983: On the influence of variation in Monin-Obukov length on horizontal roll vortices in an inversion-capped boundary layer. *Bound.-Layer Meteor.*, **27**, 43–68.
- \_\_\_\_\_, 1985: A numerical study of cloud streets in the planetary boundary layer. *Bound.-Layer Meteor.*, **32**, 281–304.
- \_\_\_\_\_, 1994: Large-eddy simulation: A critical review. *Quart. J. Roy. Meteor. Soc.*, **120**, 1–26.
- \_\_\_\_\_, and R. I. Sykes, 1980: A two-dimensional numerical study of horizontal roll vortices in the neutral atmospheric boundary layer. *Quart. J. Roy. Meteor. Soc.*, **106**, 351–366.
- \_\_\_\_\_, and \_\_\_\_\_, 1982: A two-dimensional numerical study of horizontal roll vortices in an inversion-capped boundary layer. *Quart. J. Roy. Meteor. Soc.*, **108**, 801–823.
- Mass, C., and Y.-H. Kuo, 1998: Regional real-time numerical weather prediction: Current status and future potential. *Bull. Amer. Met. Soc.*, **79**, 253–263.
- Mass, C., D. Ovens, K. Westrick, and B.A. Colle, 2002: Does increasing the horizontal resolution produce more skillful forecasts? *Bull. Amer. Met. Soc.*, **83**, 407–430.
- Mellor, G. L., 1973: Analytic prediction of the properties of stratified planetary surface layers. *J. Atmos. Sci.*, **30**, 1061–1069.
- \_\_\_\_\_, and T. Yamada, 1982: Development of a turbulence closure model for geophysical fluid problems. *Rev. of Geophys. and Space Phys.*, **20**, 851–875.
- Molinari, J., and M. Dudek, 1992: Parameterization of convective precipitation in mesoscale numerical models: a critical review. *Mon. Wea. Rev.*, **120**, 326–344.
- Nucciarone, J. F., and G. S. Young, 1991: Aircraft measurements of turbulence spectra in the marine stratocumulus-topped boundary layer. *J. Atmos. Sci.*, **48**, 2382–2392.
- Obukov, A. M., 1941: Energy distribution in the spectrum of turbulent flow. *Izvestiya AN SSSR, Ser. Geogr. Geofiz.*, No. 4-5, 453–466.
- Parrish, D. F., and J. C. Derber, 1992: The National Meteorological Center's Spectral Statistical Interpolation analysis system. *Mon. Wea. Rev.*, **120**, 1747–1763.

- Pielke, R. A., 2002: *Mesoscale Meteorological Modeling*. 2d Ed., International Geophysics Series, v. 78, Academic Press. 676 pp.
- Rabier, F., H. Jarvinnen, E. Klinker, J.-F. Mahfouf, and A. Simmons, 2000: The ECMWF operational implementation of four-dimensional variational assimilation. I: Experimental results with simplified physics. *Quart. J. Roy. Meteor. Soc.*, **126**, 1143-1170.
- Rogers, D. P., D. W. Johnson, and C. A. Friehe, 1995: The stable boundary layer over a coastal sea, part I: airborne measurements of the mean and turbulence structure. *J. Atmos. Sci.*, **52**, 673-682.
- Rogers, E., M. Ek, Y. Lin, K. Mitchell, D. Parrish, and G. DiMego, 2001: "Changes to NCEP Meso Eta Analysis and Forecast System: Assimilation of observed precipitation, upgrades to land-surface physics, modified 3DVAR analysis." [<http://www.emc.ncep.noaa.gov/mmb/mmbpll/spring2001/tpb/>].
- Rosenthal, S. L., 1978: Numerical simulation of tropical cyclone development with latent heat release by the resolvable scales. I: Model description and preliminary results. *J. Atmos. Sci.*, **35**, 258-271.
- Skamarock, W. C., M. L. Weisman, and J. B. Klemp, 1994: Three-dimensional evolution of simulated long-lived squall lines. *J. Atmos. Sci.*, **51**, 2563-2584.
- Shafran, P. C., N. L. Seaman, and G. A. Gayno, 2000. Evaluation of numerical predictions of boundary layer structure during the Lake Michigan Ozone Study. *J. Appl. Meteor.*, **39**, 412-426.
- Smagorinsky, J., 1963: General circulation experiments with the primitive equations: 1. The basic experiment. *Mon. Wea. Rev.*, **91**, 99-164.
- Smedman, A. S., and U. Höögström, 1975: Spectral gap in surface-layer measurements. *J. Atmos. Sci.*, **32**, 340-350.
- Stull, R. B., 1988: *An Introduction to Boundary Layer Meteorology*. Kluwer Academic Publishers, 666 pp.
- Taylor, G. I., 1938: The spectrum of turbulence. *Proc. Roy. Soc.*, **A164**, 476-490.
- TCIPO, 1993: Tropical Ocean-Global Atmosphere Coupled Ocean-Atmosphere Response Experiment Intensive Observing Period Operations Summary, 505 pp. [Available from TOGA COARE International Project Office, University Corporation for Atmospheric Research, P.O. Box 3000, Boulder, CO 80307.]

- Therry, G. and P. LaCarrère, 1983: Improving the kinetic energy model for planetary boundary layer description. *Bound.-Layer Meteor.*, **25**, 63-88.
- Wang, Q., and B. A. Albrecht, 1994: Observations of cloud-top entrainment in marine stratocumulus clouds. *J. Atmos. Sci.*, **51**, 1530-1547.
- Weisman, M.L., J. B. Klemp, and R. Rotunno, 1988: Structure and evolution of numerically simulated squall lines. *J. Atmos. Sci.*, **45**, 1990-2013.
- Weller, R. A., and S. P. Anderson, 1996: Surface meteorology and air-sea fluxes in the Western Equatorial Pacific warm pool during the TOGA Coupled Ocean-Atmosphere Response Experiment. *J. Climate*, **9**, 1959-1990.
- Wen, L., W. Yu, C. A. Lin, M. Beland, R. Benoit, and Y. Delage, 2000: The role of land surface schemes in short-range, high spatial resolution forecasts. *Mon. Wea. Rev.*, **128**, 3605-3616.
- Westrick, K., and C. F. Mass, 2001: An evaluation of a high-resolution hydrometeorological modeling system for prediction of a cool-season flood event in a coastal mountainous watershed. *J. Hydrometeor.*, **2**, 161-180.
- Wyngaard, J. C., 1982: Boundary layer modeling. In *Atmospheric Turbulence and Air Pollution Modeling*, F. T. M. Nieuwstadt and H. Van Dop, Eds., 69-106. D. Reidel, Dordrecht, The Netherlands.
- \_\_\_\_\_, 1983: Lectures on the planetary boundary layer. In *Mesoscale Meteorology – Theories, Observations, and Models*, T. Gal-Chen and D. K. Lilly, D. Reidel, Eds. Dordrecht, The Netherlands.
- Yamasaki, M., 1977: A preliminary experiment of the tropical cyclone without parameterizing the effects of cumulus convection. *J. Meteor. Soc. Japan*, Series II, **55**, 11-31.
- Young, G. S., 1987: Mixed layer spectra from aircraft measurements. *J. Atmos. Sci.*, **44**, 1251-1256.
- \_\_\_\_\_, D. A. R. Kristovich, M. R. Hjelmfelt, R. C. Foster, 2002: Rolls, streets, waves, and more: A review of quasi-two-dimensional structures in the atmospheric boundary layer. *Bull. Amer. Meteor. Soc.*, **83**, 997-1001.
- Yu, T. W., 1976: Numerical studies of the atmospheric boundary layer with a turbulent energy closure scheme. *Third Symposium on Atmospheric Turbulence*, Amer. Meteor. Soc. (preprint).

THIS PAGE INTENTIONALLY LEFT BLANK

## INITIAL DISTRIBUTION LIST

1. Defense Technical Information Center  
Ft. Belvoir, Virginia
2. Dudley Knox Library  
Naval Postgraduate School  
Monterey, California
3. Dr. Qing Wang  
Department of Meteorology  
Naval Postgraduate School  
Monterey, California
4. Dr. Carlyle H. Wash  
Department of Meteorology  
Naval Postgraduate School  
Monterey, California
5. Dr. Robert L. Haney  
Department of Meteorology  
Naval Postgraduate School  
Monterey, California
6. Dr. Roger T. Williams  
Department of Meteorology  
Naval Postgraduate School  
Monterey, California
7. Dr. Peter C. Chu  
Department of Oceanography  
Naval Postgraduate School  
Monterey, California
8. Dr. Shouping Wang  
Naval Research Laboratory  
Monterey, California
9. Dr. Douglas Miller  
Naval Postgraduate School  
Monterey, California

10. LCDR Michelle K. Whisenant  
OA Division  
USS Tarawa  
San Diego, California